Amorphous Lead Oxide (a-PbO) for direct conversion X-ray imaging detectors

by

Oleksandr Grynko

A dissertation submitted in partial fulfillment

of the requirements of the degree of

Doctor of Philosophy

in

Chemistry and Materials Science

Lakehead University

Thunder Bay, Ontario, Canada, 2022

Amorphous Lead Oxide (a-PbO) for direct conversion X-ray imaging detectors

OLEKSANDR GRYNKO

Doctor of Philosophy, 2022

Chemistry and Materials Science Program

Lakehead University

Abstract

Modern medical imaging revolutionized the way that medical conditions are diagnosed. It became possible after significant advancements in science and technology related to the medical visualization field. X-ray imaging is one of the most commonly used modalities; it now relies on the digital Flat Panel X-ray Imagers (FPXIs) that can provide high-quality radiographs while benefiting from many advantages inherent to the digital detectors technology, including reduced radiation exposure and convenience of use. Although some FPXIs have already been commercialized, their application is very limited, and they do not exploit the full potential of this technology. Therefore, there is a niche that can only be filled through extensive research and development. The work carried out and presented in the dissertation contributes to this effort.

In this work, an Amorphous Lead Oxide (a-PbO) photoconductor is investigated as a material of choice in the direct conversion digital FPXIs for various medical and industrial X-ray imaging applications, including general radiography, real-time fluoroscopy, digital breast tomosynthesis, and non-destructive testing. a-PbO is a recently developed material with high X-ray stopping power in a wide X-ray energy range and high theoretical X-ray–to–charge conversion efficiency. Most importantly, it lacks certain disadvantages of its predecessor, Polycrystalline Lead Oxide (poly-PbO), such as slow temporal response, high porosity, and environmental instability, which

limited the success of poly-PbO–based FPXIs in the past. Although very promising, the technology of a-PbO photoconductor is not mature enough for practical applications and the properties of this material have not been fully studied.

One important aspect in the development of the FPXI based on the a-PbO photoconductor addressed in this work is the reduction of the dark current to an acceptably low level at the strong practical electric fields without sacrificing the major benefits of a-PbO, i.e., fast temporal response and high X-ray sensitivity. It was accomplished by investigating and destroying the root cause of this problem, which is the charge injection from the electrode into the photoconductor. Two detector designs utilizing multilayer structures based on Lead Oxide photoconductor were proposed in this work, each with its advantages and shortcomings. The first configuration comprises a thin injection preventing layer of a-PbO overlayed with a relatively thick layer of poly-PbO X-ray–to–charge transducer. a-PbO/poly-PbO detector demonstrated improved structural homogeneity and lesser dispersion of charge transport in comparison to that of poly-PbO, and fast temporal response inherent to a-PbO. In the second design, a blocking layer structure with a Polyimide (PI) polymer and an a-PbO photoconductor was developed and evaluated. PI/a-PbO detector demonstrated suppression of the dark current down to an acceptably low level and a capability to withstand a strong electric field, while further improving the temporal response and X-ray sensitivity in comparison to that of other competitive detectors. This technological achievement made it possible to examine fundamental properties of the a-PbO photoconductor related to charge generation and recombination. Through the experimental investigation of the X-ray sensitivity, it was determined that the columnar recombination and bulk Langevin recombination mechanisms interplay in the a-PbO photoconductor at practical electric fields.

Acknowledgements

I would like to express my sincere gratitude to my supervisor, Dr. Alla Reznik, for her never-ending support. She always encouraged my work, inspired me to new ideas and guided me academically, professionally and personally in the right direction throughout my PhD endeavour, for which I am greatly indebted.

I am thankful to my supervisory committee members, Dr. Mitchell Albert and Dr. Dimiter Alexandrov, for their support and encouragement. The knowledge they have shared with me made my studies and my research more comprehensive and multidisciplinary. I am also thankful to my external examiner, Prof. Fedir Sizov, for providing valuable and thorough feedback on my work. I would also like to thank the Physics Department and Chemistry and Materials Science program at Lakehead University and the Thunder Bay Regional Health Research Institute for being my academic home through these years.

I am extremely grateful to all current and former members of Dr. Reznik's Advanced Detection Devices group, that I was a proud member of, especially to Dr. Oleksii Semeniuk, Sergey Reznik and Giovanni DeCrescenzo, for fruitful discussions, countless technical support and continuous expansion of my knowledge and skills.

I would like to thank all of the academic and industrial collaborators for their expert help and advice, without which many aspects of this work would not be possible. I want to express my special gratitude to Dr. Gytis Juska for stimulating discussions and the LEADER team at Teledyne DALSA for constructive deliberations on the prospects for the practical applications of this work.

I want to acknowledge NSERC, Mitacs, Teledyne DALSA, Lakehead University, and Ontario Graduate Scholarship program for their financial support.

Finally, I want to thank all of my friends and family, and especially my wife, for their love, support and patience, for cheering me up and for being there for me on this long and bumpy journey.

Table of contents

List of figures

Chapter 1

Chapter 2

Chapter 3

Chapter 4

Chapter 5

List of tables

Chapter 2

Chapter 4

Chapter 5

List of acronyms

ALARA	As Low As Reasonably Achievable
AMFPI	Active Matrix Flat Panel Imager
APC	Article Processing Charges
APS	Active-Pixel Sensor
BE	Binding Energy
CA	Cellulose Acetate
CASINO	monte CArlo SImulation of electroNs in sOlids
CELIV	Charge Extraction by Linearly Increasing Voltage
CMOS	Complementary Metal-Oxide-Semiconductor
CPI	Communications & Power Industries
CVD	Chemical Vapour Deposition
CZT	Cadmium Zinc Telluride
DBT	Digital Breast Tomosynthesis
DC	Dark Current
dc	Direct Current
DQE	Detective Quantum Efficiency
DSA	Digital Subtraction Angiography
EHP	Electron-Hole Pair
FFDM	Full-Field Digital Mammography
FOV	Field Of View

FPXI	Flat-Panel X-ray Imager
GPIB	General Purpose Interface Bus
HARP	High-gain Avalanche Rushing amorphous Photoconductor
HVL	Half-Value Layer
ICTF	International Conference on Thin Films
IEEE	Institute of Electrical and Electronics Engineers
ITO	Indium Tin Oxide
JVC	Joint Vacuum Conference
KE	Kinetic Energy
LAD	Laser Assisted Deposition
LED	Light-Emitting Diode
MIC	Medical Imaging Conference
MIS	Metal-Insulator-Semiconductor
MRI	Magnetic Resonance Imaging
MTF	Modulation Transfer Function
NIST	National Institute of Standards and Technology
NMP	n-methyl-2-pyrrolidone
NPS	Noise Power Spectrum
NSERC	Natural Sciences and Engineering Research Council of Canada
NSS	Nuclear Science Symposium
PC	Photocurrent
PET	Positron Emission Tomography

PHS	Pulse-Height Spectroscopy
PI	Polyimide
PVD	Physical Vapour Deposition
PVK	Polyvinylcarbazole
RC	Resistance-Capacitance
R&D	Research and Development
SDD	Source-to-Detector Distance
SEIA	Sensors and Electronic Instrumentation Advances
SEM	Scanning Electron Microscopy
SNR	Signal-to-Noise Ratio
SPIE	Society of Photo-optical Instrumentation Engineers
SREM	Stopping and Range of Electrons in Matter
SZD	Structure Zone Diagram
TBC	Tucker-Barnes-Chakraborty
TFT	Thin-Film Transistor
TOF	Time-Of-Flight
TV	Television
US	Ultrasound
XPM	X-ray–induced Photocurrent Method
XPS	X-ray Photoelectron Spectroscopy
XRD	X-ray Diffraction
XRII	X-ray Image Intensifier

Chapter 1

Introduction

1 X-ray medical imaging modality

Modern medicine relies on reliable, affordable, and safe diagnosis in order to provide the most accurate treatment. In clinical cases when direct visual observation of the patient is not sufficient, advanced imaging techniques can be used to visualize the interior of the body. Radiography, or X-ray imaging (including static radiography, real-time fluoroscopy used to visualize the continuous movement of internal structures, and tomosynthesis that produces three-dimensional images), is the most widely used medical imaging procedure today. The number of X-ray-based diagnostic and interventional procedures is greater than the combined use of ultrasound (US), magnetic resonance imaging (MRI), computed tomography (CT), and nuclear medicine.

Radiography is performed with an X-ray source on one side of the patient and an X-ray detector on the other side; it is a form of a transmission and projection imaging modality. The X-ray tube emits a uniform collimated X-ray beam towards the patient; X-ray photons interact with tissues while passing through the body and reach the detector, where an X-ray image is formed. The uniform distribution of X-rays reaching the patient is modified by the degree of interaction of the X-rays with the tissues (via various absorption and scattering mechanisms discussed in the next section). Different tissues, such as soft tissue, bone, and air have very different properties affecting attenuation (i.e., composition and density), providing a non-uniform but informative distribution of X-ray intensity that comes out of the patient. The radiographic image is essentially a map of this distribution. This process is schematically shown in Figure 1.

X-ray radiography is considered anatomical imaging since it provides information about anatomical structures through a projection of distribution of the density and composition of the tissues within the detector's field of view (FOV). In contrast, nuclear medicine, for example, visualizes the distribution of an injected radiotracer, which represents relative metabolic properties of tissues affected by disease conditions, and therefore, nuclear medicine is considered a functional imaging modality [1–3].

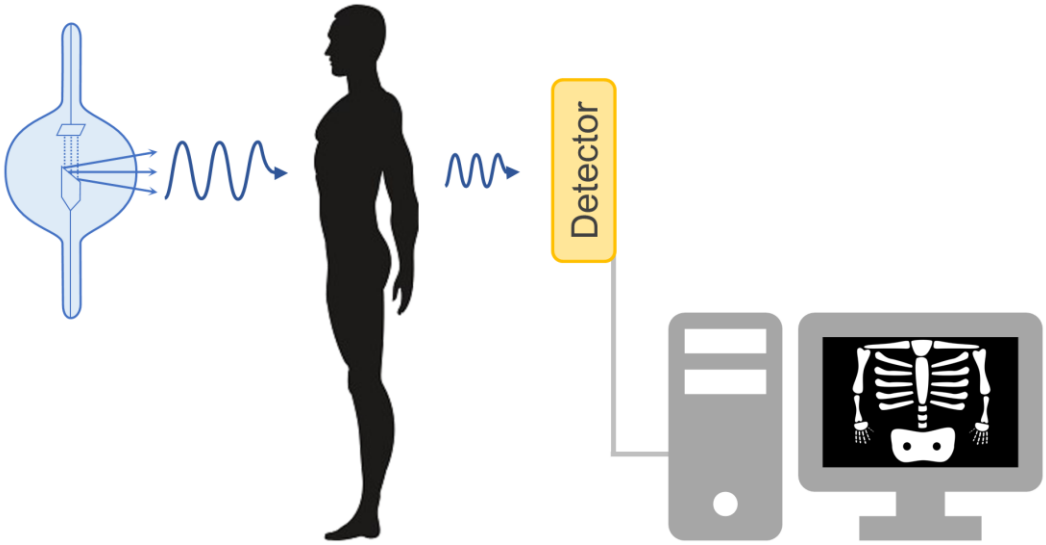

Figure 1. Schematic representation of the radiographic procedure.

The transmitted X-ray beam (or, rather, distribution of its intensity within the FOV) is a carrier of information in radiography, and more X-rays generally provide better image quality, which allows very subtle pathologies to be detected. However, X-rays are a form of ionizing radiation, which can be harmful to the patient and cause damage to the living tissues. Therefore, the radiologist should adhere to the As Low As Reasonably Achievable (ALARA) approach in clinical practice in order to minimize the radiation exposure (both to patient and radiologist) while still providing suitable image quality for the task at hand.

To facilitate this difficult duty, one has to utilize the most efficient way to extract anatomical information from the X-ray beam emerging from the patient. The X-ray detector is an integral component of the entire radiographic system specifically designed for this purpose. Therefore, the focus should be made on improving the detector's performance to provide sufficiently high image contrast at low radiation doses.

2 Flat panel detectors for X-ray medical imaging

For the best experience, the process of acquiring, viewing, and storing radiographic images must be accurate, safe, and fast. This became possible with the invention of digital X-ray detectors –

Flat Panel X-ray Imagers (FPXIs), that rendered the previous X-ray film, phosphor plate and X-ray image intensifier (XRII) technologies essentially obsolete. Indeed, in the past, starting from the first-ever radiograph obtained by Wilhelm Conrad Roentgen of his wife's hand in 1895, the radiologists had to load an X-ray film (which was single-use) into a cassette under the X-ray table, make the X-ray exposure, develop the film in a so-called dark room. Only after this long process could the radiograph be reviewed. This technology is not only time-consuming and labour-intensive but also creates inconvenient patient management and logistical hassle for storing and transferring the radiographs in a real clinical environment.

These problems were partially resolved by XRII technology introduced in the 1950s [4]. Instead of a flat X-ray film, it utilizes a rather bulky vacuum image intensifier which, when coupled to a television viewing system, transfers the X-ray image on a TV screen in real time. XRII/TV systems provided good image quality, especially at low radiation doses. This is especially critical for real-time fluoroscopic and angiographic procedures, since the cumulative exposure during the long-lasting procedure should be maintained at an adequate level, requiring the dose per frame to be significantly reduced.

With the development of digital solid-state FPXIs and their practical implementation in the 2000s, it became a dominant technology for radiography due to a number of benefits as will be discussed in the next sections [5–9]. (In this sense, the approach to the development of medical imaging technologies is similar to the approach to consumer electronics: vacuum electronics are replaced by solid-state ones). Ongoing research and development (R&D) in this field would only lead to even better image quality at a lower cost and with lesser sacrifices. Figure 2 schematically shows the typical FPXI.

The creation of an X-ray image is conceptually a three-step process. Firstly, the X-ray photons interact with an X-ray–sensitive medium and generate a measurable response that is proportional to the intensity of incident X-rays. Secondly, the response signal is integrated and stored on a storage capacitor. Finally, the electrical signal is recorded and reconstructed into a radiographic image.

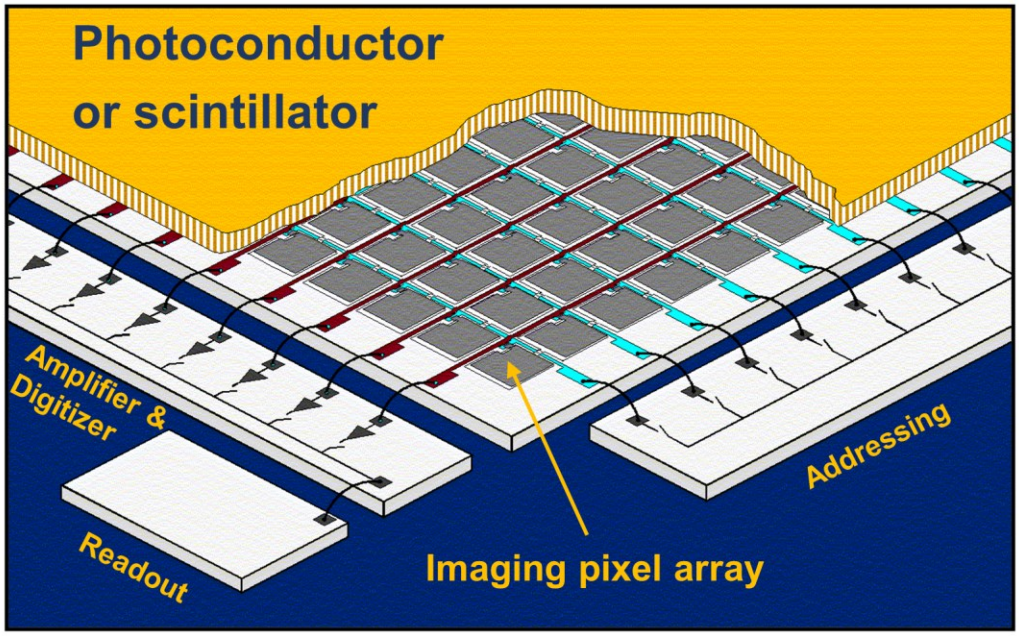

Figure 2. Schematic of the FPXI. (Image adapted from Philips Research Laboratories, Aachen.)

The X-ray–sensitive medium can be of either direct type (a photoconductor) or indirect type (a scintillator) (Figure 3), indicating that X-rays are converted into an electrical signal directly (X-ray photons – electrical charge) or with an intermediate step involving visible light (X-ray photon – scintillation optical photon – electrical charge), respectively. As this is depicted in Figure 3 (a), the FPXI of indirect conversion type utilizes a layer of a scintillator (phosphor) as an X-ray–sensing medium. Incident X-ray photons are absorbed in a scintillator layer and create multiple optical photons. The optical light propagates through the scintillator and impinges onto one of the photodiodes in the underlying imaging array, where it is converted to an electrical signal, which is stored and later read out by the imaging electronics. The most commonly used scintillators are doped gadolinium oxysulfide (Gd_2O_2S:Tb) and cesium iodide (CsI:Tl). Gd_2O_2S is a powdered (turbid) phosphor with a nearly uniform structure, and thus it allows a lateral spread of light, reducing the spatial resolution of the image. In contrast, CsI is a structured phosphor, which has needle-like closely packed crystallites that guide light towards the photodiodes and minimizes transversal propagation of light. Despite this, the indirect conversion FPXIs typically lack a high spatial resolution due to the omnidirectional propagation of scintillation optical photons.

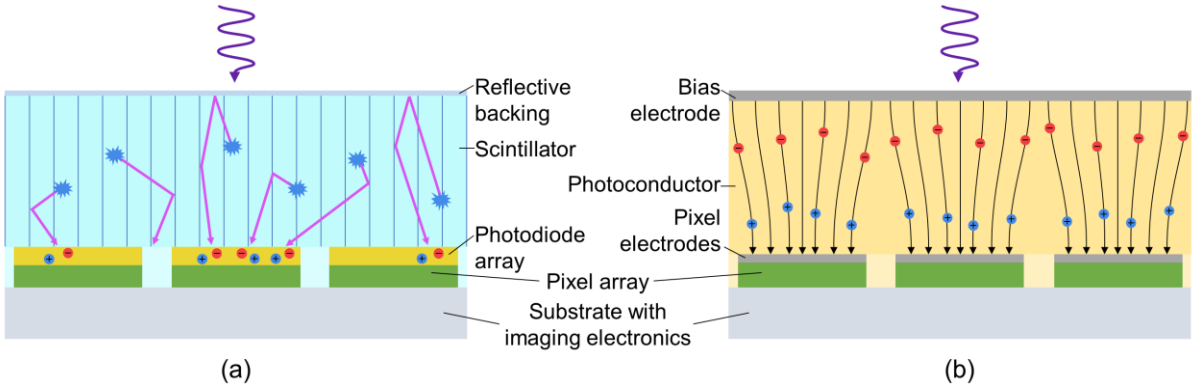

Figure 3. Schematic of the (a) indirect and (b) direct conversion detectors (not to scale).

In the direct conversion detectors, X-rays are absorbed in a photoconductor layer and directly create electrical charges – electron and hole pairs (Figure 3 (b)). These charges are separated by the application of a strong electric field, which directs carriers towards the opposite electrodes, where they are collected, stored, and finally read out by the imaging electronics. The detection process is direct in that the image information is transferred from X-rays directly to electrical charge without an intermediate stage.

Storing and recording of the electrical signal is performed by large-area integrated circuits with a thin film transistor (TFT) or complementary metal-oxide-semiconductor (CMOS) imaging pixel array and accompanying digital electronics [10]. These arrays are formed by conventional planar processing through the deposition and doping of the individual metal, insulator and semiconductor layers that are appropriately masked by the lithography process in each step. This process allows to obtain a monolithic imaging array with millions of small individual pixels of dimensions that are customized for the specific application. Each pixel has its own storage capacitor and transistor switch that is controlled by external electronics. The transistor is normally in the "off" state, allowing the X-ray–generated charge to accumulate in the capacitors. After the exposure, when the readout stage begins, the external electronics activate one line of pixels at a time by applying a small potential to that gate line, connecting storage capacitors to the source lines, and reading out the charge and converting it into an electrical signal. After each line of pixels is readout, the latent distribution of electric charges across the pixel array is reconstructed into a radiograph. Coupling an X-ray detection medium such as a scintillator or a photoconductor with a large-area imaging array forms the basis of the FPXI shown in Figure 2.

The FPXI based on the direct conversion approach has a higher potential to produce a superior image quality with a higher spatial resolution (no later spread of light) under lower X-ray doses (due to one-step conversion process) in comparison to the indirect conversion X-ray detector. In fact, the spatial resolution of the direct conversion detectors is limited by the pixel size only. This is, of course, true, when the right photoconductor suited for a particular detector application is used.

3 Photoconductors for direct conversion detectors

Let us consider what is expected from the "ideal" X-ray photoconductor [11,12].

(a) It should be technically feasible to produce large-area detectors with a photoconductive layer deposited directly on the imaging array. Crystalline semiconductors, such as cadmium zinc telluride (CZT), are not applicable for this purpose since no deposition technique will provide growth of a crystalline material on an imaging array. In contrast, disordered (polycrystalline and amorphous) photoconductors can be deposited on a TFT or CMOS imaging array at room temperature (or slightly elevated temperature, usually below 200 °C) without causing any damage to the array. Non-crystalline materials can be deposited by different techniques compatible with TFT and CMOS technologies, which will be discussed in the next section, and can produce uniform coatings of a large area.

An alternative approach to overcome the high-temperature growth limitation is to use a hybrid deposition method [13]. In this process, a photoconductor is either deposited on a separate blank substrate, typically glass or alumina (for polycrystalline materials) or it is grown as a single-crystal ingot (for crystalline materials). At this stage, the high deposition temperature does not possess any limitations since the substrate with imaging electronics is not yet involved. Following this step, the photoconductor is coupled to the readout circuitry via bump bonding. This process involves a very precise alignment of the photoconductor relative to the matrix array to achieve proper bonding of each pixel across the entire matrix area. This method is more technologically challenging, especially for high-resolution detectors with small (tens or hundreds of microns) pixel size and high pixel density. Additionally, single-crystalline photoconductors are grown in relatively small

ingots (several inches in diameter). As a result, to produce a large-area detector, a tillable array of multiple photoconductive crystals is required. This naturally increases technical complexity, cost of production, and therefore, is less favourable.

(b) Most of the incident radiation must be absorbed within a photoconductor layer. This means that over the X-ray energy range of interest, the attenuation depth should be much lower than the photoconductor thickness. Figure 4 demonstrates the attenuation coefficient for the main X-ray photoconductors investigated in the past two decades. It should be noted that the attenuation depth δ refers to the photoconductor's thickness sufficient to absorb only $\frac{I_{abs}}{I_0} = (1 - e^{-1}) \times 100\% \approx 63\%$ of the incident radiation. Therefore, for at least 95% absorption, the photoconductor thickness should be no less than 3δ.

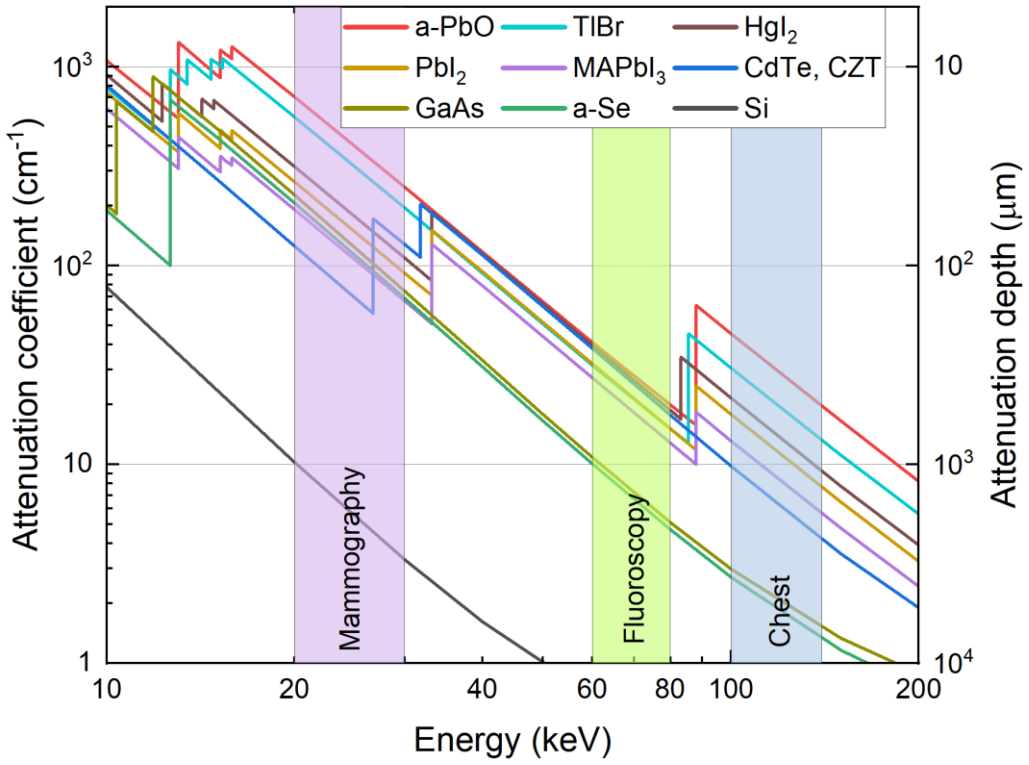

Figure 4. The attenuation coefficient and attenuation depth as a function of X-ray energy for different photoconductors. Data obtained from NIST database [14].

(c) A photoconductor must efficiently convert absorbed X-rays into an electrical signal and generate as many electron-hole pairs (ehps) as possible per every absorbed X-ray photon.

This requires high charge yield or, alternatively, low ehp creation energy $W_{\pm}$. $W_{\pm}$ characterizes the energy required to generate a single detectable pair of electron and hole. It was shown that the intrinsic (or, theoretical) $W_{\pm}^{0}$ is proportional to the bandgap of the photoconductor and follows Klein or Que-Rowlands rules (see Figure 5) that both can be approximated as $W_{\pm}^{0} \approx 3E_g$ [15]. However, in practice, for many photoconductors [16–19], experimentally measured (or, effective) $W_{\pm}$ is larger than $W_{\pm}^{0}$ and depends on the applied electric field. Relatively low $W_{\pm}$ at the practical electric field is an important requirement for an X-ray photoconductor.

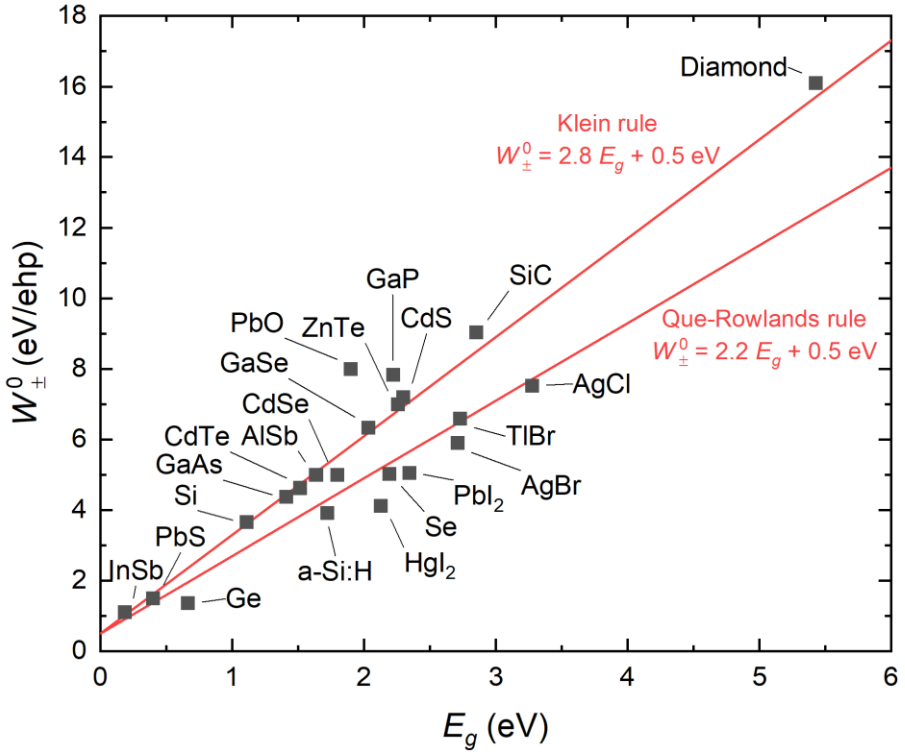

Figure 5. The theoretical electron-hole pair creation energy for different materials plotted as a function of the bandgap. Data obtained from [20,21].

(d) The photoconductor must have a low dark current, which is the main contribution of the detector's noise. This requires a wide bandgap to minimize the amount of thermally activated carriers. Additionally, a photoconductor must form non-injecting contacts with adjacent electrodes. It can be achieved by separating a photoconductor from the electrodes

by semi-insulating blocking layers that would allow the collection of the X-ray generated carriers of one sign from the photoconductor but will prevent injection of the oppositely charged carriers from the electrodes.

(e) The X-ray–generated carriers must be efficiently collected. This requires the schubweg of both electrons and holes to be larger than the detector's thickness. Schubweg s is the mean distance that carriers travels before undergoing trapping or recombination. It is given as a product of mobility μ, lifetime τ and electric field F: $s=\mu\tau F$. Therefore, a photoconductor must demonstrate sufficient mobility and lifetime of its charge carriers.

(f) A photoconductor must exhibit low surface conductivity, low lateral diffusion of carriers (in comparison to their drift), and high energy of K-edge (see next section) in order to preserve high spatial resolution.

(g) The properties of the photoconductor should not change or deteriorate with time. This requires a photoconductor that is stable in ambient conditions. If it is an issue, an additional technological step can be implemented to encapsulate a photoconductor from the atmosphere.

(h) When the intended application of the detector under consideration is in real-time imaging or 3D tomosynthesis, a photoconductor must have a fast response with very little signal lag – a residual current after exposure termination.

(i) The technological process of photoconductive layer deposition must be stable, reproducible, time-efficient, and cost-effective.

It is difficult to expect that one single material will satisfy each one of these requirements. A trade-off must be achieved between the charge yield and the dark current at a high electric field, or, in another example, sufficient X-ray absorption, which requires a certain thickness, and schubweg, which deteriorates with an increase in thickness. Alternatively, an engineering solution can be applied to improve one or several of these criteria, for example, by reducing a dark current via the development of a blocking layer structure, or by improving charge carriers transport via proper doping and alloying of the material. Finally, it should be noted that different clinical procedures have different requirements (detector area, energy range, read-out rate, etc.), therefore, a photoconductor must be tuned bearing a specific application in mind.

4 Interaction of X-rays with matter

When passing through matter, X-ray photons can be attenuated or pass through unaffected, as primary or direct radiation. Attenuation is caused via absorption or scattering, resulting in the local deposition of energy and the formation of a scattered or characteristic X-rays. The major interaction types are: (a) photoelectric absorption, (b) Compton scattering, (c) Rayleigh scattering, (d) pair production [1,2].

Photoelectric absorption

The photoelectric absorption is based on the photoelectric effect discovered by Albert Einstein in 1905. In the photoelectric effect, the incident photon interacts with an atomic electron, transferring all of its energy (Figure 6 (a)). If the photon's energy E_0 is greater than or equal to the binding energy BE of the electron, then it is ejected from the atom with the kinetic energy $KE = E_0 - BE$. Otherwise, the photoelectric interaction with that electron is not energetically feasible and will not happen.

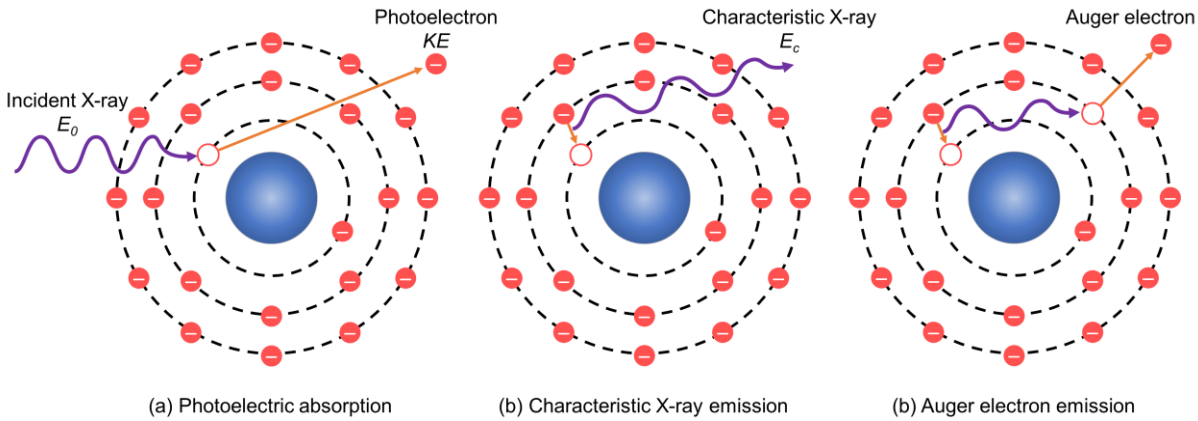

Figure 6. Schematic of (a) the photoelectric absorption, (b) the characteristic X-ray and (c) Auger electron emission processes.

If a photoelectric interaction is energetically unfeasible with K-shell electrons, it may still occur with an outer-shell electron. The photoelectric interaction has the highest probability when $E_0 = BE$ and afterwards decreases with increasing E_0. Although the probability of the photoelectric interaction decreases, in general, with increasing photon energy, it experiences an abrupt rise when

the photon energy overcomes the binding energy. For example, when the photon energy increases just past the binding energy of a K-shell electron (so-called K-edge), the photoelectric interaction with that electron becomes energetically feasible and photoelectric absorption probability increases sharply.

The photoelectric effect results in the ionization of the atom and the formation of a pair of electron and positively charged atom. The ejected photoelectron leaves a vacancy in the parent atom that will be filled by an outer-shell electron with lower binding energy, releasing a characteristic (fluorescent) X-ray with the energy equal to the difference in binding energies $E_c = \Delta BE$ (Figure 6 (b)) or Auger electron (Figure 6 (c)). This cascade process will repeat until the vacancy is left at the outermost shell where it is the most susceptible to be filled by a free electron.

The photoelectric process dominates when relatively low-energy X-ray photons interact with high-Z materials (Z – effective atomic number). Therefore, it is typically the main interaction mechanism in the X-ray detection medium of the detector, i.e., a photoconductor or a scintillator, which results in efficient conversion of X-ray photon energy into an electrical signal of the digital detector. However, if characteristic X-rays originate from high-Z materials, they have substantial energy to propagate finite distance in this medium, which plays a detrimental role in X-ray image quality.

Compton scattering

In a Compton scattering event, an incident X-ray photon with energy E_0 undergoes the inelastic (incoherent) scattering by an atomic electron, producing a scattered under the angle θ X-ray photon with energy $E_{sc} = \frac{E_0}{1+\frac{E_0}{m_0c^2}(1+\cos\theta)}$, where m_0c^2 = 511 keV is the rest mass of the electron, and an electron ejected from the parent atom with kinetic energy $KE_- = E_0 - E_{sc} - BE$ (Figure 7). Compton scattering results in the ionization of the atom and distribution of the incident photon's energy between the scattered photon and the recoil electron.

Compton scattering typically occurs at higher X-ray energies, where the binding energy of the atomic electron is much lower than the energy of the X-ray photon, and thus the Compton effect takes place with outer-shell electrons. Low-energy photons are mostly back-scattered ($\theta \approx 180°$) while high-energy X-rays have a higher probability of forward-scattering ($\theta \approx 0°$).

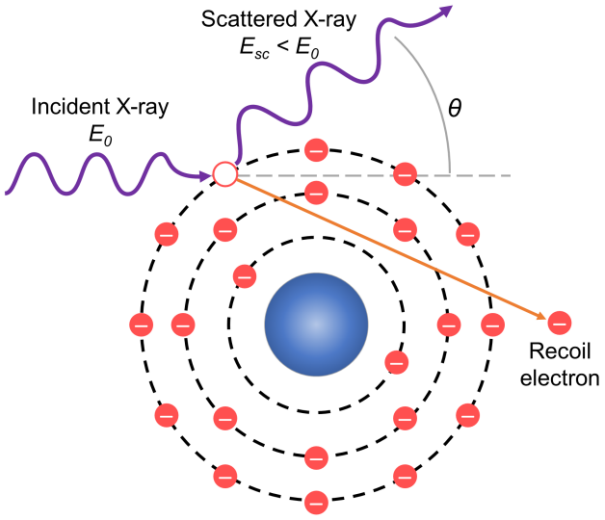

Figure 7. Schematic of the Compton scattering mechanism.

In the X-ray photon energies used in diagnostic imaging (10–140 keV), the incident photon energy is mostly transferred to the scattered photon, which, upon reaching the detector, cause a degradation of image contrast and an increase in random noise.

Rayleigh scattering

In a Rayleigh scattering event, an X-ray is elastically (coherently) scattered by an atom (Figure 8). In this process, ionization of the atom does not occur, and the energy of the scattered photon is preserved ($E_{sc} = E_0$), meaning that the X-ray energy is not deposited in the medium. However, the direction of propagation of the scattered X-ray photon changes relative to that of the incident photon. This has a detrimental effect in X-ray imaging, where the detection of scattered X-rays is undesirable. Higher energy X-rays are mostly forward-peaked, but low-energy X-rays undergo large-angle scattering. Rayleigh elastic scattering is more likely to occur for low-energy X-rays.

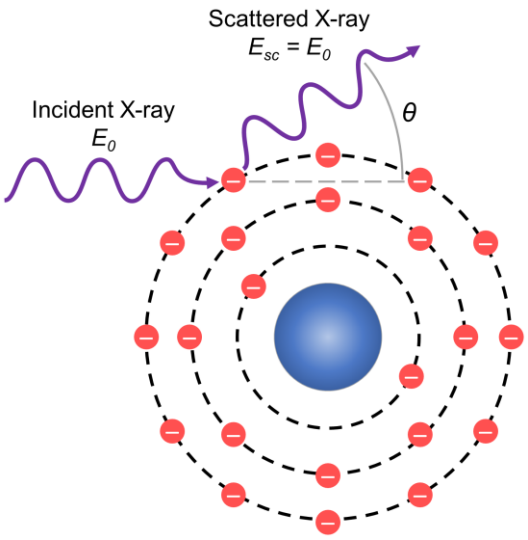

Figure 8. Schematic of the Rayleigh scattering mechanism.

Pair production

In a pair production event, an X-ray photon interacts with the atom's nucleus, gets absorbed, and produces an electron e^- and positron e^+ pair (Figure 9). The X-ray energy E_0 is spent toward the creation of an electron-positron pair ($2m_0c^2$) and their kinetic energies (KE_- and KE_+). Pair production can only occur when the energy of the X-ray exceeds the rest mass energy of the electron and positron $2m_0c^2 = 1022$ keV. It is interesting to note that the ionization of an atom does not occur, although charged particles (e^- and e^+) are created.

When the positron comes to rest, it annihilates with a negatively charged free electron (there is always an abundance of outer-shell electrons with low binding energy), resulting in the formation of two 511-keV gamma-photons ejected in nearly opposite directions. This effect is at the heart of the positron emission tomography (PET) modality, although the origin of the positron differs. In diagnostic X-ray imaging, pair production does not occur because of the high energy threshold.

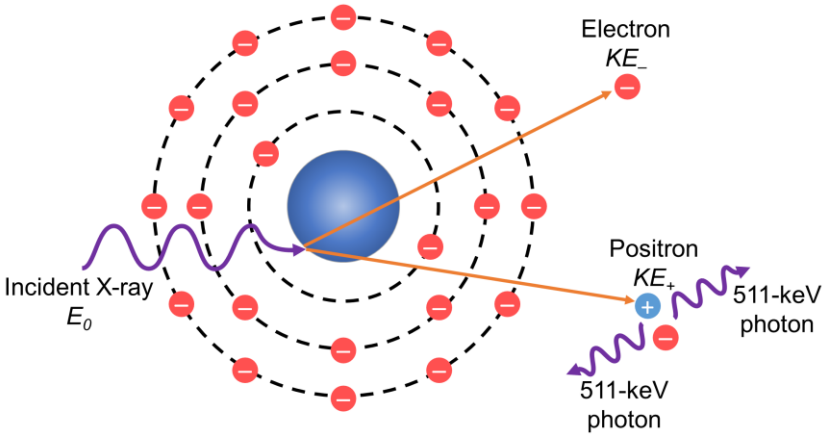

Figure 9. Schematics of the pair production mechanism.

Attenuation coefficients

All of the abovementioned interaction mechanisms result in the attenuation of the incident X-ray beam as it propagates through the matter by removal of the photons from the beam via absorption or scattering. The fluence of a beam after it passes through the medium is given by Lambert-Beers law:

$$N = N_0 e^{-\mu d}, \tag{1}$$

where N_0 is the incident fluence, d – thickness of the medium, and μ is the linear attenuation coefficient, which denotes the probability per unit of thickness, that an X-ray photon will be attenuated. The linear attenuation coefficient includes the probability of interaction from all mechanisms described above, and is the sum of the interaction probabilities of photoelectric absorption (τ), Compton (σ_c) and Rayleigh (σ_r) scattering, and pair production (π) interaction types:

$$\mu = \tau + \sigma_c + \sigma_r + \pi. \tag{2}$$

For a given X-ray photon energy, the linear attenuation coefficient is specific to each element, and thus, to each material. However, if mediums have the same elemental composition but different densities (water, ice, and vapours, for example), they will attenuate the X-ray beam differently. To account for this fact, the attenuation of the X-rays is conventionally characterized by a mass attenuation coefficient (μ/ρ). Therefore, the Lambert-Beers law can be rewritten as:

$$N = N_0 e^{-\left(\frac{\mu}{\rho}\right)\rho d}, \tag{3}$$

where ρd is usually referred to as mass thickness.

The mass attenuation coefficients are usually given for individual elements. For the compound consisting of a mixture of elements i with corresponding weight fractions w_i, the mass attenuation coefficient is the weighted (by weight) average of the elemental coefficients $(\mu/\rho)_i$:

$$\left(\frac{\mu}{\rho}\right)_{compound} = \sum_i w_i \left(\frac{\mu}{\rho}\right)_i . \quad (4)$$

Mass attenuation coefficient describes the efficiency of the removal of X-ray photons from the initial beam via different interaction mechanisms. However, only a fraction of these interactions results in a local deposition of energy as kinetic energy of electrons. Indeed, a Rayleigh-scattered photon does not transfer its energy; in Compton scattering, a portion of energy leaves the interaction site as a scattered photon. In photoelectric absorption, after the photon energy is transferred to the electron, the ionized atom can be de-excited by either ejecting secondary Auger electrons via non-radiative transitions and locally depositing energy, or by emitting a characteristic X-ray that leaves the interaction site. Mass-energy transfer coefficient (μ_{tr}/ρ) describes a fraction of the mass attenuation coefficient which contributes to the production of kinetic energy in charged particles in the medium. If energetic electrons subsequently produce a bremsstrahlung (braking) radiation as they decelerate in the medium, another portion of the energy is lost; the mass-energy absorption coefficient (μ_{en}/ρ) accounts for this difference. However, in the diagnostic energy range and for low-Z materials, the radiative losses are negligibly small and $(\mu_{tr}/\rho) \approx (\mu_{en}/\rho)$.

Figure 10 shows mass attenuation coefficients as a function of X-ray photon energy for two different cases: (a) soft tissue (a patient) and (b) lead oxide (a photoconductor in a digital detector). As soft tissue has a low density and consists mainly of low-Z elements (H, C, N, O), it has a relatively low photoelectric absorption efficiency, and thus, Compton scattering begins to dominate after ~30 keV. To remove these scattered photons, an anti-scatter grid is typically placed in between the patient and the detector, which inevitably reduces detected signal intensity. A photoconductor, in contrast, has a high density and high effective atomic number. This results in strong absorption of the incident X-rays (and, consequently, in a high digital signal) with a negligible scattering in the diagnostic X-ray energy range. The high energy of K-edge (~88 keV) also ensures that the characteristic (fluorescent) X-rays are not produced when photons with energies below this edge are used. The dashed lines in Figure 10 illustrate the mass-energy

absorption coefficients (μ_{en}/ρ), and the shaded areas indicate the energy range relevant to X-ray medical imaging.

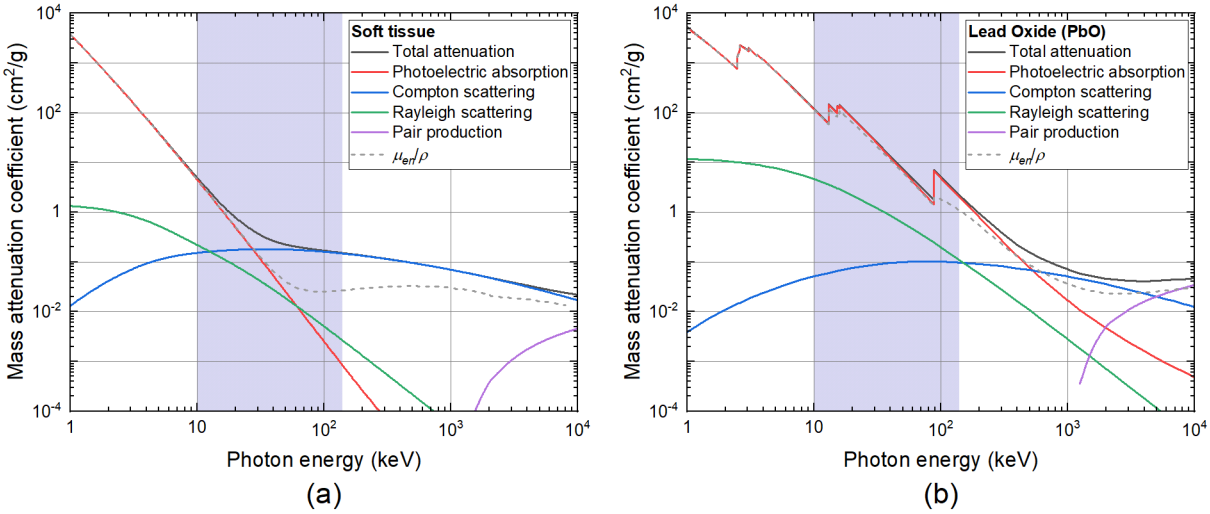

Figure 10. Mass attenuation and mass-energy absorption coefficients for (a) soft tissue and (b) lead oxide photoconductor. Data obtained from the NIST databases [13,23].

5 Research Objectives

The objective of this research is to undertake comprehensive materials science research into a new photoconductor material for X-ray imaging systems, namely amorphous Lead Oxide. The research goals carry both an applied and a fundamental character.

Applied purposes are:

(1) to advance a-PbO technology by developing a PbO-based blocking structure for enhanced stability under high electric field and reduced dark current while preserving fast temporal response and high X-ray sensitivity;

(2) to optimize the design of the X-ray–to–charge converter based on bilayer a-PbO/poly-PbO structure;

(3) to develop technology to the point that it will be ready for scaling up in order to produce large-area detectors with a photoconductive structure deposited directly on the imaging array.

A fundamental purpose is to clarify the physics of the charge generation-recombination mechanisms in this material which remain unclear despite the long-term discussion about the similar processes in other disordered photoconductors, including amorphous selenium (a-Se).

6 Dissertation outline

Chapter 1 provides a background on the medical X-ray imaging, flat panel X-ray imagers technology and their physical principles, as well as postulates the research objectives and structure of this dissertation.

Chapter 2 provides an overview of the progress in the science and technology of Lead Oxide photoconductors for application in the direct conversion X-ray imaging detectors. The deposition process, structural properties, and X-ray performance of both polycrystalline and amorphous polymorphs of Lead Oxide are presented.

Chapter 3 demonstrates a practical approach to the suppression of signal lag and dark current by developing a bilayer a-PbO/poly-PbO homostructure. The rationale behind this approach is discussed. Charge transport properties of the faster carriers (holes) and X-ray temporal response of this detector are investigated.

Chapter 4 demonstrates a practical approach to the dark current suppression by developing a PI/a-PbO blocking structure. Technical details of the blocking layer application are presented. The suppression of the dark current to an acceptably low level, as well as improvements in signal lag and adequate ghosting, are demonstrated.

In Chapter 5, the X-ray sensitivity of a-PbO photoconductor is analyzed and underlying mechanisms responsible for charge recombination in this material are examined. The electron-hole pair creation energy in a-PbO is measured in a wide range of electric fields, exposures, and X-ray energies. The role of the geminate, columnar and bulk recombination mechanisms in a-PbO photoconductor is discussed.

Chapter 6 concludes the dissertation, highlights the significance of the results, and provides suggestions for future work.

The topics discussed in Chapters 2–5 have been published or are currently in press in peer-reviewed journals and books, where the author of this dissertation is the first (main) co-author and his supervisor is the most senior co-author of the publications. Full texts of these publications are provided in each chapter, which constitute the main body of the dissertation.

7 References

[1] Beutel, J.; Fitzpatrick, J.M.; Horii, S.C.; Kim., Y.; Kundel, H.L.; Sonka, M.; Van Metter, R.L. Handbook of Medical Imaging, Volume 1. Physics and Psychophysics. SPIE, Bellingham, WA, USA (2000), doi: 10.1117/3.832716.

[2] Bushberg, J.T.; Seibert, J.A.; Leidholdt, E.M.; Boone, J.M. The Essential Physics of Medical Imaging, 3rd Ed. Lippincott Williams & Wilkins, Philadelphia, PA, USA (2012).

[3] Seeram, E. Digital Radiography. Physical Principles and Quality Control, 2nd Ed. Springer Singapore (2019), doi: 10.1007/978-981-13-3244-9.

[4] Coltman, J.W. Fluoroscopic Image Brightening by Electronic Means. *Radiology* 51, 359–367 (1948), doi: 10.1148/51.3.359.

[5] Rowlands, J.; Yorkston, J. Flat Panel Detectors for Digital Radiography. In *Handbook of Medical Imaging, Volume 1. Physics and Psychophysics*. SPIE, Bellingham, WA, USA; pp. 223–328 (2012), doi: 10.1117/3.832716.ch4.

[6] Seeram, E. Flat-Panel Digital Radiography. In *Digital Radiography. Physical Principles and Quality Control, 2nd Ed*. Springer, Singapore; pp. 65–85 (2019), doi: 10.1007/978-981-13-3244-9_4.

[7] Spahn, M. Flat detectors and their clinical applications. *Eur. Radiol*. 15, 1934–1947 (2005), doi: 10.1007/s00330-005-2734-9.

[8] Seibert, J.A. Flat-panel detectors: How much better are they? *Pediatr. Radiol*. 36, 173–181 (2006), doi: 10.1007/s00247-006-0208-0.

[9] Yaffe, M.J.; Rowlands, J.A. X-ray detectors for digital radiography. *Phys. Med. Biol*. 42, 1–39 (1997), doi: 10.1088/0031-9155/42/1/001.

[10] Zentai, G. Comparison of CMOS and a-Si flat panel imagers for X-ray imaging. *Proc. IEEE Int. Conf. Imag. Syst. Techn.,* pp. 194–200 (2011), doi: 10.1109/IST.2011.5962217.

[11] Kasap, S.O.; Frey, J.B.; Belev, G.; Tousignant, O.; Mani, H.; Greenspan, J.; Laperriere, L.; Bubon, O.; Reznik, A.; DeCrescenzo, G.; Karim, S.K.; Rowlands, J.A. Amorphous and Polycrystalline Photoconductors for Direct Conversion Flat Panel X-Ray Image Sensors. *Sensors* 11, 5112–5157 (2011), doi: 10.3390/s110505112.

[12] Kabir, M.Z.; Kasap, S. Photoconductors for X-Ray Image Detectors. In Springer Handbook of Electronic and Photonic Materials. Springer, Cham; pp. 1125–1147 (2017), doi: 10.1007/978-3-319-48933-9_45.

[13] Adachi, S.; Hori, N.; Sato, K.; Tokuda, S.; Sato, T.; Uehara, K.; Izumi, Y.; Nagata, H.; Yoshimura, Y.; Yamada, S. Experimental evaluation of a-Se and CdTe flat-panel x-ray detectors for digital radiography and fluoroscopy. *Proc. SPIE* 3977, 38–47 (2000), doi: 10.1117/12.430924.

[14] Berger, M.J.; Hubbell, J.H.; Seltzer, S.M.; Chang, J.; Coursey, J.S.; Sukumar, R.; Zucker, D.S.; Olsen, K. XCOM: Photon Cross Sections Database (2010). Available online: http://physics.nist.gov/xcom.

[15] Que, W.; Rowlands, J.A. X-ray photogeneration in amorphous selenium: Geminate versus columnar recombination. *Phys. Rev. B* 51, 10500–10507 (1995), doi: 10.1103/PhysRevB.51.10500.

[16] Bubon, O.; Jandieri, K.; Baranovskii, S.D.; Kasap, S.O.; Reznik, A. Columnar recombination for X-ray generated electron-holes in amorphous selenium and its significance in a-Se x-ray detectors. *J. Appl. Phys*. 119, 124511 (2016), doi: 10.1063/1.4944880.

[17] Semeniuk, O.; Grynko, O.; Decrescenzo, G.; Juska, G.; Wang, K.; Reznik, A. Characterization of polycrystalline lead oxide for application in direct conversion X-ray detectors. *Sci. Rep*. 7, 8659 (2017), doi: 10.1038/s41598-017-09168-3.

[18] Grynko, O.; Thibault, T.; Pineau, E.; Reznik, A. The X-ray Sensitivity of an Amorphous Lead Oxide Photoconductor. *Sensors* 21, 7321 (2021), doi: 10.3390/s21217321.

[19] Xu, X.; Qian, W.; Xiao, S.; Wang, J.; Zheng, S.; Yang, S. Halide perovskites: A dark horse for direct X-ray imaging. *EcoMat* 2, e12064 (2020), doi: 10.1002/eom2.12064.

[20] Kasap, S.O.; Rowlands, J.A. X-ray photoconductors and stabilized a-Se for direct conversion digital flat-panel X-ray image-detectors. *J. Mater. Sci. Mater. Electron*. 11, 179–198 (2000), doi: 10.1023/A:1008993813689.

[21] Kasap, S.O.; Rowlands, J.A. Direct-conversion flat-panel X-ray image sensors for digital radiography. *Proc. IEEE* 90, 591–604 (2002), doi: 10.1109/JPROC.2002.1002529.

[22] Toda, H. Fundamentals of X-Ray Imaging. In *X-Ray CT: Hardware and Software Techniques*. Springer, Singapore; pp. 17–49 (2021), doi: 10.1007/978-981-16-0590-1_2.

[23] Hubbell, J.H.; Seltzer, S.M. Tables of X-Ray Mass Attenuation Coefficients and Mass Energy-Absorption Coefficients from 1 keV to 20 MeV for Elements Z = 1 to 92 and 48 Additional Substances of Dosimetric Interest (2004). Available online: http://physics.nist.gov/xaamdi.

Chapter 2

Progress in Lead Oxide photoconductors for digital direct conversion X-ray imaging detectors

This topic has been elaborated in the following publication:

Oleksandr Grynko, Alla Reznik. Progress in Lead Oxide X-ray Photoconductive Layers. In *Photoconductivity and Photoconductive Materials: Fundamentals, Techniques and Applications* (ed. Safa Kasap). John Wiley & Sons, Ltd; Chapter 16 (2022); in print.

Selected sections of the publication are listed below.

Photoconductivity and Photoconductive Materials:
Fundamentals, Techniques and Applications

Edited by Safa Kasap

John Wiley & Sons, Ltd © 2022

Chapter 16

Progress in Lead Oxide X-ray Photoconductive Layers

Oleksandr Grynko

Department of Physics, Lakehead University, Thunder Bay, Ontario, Canada

Alla Reznik

Department of Physics, Lakehead University, Thunder Bay, Ontario, Canada

Thunder Bay Regional Health Research Institute, Thunder Bay, Ontario, Canada

1. Introduction

Many of the existing X-ray and gamma-ray detectors and imaging systems rely on indirect conversion of radiation into a signal, i.e., where a scintillator first converts X-ray quanta into optical photons, which in turn diffuse through a phosphor (e.g., CsI or Gd_2O_2S) and then are converted back to electrons by an array of photodiodes [1,2]. This two-step conversion process reduces the X-ray–to–charge conversion gain and as a result, these detectors are quantum limited, so the signal-to-noise ratio (SNR) for a given pixel is proportional to the square root of the number of detected X-rays. Subsequently, at the lowest exposure levels common in fluoroscopy (0.1–1 μR/frame) electronic noise dominates over the quantum noise and therefore, the visibility of low contrast objects is compromised. In addition, diffusion of optical photons in the scintillator reduces

the spatial resolution of the indirect conversion detectors [3,4]. An alternative detection scheme is a direct conversion [5], i.e., where X-rays are absorbed in a semiconductor that directly creates electron-hole pairs (EHPs), which in turn are subsequently separated by a bias field to generate a signal. The charges are moved by an electric field, making it possible to create an image with a thick detector layer without significant loss of resolution. The benefits inherent to direct conversion are high spatial resolution that is limited only by pixel size and improved adherence to the As Low As Reasonably Achievable ("ALARA") patient dose recommendation, as required by X-ray imaging clinical practices. Commercial Flat Panel X-ray Imagers (FPXIs) for mammography, with a layer of amorphous selenium (a-Se) as an X-ray–to–charge transducer, opened a new era in breast imaging due to the supreme detectability of small breast lesions, illustrating the enormous potential for direct conversion detectors in X-ray imaging [5–7].

The two major components of FPXIs are a large area thin-film transistor (TFT) or complementary metal-oxide-semiconductor (CMOS) active-matrix array (as used in flat panel displays, for example), and a photoconductive layer which is deposited directly onto the imaging array and acts as an X-ray–to–charge transducer (Figure 1). Currently, stabilized a-Se is the only commercially viable large-area-compatible X-ray photoconductor in direct conversion X-ray detectors due to its several distinct advantages over potentially competing photoconductors. Both X-ray generated electrons and holes can be made to drift in a-Se, the dark current can be appropriately controlled by the use of blocking structures, and the X-ray attenuation coefficient, while not outstanding, is acceptable for the relatively soft X-rays in the mammographic energy range. Therefore, the most successful application of stabilized a-Se technology is in mammography, where a-Se large area flat panel detectors became a dominant technology. For higher energy applications like fluoroscopy, a-Se does not have enough X-ray stopping power and alternative materials are needed to expand the success of the direct conversion scheme over the diagnostic energy range. In this regard, alternative and technologically feasible X-ray photoconductors with higher effective atomic numbers that can be easily interfaced with readout electronics are needed.

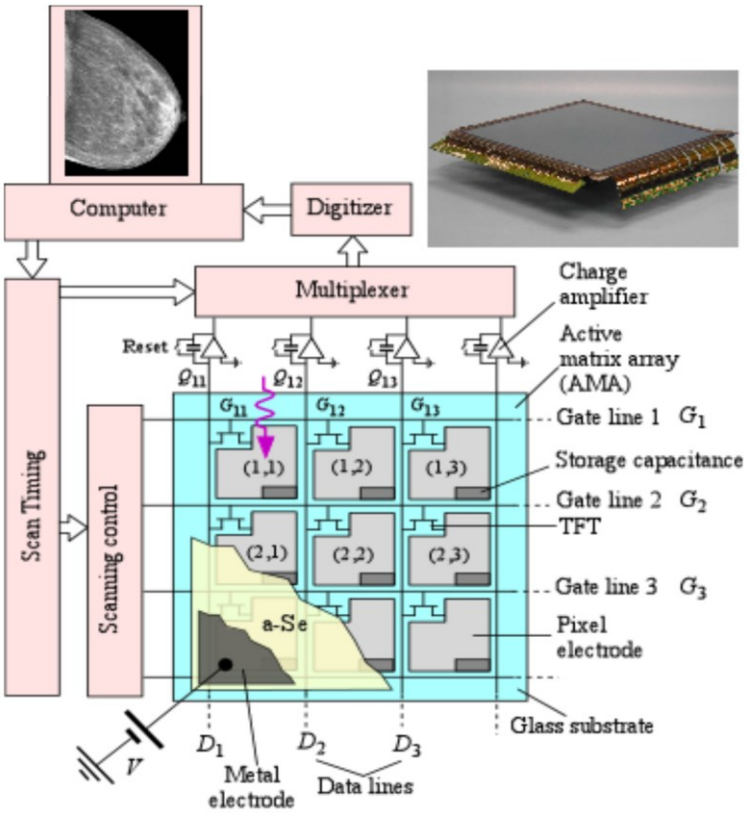

Figure 1. A simplified schematic illustration of a direct conversion FPXI and its peripheral electronics that drive the sensor operation [6].

When choosing an optimal photoconductive material for direct conversion detectors two major factors should be considered: (1) X-ray–to–charge conversion efficiency and (2) technical feasibility to be deposited over the imaging electronics, under deposition conditions suitable for imaging substrates. Additionally, if the photoconductor is considered for application in real-time imaging, it should demonstrate adequate temporal response without signal lag, i.e., a residual current after X-ray exposure is terminated. Since X-ray imaging detectors should normally have a large active area (one cannot converge X-rays), single-crystalline photoconductors are ruled out from the consideration. Thus, it is imperative to focus on amorphous and polycrystalline phases of high-*Z* photoconductors, that can be directly deposited on a large-area imaging array without causing permanent damage. Potential X-ray photoconductors such as polycrystalline layers of BiI_3 [8,9], PbI_2 [10–12], HgI_2 [12–14], ZnO [15], CdTe [16], $Cd_{1-x}Zn_xTe$ [17], and PbO [18] have been investigated and have shown potential for use in direct conversion detectors. The X-ray–to–charge conversion rate of these materials is 3–8 times larger than that of a-Se and thus, potentially they

are capable of X-ray quantum noise limited operation at low exposures, since the X-ray quantum noise can prevail over the electronic noise. However, the level of lag in these materials is too high: for example, $Cd_{1-x}Zn_xTe$ and CdTe show 10–70% lag at 30 frames per second (fps) read-out [16,19–21], PbI_2 and HgI_2 have lag of 10–30% at 2–5 fps [12,22,23], and poly-PbO demonstrated 4–9% lag at 1 fps [18]. The presence of this residual signal has a detrimental effect on real-time procedures, since part of the signal from previous exposures combines with the consecutive one. The resulting image can be inaccurate and misleading and as such can compromise the whole visualization advantage of real-time (fluoroscopic) imaging. For practical fluoroscopic applications, the residual signal should promptly decay to a level well below 10% in less than 33 ms [21,24–27]. Other problems of these photoconductors are incomplete charge collection and high dark current (or a combination of both). Therefore, material science and engineering solutions are needed to be applied to bring the technologies and properties of these promising materials to the "detector grade" level.

Another class of materials that is rapidly gaining popularity for applications in photonics and optoelectronic devices and potentially can be a game-changing approach to medical X-ray detectors are perovskite semiconductors [28]; however, they are still at a very early stage of development. Most of the perovskites are limited by comparatively high dark current, signal lag, material instability, and technological difficulties in manufacturing a thick and uniform layer over a large area. Therefore, at the current state of technology, they are not mature enough to be considered as a practical solution to improve radiation medical imaging.

Among the potential X-ray–to–charge transducers listed above, Lead Oxide (PbO) has a special place. Lead Oxide has three distinct advantages over a-Se. To start, it has higher X-ray detection efficiency than a-Se due to its higher Z_{eff} and thus permits effective absorption of higher energy X-rays with a thinner layer. Furthermore, it has a lower theoretical EHP creation energy, and hence a higher X-ray-to-charge conversion gain. Finally, the high energy of the absorption edge (K-edge) results in constant contrast between bones and soft tissues in a much broader range of X-ray tube voltages (kVp settings) as compared to other materials. Therefore, Lead Oxide can be considered as an alternative to an a-Se photoconductor [5,6,29–32].

PbO exists in two polymorphs which both can be deposited over large-area imaging substrates: polycrystalline Lead Oxide (poly-PbO) which is deposited with the basic thermal evaporation

method, and a newer non-crystalline polymorphic form of the material – amorphous Lead Oxide (a-PbO), deposited by ion-assisted thermal deposition i.e., with simultaneous energetic ion bombardment of the growing layers. Interestingly, poly-PbO, like a-Se has a long history of commercial utilization in optical imaging. Previously, thin layers of poly-PbO were employed in so-called Plumbicon video pick-up tubes that were extensively used for broadcast and fluoroscopy and digital subtraction angiography in conjunction with image intensifiers. Due to the exceptional photoconductive properties of poly-PbO, Plumbicon gave rapid response and high-quality pictures at low light levels. In 1967, the Academy of Television Arts and Science awarded Philips an Emmy Award for "Outstanding Achievements in Engineering Development" for the invention of the Plumbicon tube. The principle of Plumbicon vacuum pick-up tubes utilizing poly-PbO photo-targets involves the following. Optical photons impinging on the poly-PbO photoconductive layer are absorbed at the incident poly-PbO surface and create free EHPs. Under the influence of the applied field, holes are drawn across the poly-PbO and are collected on the back surface where they form a latent charge image that is subsequently readout using a scanning electron beam. In this configuration with electron beam read-out, poly-PbO showed no signal lag [33–35].

For use in medical imaging systems, electron beam readout has to be replaced by a two-dimensional array of pixel electrodes. However, the implementation of electronic readout to a poly-PbO photoconductor in a non-vacuum environment has several technological challenges. First, poly-PbO layers are highly porous and unstable at ambient conditions thus requiring a protective sealing to be applied immediately after the deposition. Also, interfacing a poly-PbO layer with pixelated metal electrodes results in signal lag. Reported signal lag is probably the major constraint for the application of poly-PbO in real-time imaging and restricts its application to static imaging only (radiology) [29,36].

In contrast to poly-PbO, its more disordered, amorphous PbO counterpart, grown by ion-assisted thermal deposition is more attractive for application in the direct conversion detectors [37]. It is dense, capable of withstanding higher electric fields with lower dark current and exhibits no signal lag [30].

Here we present an overview of the recent advances in Lead Oxide technology for application in the direct conversion X-ray imaging detectors. The technological step that led to the growth of lag-free material, namely a-PbO, and the underlying mechanisms that allowed the transition from

structurally disordered poly-PbO to a homogeneously structured a-PbO, will be discussed. The peculiarities of the electro-optical and X-ray performance of both PbO polymorphs will be thoroughly examined and compared to those of other photoconductors currently in use or under intensive research. A practical approach to the PbO-based detectors for a variety of clinical and industrial application including multilayer a-PbO/poly-PbO and Polyimide/a-PbO blocking structures will be demonstrated.

2. Deposition process of PbO layers

Like many other materials, PbO can be grown by a wide variety of methods. Table 1 below summarizes the techniques and the main deposition parameters for the growth of different PbO structural configurations.

Since currently the most promising application of PbO is in medical X-ray detectors, where a uniform layer of a photoconductor has to be directly deposited on the TFT or CMOS imaging array, recent research efforts were focused on the development of PbO deposition techniques that allow the depositing of large-area uniform layers without damaging the imaging electronics. The major requirements to the deposition process are:

1. The deposition process should provide a uniform coating over a large area (~25×30 cm^2 for breast imaging and ~43×43 cm^2 for chest imaging) [18,38];
2. The substrate temperatures should be kept below ~200–250 °C [39];
3. The deposition rate should be not less than ~0.5 μm/min for a cost-efficient process.

The first condition comes from the fact that the detector is typically placed right behind the object to be imaged, or a patient, and therefore, the active area of the X-ray imaging detector has to be at least of the same size as the object (since one cannot effectively focus X-rays). The second condition prevents irreversible damage to the TFT and CMOS imagers, that negatively alters their operating parameters [40], possibly caused by the high temperature.

Table 1. Overview of known PbO deposition techniques.

Deposition technique	Solid type	Substrate temperature (°C)	Area	Deposition rate (μm/min)	Ref.
Czochralski method	Single crystal	~870	2×2×2 cm^3	33–83	[41]
Hydrothermal method	Single crystal	400	1×1×0.1 mm^3	Not specified	[42]
Electrochemical method	Microcrystalline film	80	Depends on anode size	~10	[43,44]
Spray pyrolysis	PbO film *	300	2.5×7.5 cm^2	~0.004	[45]
Sputter deposition	PbO film *	Not specified	Not specified	0.01–0.1	[46,47]
Particle-in-binder	PbO film *	25–500	2.5×2.5 cm^2	Not specified	[48]
Chemical vapor deposition (CVD)	Polycrystalline film	400–800	10 inch in diameter	0.015	[49,50]
Laser assisted deposition (LAD)	Polycrystalline film	150–300	Not specified	5–20	[51]
Vacuum thermal evaporation	Polycrystalline film	100	18×20 cm^2	~1–2	[18,36]

* the film is not single-crystalline, but further details on the structure were not specified.

The low-temperature and large-area deposition requirements significantly constrain the choice of deposition method and the type of solids to be used. Indeed, the methods for growing single-crystalline materials require a much higher temperature than imaging electronics can withstand. Alternative methods using a hybrid deposition technique, where the photoconductor is first grown on the glass or alumina substrate and then coupled to the readout circuitry are also less practical, since the latter involves very precise alignment of the photoconductor relative to the matrix array to achieve proper pixel-to-pixel bonding that is technologically challenging and makes the detector fabrication very expensive, especially for large-area high-resolution detectors. Therefore, single-crystalline photoconductors are removed from consideration.

Alternatively, most of the non-crystalline deposition techniques allow direct deposition on large-area substrates, but with a few limitations. Chemical vapour deposition (CVD) and spray pyrolysis utilize high substrate temperature. CVD, spray pyrolysis, and sputtering depositions have slow deposition rates. The laser assisted deposition (LAD) lacks uniformity for large-area coatings. Electrochemical methods require submerging an imaging substrate into an aqueous solution which is not feasible. The particle-in-binder technique uses a gel paste prepared by mixing particles with a special binder and deposited on the substrate. However, this method might also be impractical, since it is hard to control the quality and thickness of the layer across the large area of the imager. Overall, all of the deposition techniques discussed above have pitfalls that prevent their practical utilization in the fabrication of large-area uniform layers of X-ray photoconductors. The only other technique that can satisfy all of the deposition criteria is thermal evaporation in vacuum, a common method of physical vapour deposition (PVD).

Thermal deposition of the polycrystalline Lead Oxide layer was pioneered by the Philips Research Laboratories in the early 1960s [35] for the growth of relatively thin poly-PbO layers (~5–20 μm) to make optical targets in the Plumbicon television pick-up tubes. In the 2000s, with a resumed interest in photoconductive materials for application in X-ray imaging, Simon et al at Philips Research Laboratories scaled up the deposition process to obtain a 340-μm thick layer of poly-PbO, required for the efficient absorption of diagnostic X-rays [18,36,52].

The schematics of the thermal evaporation process is shown in Figure 2. During the thermal deposition, high purity (5N) PbO powder is evaporated from a crucible at ~1000 °C (melting point of PbO is ~890 °C) onto the substrate held at ~100 °C with a relatively high deposition rate of ~1–2 μm/min [18,36,52,53]. The deposition takes place in a background atmosphere of molecular oxygen at ~3 mTorr, which is required for proper layer stoichiometry. The bulk of the layer consists mainly of the red tetragonal lead oxide (α-PbO) (with a small fraction of yellow orthorhombic β-PbO), but a seeding layer at the first few microns of the film is formed mostly by β-PbO [54].

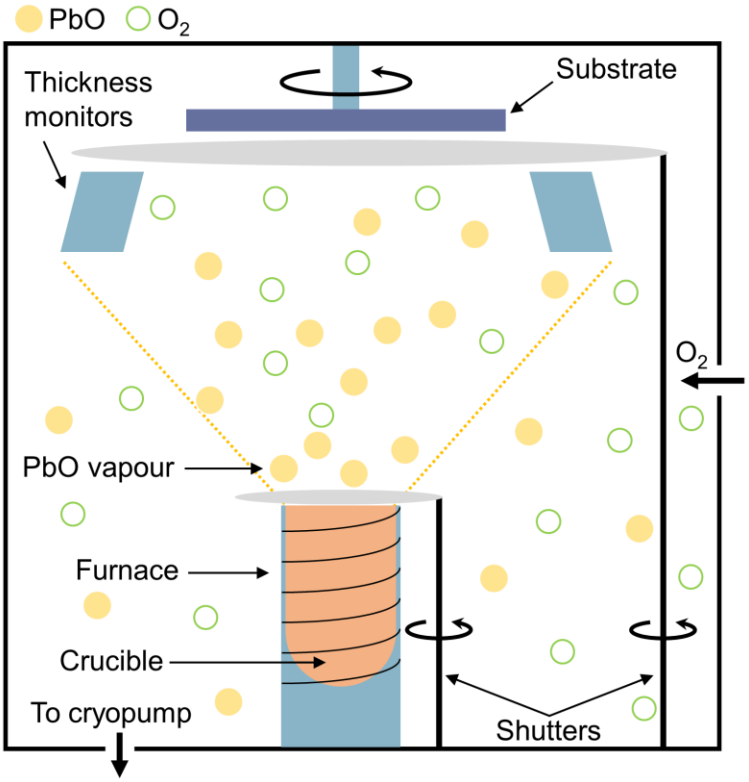

Figure 2. Schematic description of the conventional thermal evaporation process [53]. (Used with permission.)

Poly-PbO deposited by thermal evaporation has a very peculiar structure: poly-PbO layers are composed of randomly oriented platelets, or grains, which are several microns in diameter and around a hundred nanometers thick (Figure 3) [53,55]. As seen from the scanning electron microscopy (SEM) images in Figure 3, these platelets are oriented largely along the growth direction, but randomly arranged within a plane. The platelet structure results in high micrometre surface roughness (as defined by the platelets size) and high porosity of the grown layers. High porosity significantly reduces the packing density of the poly-PbO (up to 50% of single-crystal density). It should be noted that the morphologies of poly-PbO layers reported in different publications are very similar [18,53,55] suggesting high reproducibility of the basic thermal evaporation process.

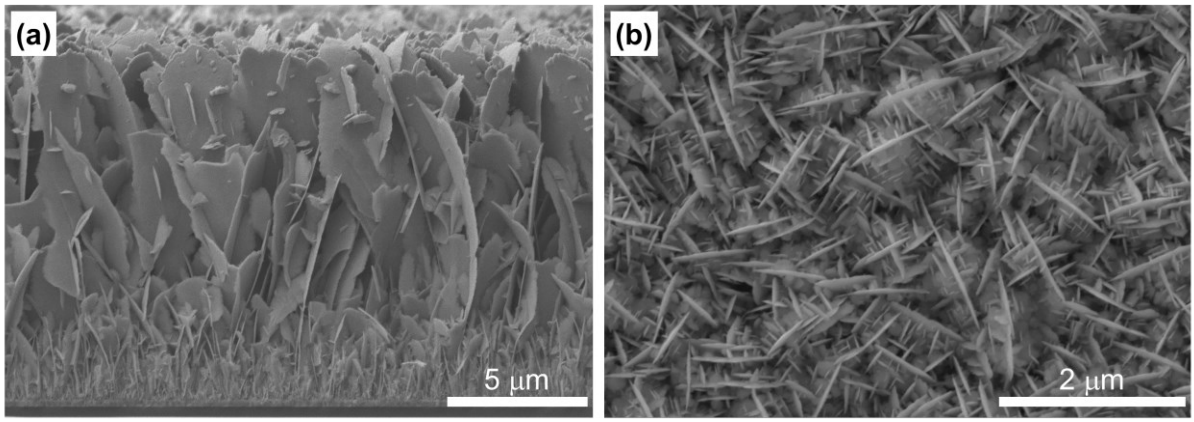

Figure 3. (a) The SEM cross-sectional view of the poly-PbO. (b) The surface of the poly-PbO layer with visible individual platelets [53]. (Used with permission.)

Similar to many other metal oxides, poly-PbO layers grown by thermal evaporation suffer from some degree of non-stoichiometry. Figure 4 shows the X-ray photoelectron spectroscopy (XPS) spectra of the poly-PbO layer measured on the surface and in the bulk of the layer at different depths [53]. The surface is over-oxidized as indicated by the presence of both PbO and PbO_2 phases. In the bulk, Pb-O remains the dominant bonding configuration, but some oxygen deficit (as indicated by the presence of un-oxidized Pb atoms) is evident from the spectra. This is not surprising considering the relatively low theoretical formation energy of oxygen vacancies and their high solubility in the grown layers [56].

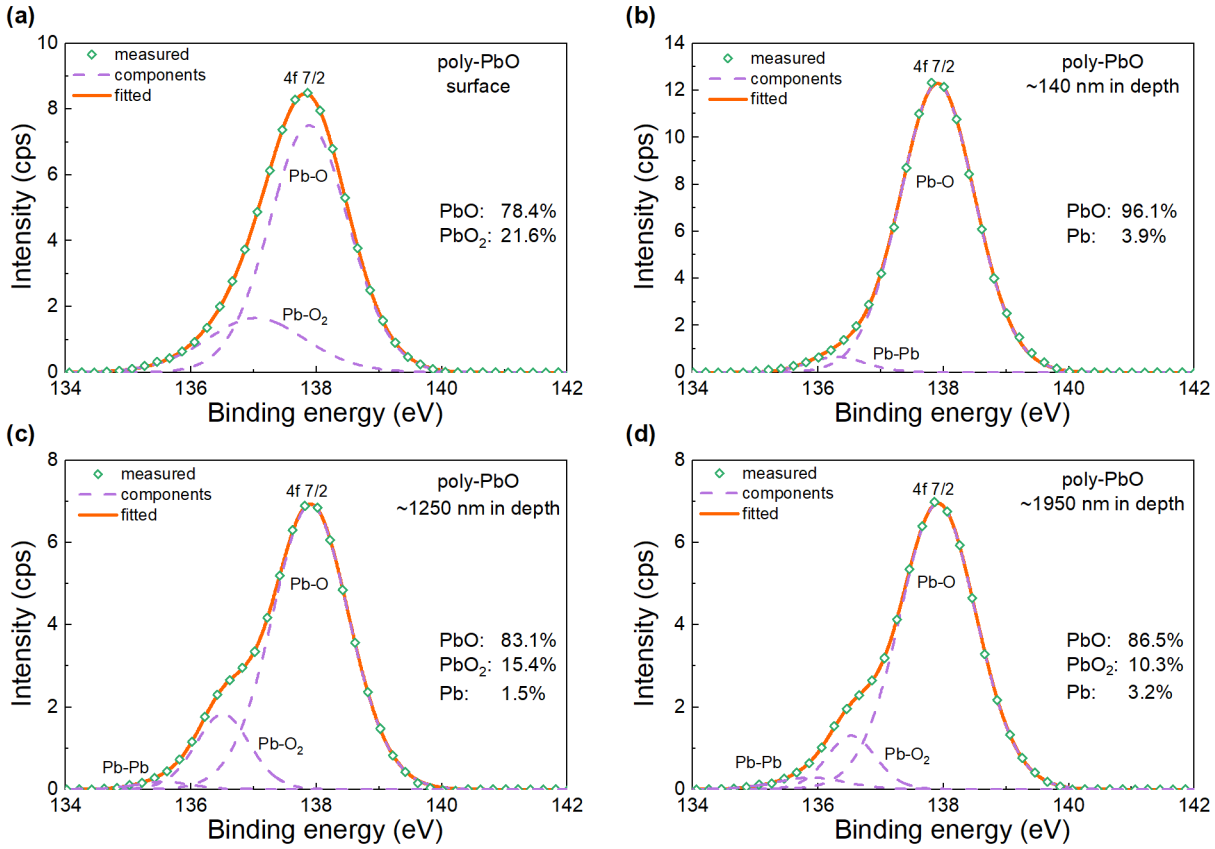

Figure 4. XPS spectra of poly-PbO at a surface and at selected depths [53]. (Used with permission.)

In a simplified way, the low packing density, poor sample stability and non-stoichiometry of the PbO-layers grown by thermal evaporation can be explained in terms of the so-called structure zone diagram (SZD) model [57–59 and references therein]. In this model, the effect of different deposition parameters on structural imperfections is reduced to consider only the homologous temperature, T^*, that is the layer growth temperature normalized by the melting temperature of the deposited layer material, T_{melt}. Since it is difficult to measure the layer temperature during a deposition process, it is normally replaced by the substrate temperature, T_{sub}, and T^* is estimated as $T_{\mathrm{sub}}/T_{\mathrm{melt}}$ (K/K). In order to achieve a highly-packed layer during evaporative deposition, T^* should be higher than ~0.6, which corresponds to Zone 3 of the temperature regime [58,59] (the closer this ratio is to unity, the more refined structure is obtained due to increased adatom mobility and surface diffusion). At substrate temperatures which correspond to Zone 1 with $T^* < 0.3$, the adatom mobility is low; this leads to continued nucleation of grains and as a result, to the growth

of a textured structure consisting of fibrous grains growing in the direction of the incoming vapour flux [57]. Since the melting temperature of PbO is ~890 °C, its temperature regime for the deposition over imaging readout electronics at T_{sub}~200 °C corresponds to T^{*}~0.4. Although this is slightly beyond Zone 1 of the SZD model, a high porosity and a platelet structure of grown poly-PbO layers strongly resemble the fine-grained structure of textured and fibrous grains typical to Zone 1, and can be attributed to the limited mobility of the material on the surface of the growing layer and insignificant diffusion of atoms in the bulk of the layer under low-temperature deposition [60–62].

Thus, the conventional thermal deposition of the PbO layer over imaging electronics has an inherent problem of large thermal mismatch between the PbO vapour and the substrate, which causes the formation of the porous structure with a network of individual platelets. Raman spectroscopy indicates that the platelets are composed of highly crystalline material with a predominance of tetragonal α-PbO phase in the bulk [53].

To obtain a dense and more homogeneous film, the deposition regime should correspond to Zone 3 with $T^{*} > 0.6$. To achieve this, the substrate temperature must be maintained at ~600 °C that is well above the thermal tolerance of most commercial image readout electronics.

A plausible approach to solving a problem of the large mismatch between T_{sub} and T_{melt} during the PbO deposition process, is to apply the so-called ion-assisted deposition that is thermal evaporation with low-energy oxygen ion bombardment. The key difference from the conventional thermal deposition, is that the deposition takes place in the atmosphere of *ionized oxygen*, instead of *molecular oxygen* (Figure 5 (a)). Oxygen ion bombardment can be delivered by a specialized ion source with either a hot filament or a hollow-cathode electron emitter (Figure 5 (b)). The latter provides much better control of the emission current and offers a significantly longer operational time interval before maintenance in comparison to the hot filament electron source. The gas to be ionized is admitted to the ion source between the magnet and the small base of the conical anode at a controlled flow rate. As voltage is applied between the anode and cathode, electrons emitted from the cathode are accelerated by the applied electric field and bombard the gas, producing ions.

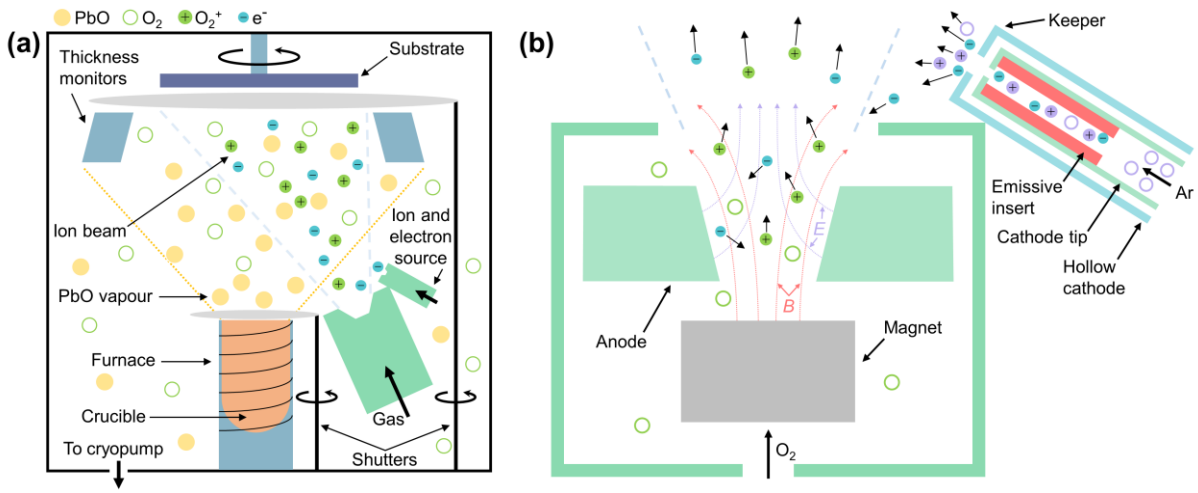

Figure 5. (a) Schematic description of the advanced ion-assisted thermal evaporation process. Oxygen gas is supplied to the chamber through an ion source [53]. (Used with permission.) (b) The cross-section of the End-Hall ion source with the Hollow-Cathode electron emitter (cathode).

Most ion sources work with singly charged ions, for instance, N_2^+ and O_2^+ for nitrogen and oxygen, respectively [63]. The magnet provides a divergent DC magnetic field that impedes the mobility of electrons as they drift to the anode, thus increasing their lifetime in the plasma. This results in a spatially distributed plasma potential field that accelerates ions away from the source. The energy of the accelerated ions depends on where they were created along the spatial potential field, but the mean ion energy is ~60–70% of the anode voltage. The fraction of electrons that do not participate in gas ionization, serves as the neutralization for the ion beam [64,65]. The ion source allows for independent control of oxygen ion energy and ion current density, required to achieve the desired structural modifications of a growing layer.

During the ion-assisted thermal evaporation, the substrate is being simultaneously coated with material vapours and bombarded with ions (Figure 6 (a)). Quantitatively, this process can be characterized by the ion arrival rate R_i (atoms/cm^2/s) and the atom arrival rate R_a (ions/cm^2/s) [63]:

$$R_i = \frac{J_i}{1.6 \cdot 10^{-19}}, \quad R_a = \frac{r \times \rho \times N}{1.66 \cdot 10^{-24} \times w} \times 10^{-8}, \tag{1}$$

where J_i (A/cm^2) – ion current density that is given by the specifications of the ion source and the discharge current, r (Å/s) – deposition rate, ρ (g/cm^3) – deposited film density, N – number of

atoms in a molecule, w (amu) – molecular weight of the material being deposited [63,66]. The ion/atom arrival ratio, multiplied by the ion energy E_i (eV) gives one of the most important parameters to consider in the ion-assisted applications, an ion-assist energy dose D_{ia} (eV/atom) [63]:

$$D_{ia} = E_i \times \frac{R_i}{R_a}. \quad (2)$$

It was shown [63] that for low-energy applications (E_i < 100 eV), the practical ion-assist dose increases exponentially with the melting temperature of the material being deposited (Figure 6 (b)). For PbO with T_{melt} ~890 °C, D_{ia} should be ~1–10 eV/atom. A lower ion arrival rate would result in a smaller density and incomplete amorphization of the film. On the other hand, excessive ion bombardment may cause an ion implantation or etching of the deposition substrate [63,66].

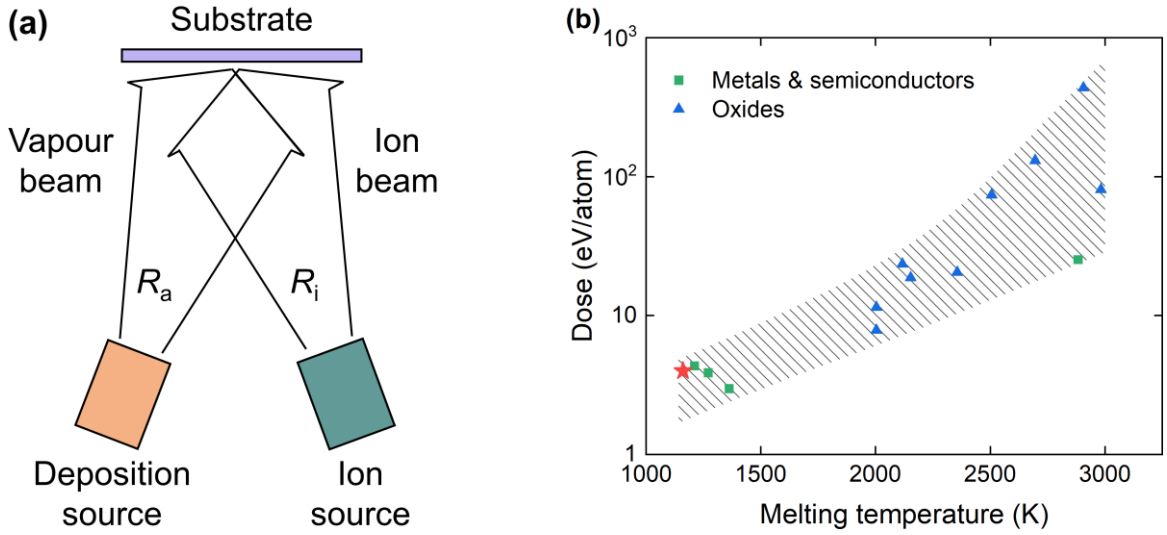

Figure 6. (a) Schematics of the ion-assisted deposition. (b) Optimal ion-assist energy dose for low-energy applications. Data extracted from [63]. The red star marker indicates a typical dose for a-PbO, which falls into the optimal region.

The ion-assisted deposition has been proven to be an effective tool for solving a variety of problems in materials science. Initially, this method was used to improve the basic properties of metal oxides, including packing density [67–70] and stoichiometry [71,72]. Nowadays, ion-assisted deposition is successfully applied to advance the growth of organic transistors and

polymer-based electronic devices [73–75]. In addition, ion-assisted deposition is used as an alternative to high pressure and/or high-temperature deposition technique of crystalline and epitaxial materials [76,77]. In the case of PbO growth, ion-assisted deposition was shown to destroy structural disorder in the form of individual platelets and to produce amorphous layers that are free of voids, possess bulk packing density, and have perfect stoichiometry throughout the film thickness. For the ion-assisted deposition of a-PbO layers, the ion energy varied between 40–60 eV, while the ion flux is kept at ~0.2 mA/cm^2. The substrate and evaporation source temperatures were similar to those of the conventional thermal evaporation, resulting in the deposition rate of a-PbO ~0.2–0.4 μm/min. Under these deposition conditions, the ion-assist dose is 2–6 eV/atom, which lays within the useful range for PbO, as indicated by the red star marker in Figure 6 (b).

Figure 7 shows the SEM image of the amorphous Lead Oxide deposited using ion-assisted deposition in an atmosphere of ionized oxygen [53]. In contrast to the poly-PbO layer (Figure 3), a-PbO has a uniform, homogeneous and void-free structure. The absence of platelets results in a smooth surface of the grown layer, never achieved before with conventional thermal deposition of the polycrystalline layers.

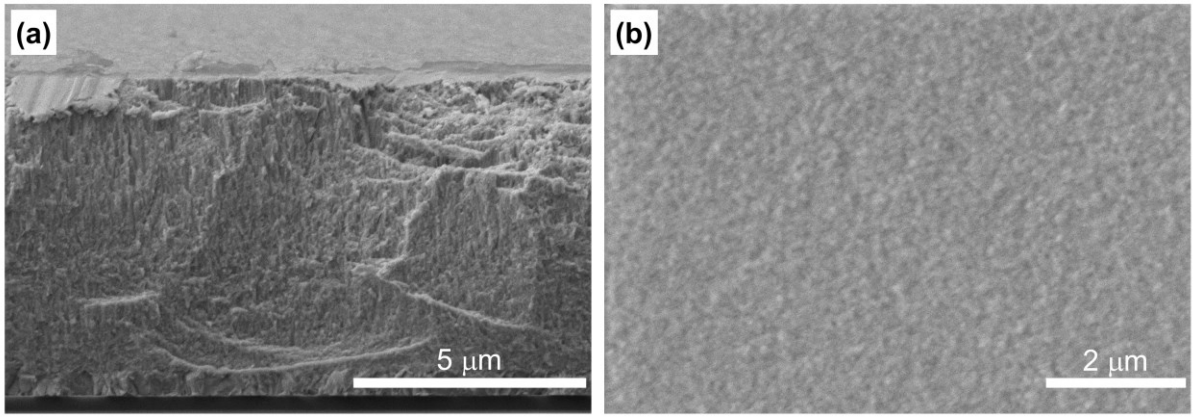

Figure 7. (a) The SEM cross-sectional view of the a-PbO. (b) The surface of the a-PbO layer [53]. (Used with permission.)

Utilization of an ion source was a natural way of solving the oxygen deficiency problem in poly-PbO layers. As it is evident from the XPS spectra obtained at different depths below the surface, a-PbO layers are structurally uniform and stoichiometric across the layer thickness: only PbO

without any other elements or oxides of lead (e.g., Pb or PbO_2) was detected (Figure 8) [53]. The reason for this is that the charge neutrality is distorted, thus facilitating the incorporation of oxygen in the growing film: the ion source ionizes oxygen, converting it to a charged state and thus making it more reactive.

Another issue which is addressed by the application of ion-assisted deposition, is the chemical stability of the grown layers. Indeed, poly-PbO is unstable in the ambient conditions; it reacts with water and carbon dioxide (CO_2) from the air and forms a compound known as a hydro-cerussite: $2PbCO_3 \cdot Pb(OH)_2$ [36,44]. This structural transformation results in significant degradation of the electrical, optical and X-ray performance of the poly-PbO photoconductor. To overcome this problem, extra technological steps should be taken, that includes either keeping a detector in the atmosphere of dry nitrogen or other inert gas, or adding a protective overcoating layer such as Parylene, Cellulose Acetate or Epoxy resin atop of the photoconductor to seal the layer and to prevent degradation of its performance during operation. In contrast, novel a-PbO layers deposited by the ion-assisted thermal evaporation technique are stable at ambient conditions, reducing the complexity and cost of the PbO-based detector fabrication process.

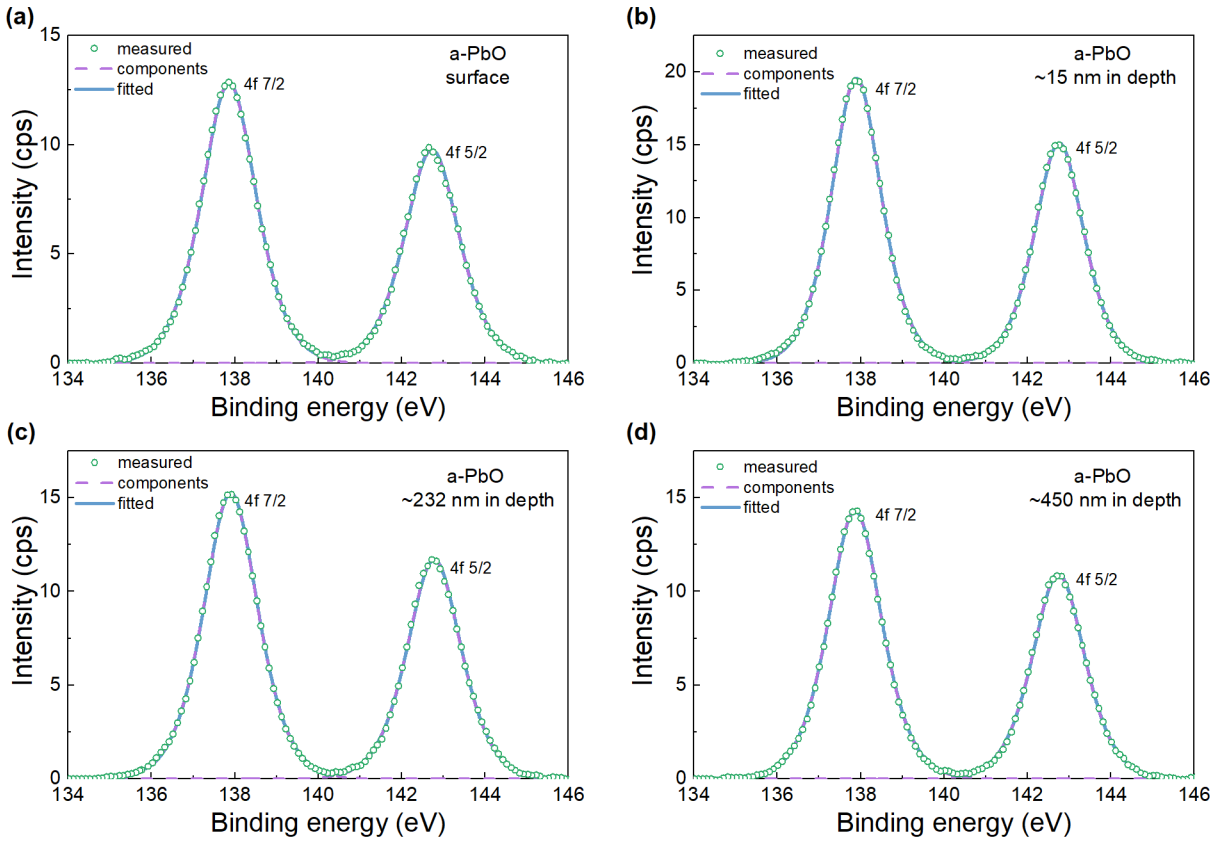

Figure 8. XPS spectra of a-PbO at a surface and at selected depths [53]. (Used with permission.)

Figure 9 (a) compares Raman spectra of poly-PbO and a-PbO films, grown with conventional thermal deposition and ion-assisted thermal deposition, respectively [53]. The Raman spectrum of poly-PbO indicates the presence of both phases: tetragonal α-PbO peaks at 81 and 340 cm^{-1} and β-PbO peaks at 89 cm^{-1} and 289 cm^{-1}. The Raman peak at ~146 cm^{-1} cannot be definitely attributed to either phase since both of them have the strongest signal in this region: α-PbO at 145 cm^{-1} and β-PbO at 147 cm^{-1} [54]. Overall, the measured Raman spectrum of poly-PbO is represented by tall and relatively narrow peaks, indicating a crystalline structure of the deposited layers. In contrast, the Raman spectrum of a-PbO is very different. It is represented by wide peaks and a high plateau typical of an amorphous structure.

Figure 9 (b) shows Raman spectra of a-PbO sample following annealing for one hour at different temperatures [53]. Various characteristic peaks evolve from a broad spectrum of the as-grown a-PbO at different temperatures, indicating that a-PbO undergoes gradual recrystallization. Indeed, at 200 °C structural changes begin with the formation of the peaks at 85, 143 and 288 cm^{-1}; in the

temperature range from 200 °C to 300 °C these peaks grow gradually and become well defined at 300 °C. These peaks are close to those of the β-PbO phase [54]. At 400 °C, another characteristic β-PbO peak appears at 71 cm^{-1}, as well as additional peaks at 121, 224, 391 and 548 cm^{-1} attributed to Pb_3O_4 [54]. Upon annealing to 600 °C, most of the former peaks have disappeared. All peaks at 600 °C are attributed to orthorhombic β-PbO. The spectra showed in Figure 9 (b) were normalized and shifted upwards for better visualization. However, it should be noted, that the peak becomes higher and narrower as the temperature increases. At the same time, the plateau decreases with an increase in annealing temperature, indicating refinement of the crystal structure.

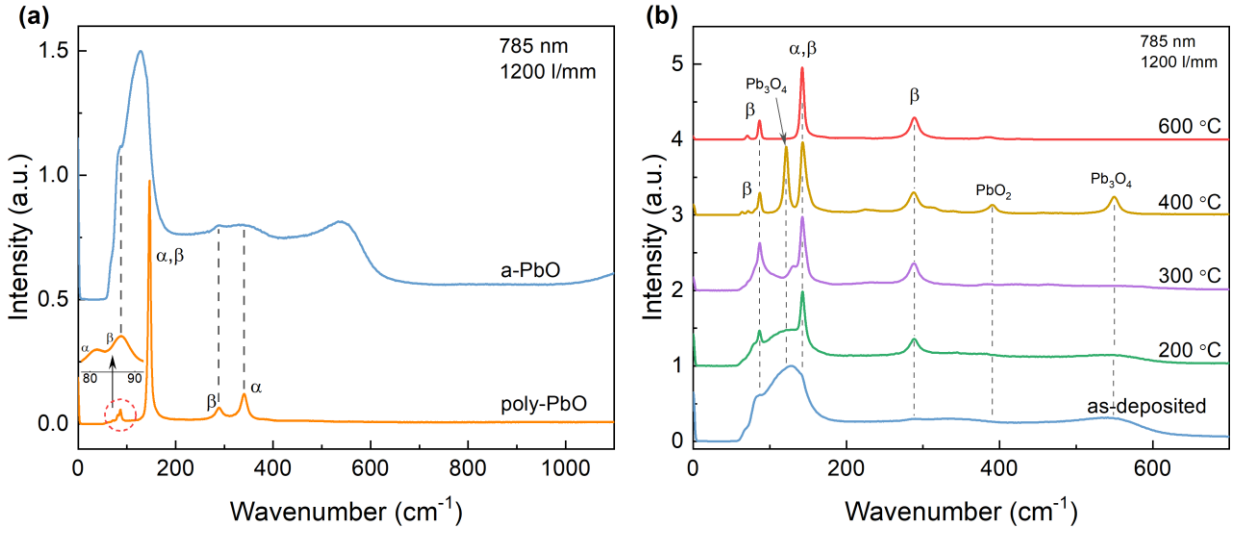

Figure 9. (a) Raman spectra of as-deposited poly-PbO and a-PbO. (b) Raman spectra of a-PbO layers after one hour annealing at selected temperatures indicated. All spectra were measured on the surface of the films [53]. (Used with permission.)

Similar peculiarities of poly-PbO and a-PbO layers were observed with X-ray diffraction (XRD) spectroscopy (Figure 10 (a)) [53]. While the XRD spectrum of poly-PbO is represented by sharp, well-defined characteristic peaks typical for crystalline structure, the XRD spectrum of a-PbO again exhibits very wide peaks indicating its amorphous nature. XRD measurements of poly-PbO reveal the presence of both tetragonal and orthorhombic phases of PbO, as well as an orthorhombic PbO_2 phase, which was not observed on the Raman spectrum. This might be due to the higher sensitivity of the XRD measurements than that of the Raman spectroscopy.

XRD also demonstrates structural changes in a-PbO upon annealing (Figure 10 (b)) [53]. The effect of annealing starts to appear at 200 °C, although insignificantly. At higher temperatures, characteristic peaks emerge from a broad spectrum. A gradual refinement of the crystal structure is further observed: the width of the emerged peaks decreases, and their intensity increases with increasing temperature. At temperatures above 300 °C, multiple phases of PbO were found to coexist simultaneously: α-, β-PbO, Pb_3O_4 and PbO_2. However, at 600 °C, the spectrum closely resembling a single phase of orthorhombic PbO with a minor peak of PbO_2 detected.

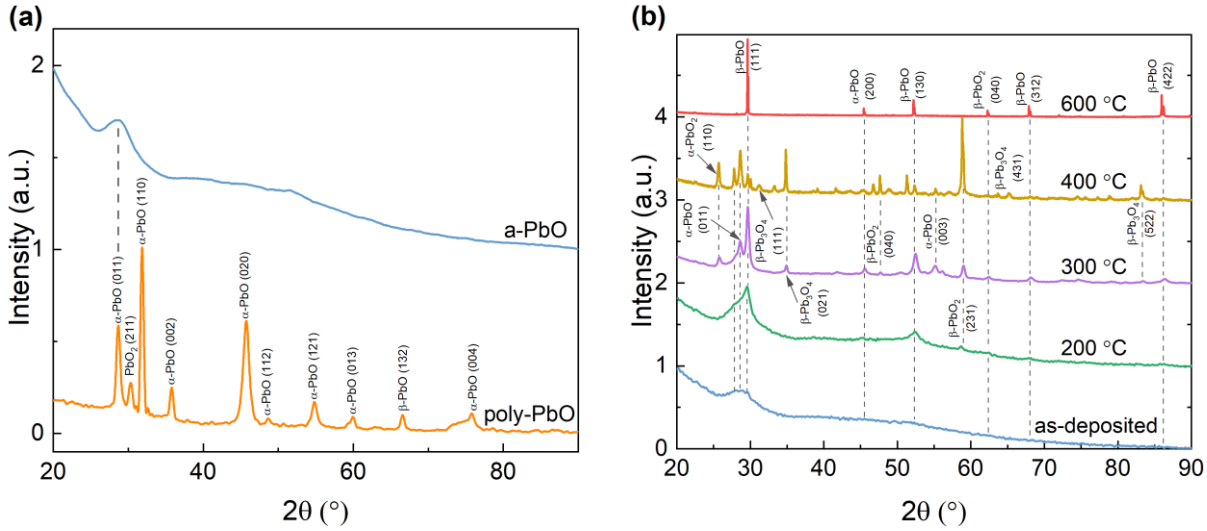

Figure 10. (a) The XRD spectra of as-deposited poly-PbO and a-PbO. (b) XRD spectra of a-PbO layers after one hour annealing at selected temperatures indicated. The spectra were measured on the surface of the films [53]. (Used with permission.)

Overall, XRD and Raman measurements after thermal annealing demonstrate that although amorphous PbO is stable at ambient conditions, it is (as expected) fundamentally metastable with respect to its crystalline counterpart and undergoes gradual recrystallization toward orthorhombic PbO at elevated temperatures. This property is reminiscent of another amorphous material that is highly significant to radiation medical imaging, namely, a-Se.

In conclusion, conventional thermal evaporation of Lead Oxide results in a platelet-like, porous polycrystalline structure of the grown layers. Introducing oxygen ion bombardment into the deposition process increases the packing density, improves stability, stoichiometry and uniformity

of the film and produces a new material, namely, amorphous Lead Oxide, which is another polymorphic form of PbO. Enhanced density and uniformity of the a-PbO layers result in a high X-ray stopping power – one of the main advantages of PbO for direct conversion X-ray detectors. The a-PbO deposition process is compatible with large-area X-ray detector technologies. Therefore, an a-PbO X-ray–to–charge transducer can be considered as an alternative to a-Se photoconductors for X-ray medical detectors in the diagnostic energy range where a-Se is suboptimal due to its low atomic number.

3. X-ray performance of poly-PbO

The first prototype of the PbO-based direct conversion medical imaging detectors was developed by Simon et al at Philips Research Laboratories [18,36]. The detector employed 340-μm thick poly-PbO X-ray–to–charge transducer deposited by conventional thermal evaporation process over a large-area (18×20 cm^2) TFT array. The results of its imaging performance evaluation were very reassuring: the sensitivity was high enough for low-dose imaging, and the spatial resolution, measured in terms of a modulation transfer function (MTF), was also very high and limited only by the pixel size – a proven capability for high-resolution imaging [18,36]. However, the detector exhibited poor temporal performance caused by signal lag. The presence of lag limits the application of this detector to static imaging only (i.e., mammography or chest radiography), while the needs of vitally-important real-time imaging, like fluoroscopy, are left unmet.

Another important characteristic of the poly-PbO photoconductor that was evaluated with the first detector prototype is the charge yield, or its reciprocal, electron-hole pair creation energy $W_{\pm}$ – an average energy needed to create one detectable EHP. $W_{\pm}$ indicates the ability of the material to convert X-ray photons into recordable electrical charges and directly indicates the detector's X-ray sensitivity: the lower the $W_{\pm}$ value, the more charges can be collected from a single photon, and thus the higher is the sensitivity of the detector. Typically, $W_{\pm}$ can be estimated from the width of bandgap of the semiconductor E_g by empirical formula, so-called Klein rule [78]. Klein showed that for many X-ray photoconductors, $W_{\pm}$ increases linearly with increasing E_g with a slope of about three. This implies that on average an energy of $3E_g$ is needed to release one EHP, which for PbO with $E_g \approx 1.9$ eV [6] yields the theoretically estimated EHP creation energy $W_{\pm}^0 \approx 6$ eV.

However, in practice, there are low-mobility amorphous and polycrystalline semiconductors which demonstrate experimental $W_{\pm}$ that is higher than that estimated by the Klein rule. This indicates that a certain portion of the initially generated charge is not collected, either due to trapping into deep localized states within the bandgap or recombination. The latter can occur between (1) separate electron and hole drifting through the bulk of the photoconductor, that collide with one another and recombine, (2) geminate EHPs, i.e, those created together by the same event of ionizing collision, or (3) non-geminate (or columnar) EHPs created by the same X-ray photon in a uniformly dense region (a column) surrounding the trajectory of a photoelectron [79]. Additionally, for two materials that stand out, a-Se and poly-PbO, the $W_{\pm}$ was found to be dependent on the electric field: $W_{\pm}$ decreases with application of a stronger electric field [18,80].

Two main techniques used for the X-ray characterization and $W_{\pm}$ evaluation are X-ray–induced Photocurrent Method (XPM) [18,48,81] and Pulse Height Spectroscopy (PHS) [80,82–84]. In XPM technique, schematically depicted in Figure 11 (a), a biased detector is irradiated by a relatively long continuous X-ray pulse, generating charge carriers in the bulk of the photoconductor. The X-ray generated EHPs are separated and extracted by the applied electric field. $W_{\pm}$ is obtained by integrating the X-ray response and comparing the total collected charge against the energy deposited by the incident X-ray flux. XPM can be used to measure $W_{\pm}$ as a function of X-ray flux, allowing to investigate how $W_{\pm}$ changes at different radiation doses, which is a very important characteristic for a medical imaging X-ray detector. However, the XPM technique has its drawbacks: if there is a charge injection in the material from the bias electrodes (as it was suggested for poly-PbO [18]), the injected charge will be added to the X-ray generated charge (since injection current cannot be easily and unambiguously separated from the X-ray response), thus the calculated $W_{\pm}$ is exaggerated, resulting in the overestimated X-ray–co–charge conversion efficiency of the detector.

On the other hand, PHS technique utilizes low fluxes of gamma photons emitted from the radioactive source to irradiate the detector; the generated charge is integrated over a very short time (in the microseconds or even nanoseconds scale) and compared with the energy of an incident photon (Figure 11 (b)). Due to very short, microsecond-range integration time, the contribution of the injection current is greatly reduced. Also, since the detector is exposed to a monoenergetic isotopic gamma-ray source rather than a polyenergetic high-flux beam from the X-ray tube, $W_{\pm}$ is

evaluated more accurately. These benefits make PHS a gold standard for more accurate measurement of $W_{\pm}$. In addition, PHS can be used not only for X-ray sensitivity measurements, but also for charge transport characterization. Indeed, the shape of the pulse height spectrum gives insights into the charge transport and collection being affected by the mobility-lifetime product $\mu\tau$ of the carriers [80]. This in turn allows evaluation of the carrier schubweg s, i.e., the mean carrier range before it is trapped or recombines. Schubweg can be expressed as the product of charge carrier's mobility μ, lifetime τ and applied field F i.e., $s = \mu\tau F$.

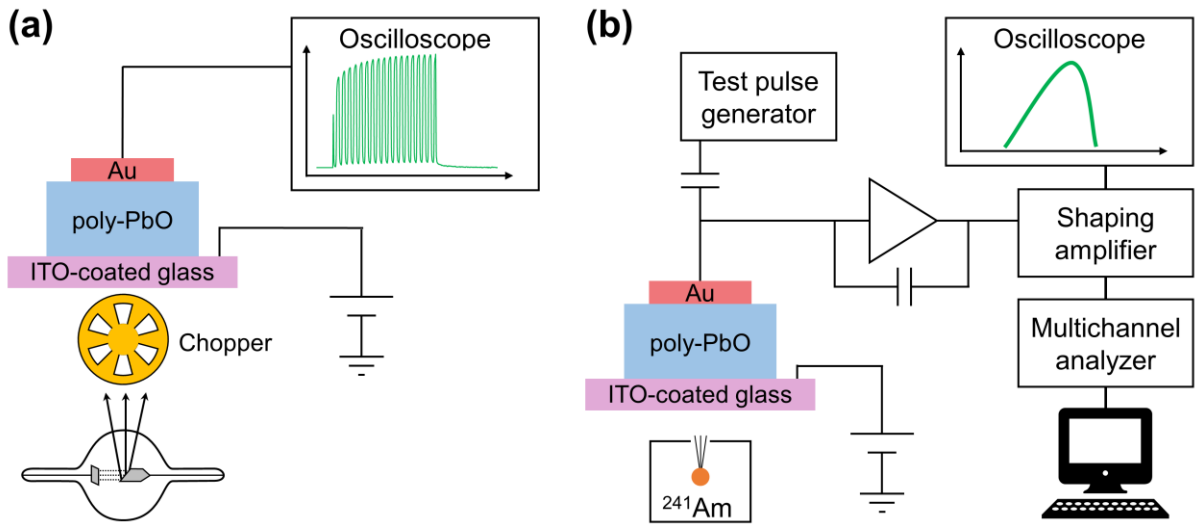

Figure 11. (a) Schematic representation of the XPM apparatus. The exposure was applied from the ITO side. The rotational chopper is used to modulate an X-ray pulse to simulate short-pulse irradiation. (b) Schematic representation of the PHS setup with a virtual ground input to charge amplifier for poly-PbO characterization. The radioactive source was located behind the ITO glass [29].

Simon et al used the XPM technique to investigate the temporal performance of the poly-PbO–based detector prototype and to evaluate $W_{\pm}$; he obtained a value of 9.9 eV/ehp at the electric field of 3.5 V/μm [18,36]. This value was higher than the one predicted by the Klein rule; however, it was much lower than the previously measured $W_{\pm}$ in a-Se at similar electric fields (45 eV/ehp at 10 V/μm) [80,85,86]. This finding was very encouraging and motivated further research and development of the PbO technology to combat signal lag while preserving charge collection

efficiency and $W_{\pm}$. Further investigation of the poly-PbO–based detector was performed by Semeniuk et al, who characterized performance of a relatively thick 42-μm poly-PbO films using both XPM and PHS techniques [29]. It should be noted that prior to this work PHS measurements have never been performed on poly-PbO mainly due to a challenge to make a PbO X-ray detector with low noise to acquire spectra with distinguishable peaks. Recent improvements in poly-PbO deposition technology led to a significant dark current suppression that in turn enables measuring an X-ray photocurrent spectrum with distinguishable peaks.

The typical response of poly-PbO detector to a continuous 3.75-s–long X-ray pulse is shown in Figure 12 (a). XPM results by Semeniuk et al [29] are very similar to the previously published data by Simon et al [18]. At the beginning of the irradiation, the amplitude of the signal gradually increases until it reaches a steady-state value in ~2 seconds. As exposure terminates, the detector exhibits a well-pronounced residual current, or lag. Both the signal amplitude and lag increase with the applied electric field F in a similar manner so that when the signals are normalized, they closely resemble each other as shown in Figure 12 (b).

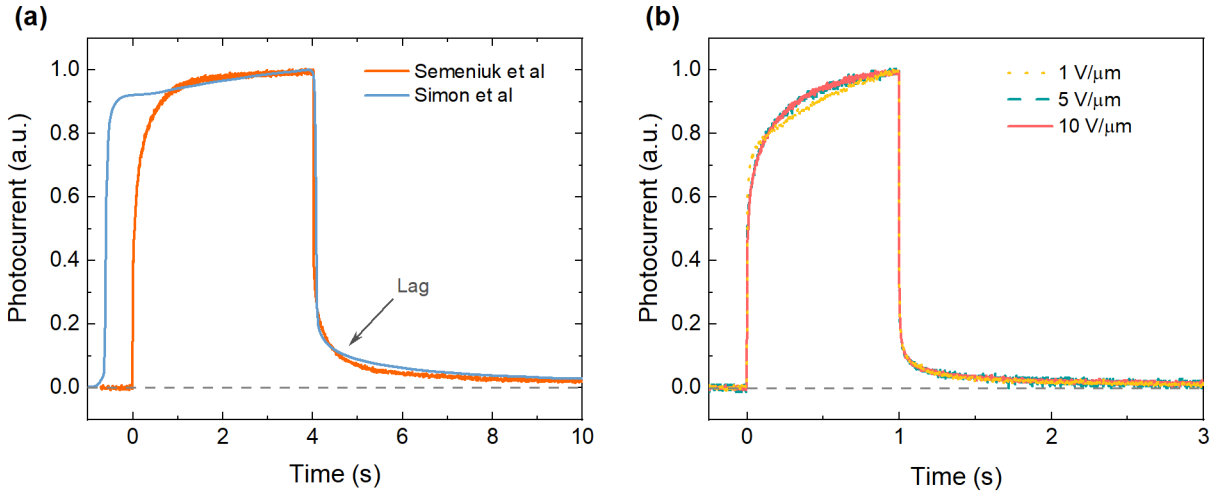

Figure 12. (a) Normalized X-ray response of poly-PbO, measured at F = 4 V/μm. (b) Normalized X-ray responses measured at different electric fields. In all the waveforms, the dark signal was set to zero [29].

The X-ray sensitivity $W_{\pm}$ for the poly-PbO detector was calculated from the XPM measurements for different pulse durations and electric fields. For the 3.75-s–long X-ray pulse and applied field

F = 4 V/μm, $W_{\pm} \approx$ 12 eV/ehp, which is close to the previously reported by Simon et al value $W_{\pm} =$ 9.9 eV/ehp, obtained under similar experimental conditions (5 s, 3.5 V/μm [18]). However, it should be noted that $W_{\pm}$ measured by XPM is sensitive to the X-ray pulse duration t_{pulse}: the shorter the X-ray pulse, the larger is $W_{\pm}$. For instance, at F = 4 V/μm and t_{pulse} = 100, 50 and 10 ms, $W_{\pm}$ will increase to 14.2, 15.8 and 18.3 eV/ehp, respectively. On the other side, at longer exposures ($t_{\text{pulse}} >$ 3.75 s) and higher electric fields ($F >$ 10 V/μm), $W_{\pm}$ will drop to its estimated value $W_{\pm}^{0}$.

To investigate this unusual dependence of $W_{\pm}$ on t_{pulse}, the detector was exposed to a series of short millisecond-long X-ray pulses, instead of a single seconds-long pulse, using a copper rotating chopper (thick enough to block X-rays) to modulate an incident X-ray pulse at a variable frequency (Figure 11 (a)) [29]. This XPM technique in a pulsed mode was often selected for investigation of the temporal behaviour of the detector since it allows to distinguish the injected current from the X-ray photogenerated current [87,88]. The example of the X-ray response is shown in Figure 13, where a 3.75-s–long X-ray pulse was modulated with the frequency of 5 Hz and 50/50 duty cycle. In this configuration, the detector is exposed to a sequence of ~18 100-ms–long X-ray pulses with an interval of 100 ms between each other.

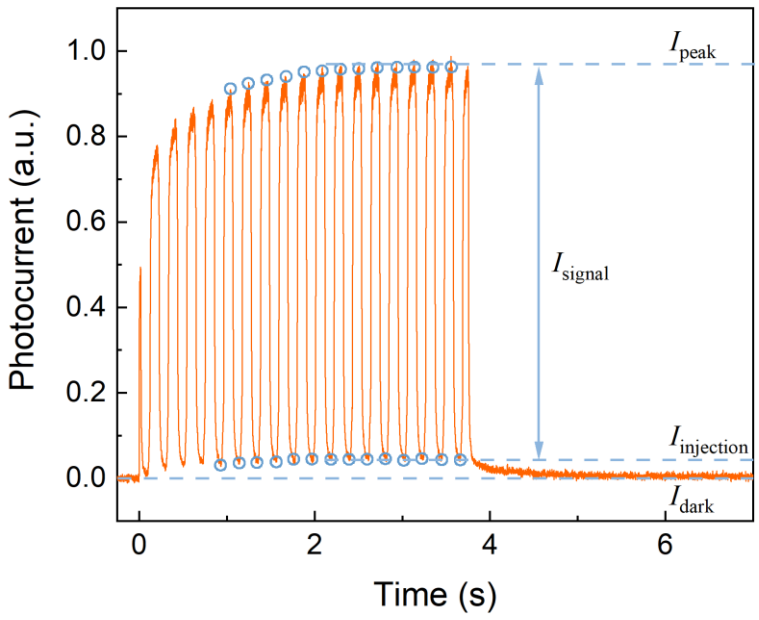

Figure 13. The X-ray response of poly-PbO detector to the modulated X-ray exposure at $F = 2$ V/μm, normalized to the steady-state peak value. It should be noted that the first frames are affected by the asynchronization of the chopper rotation and the beginning of the exposure, and fluctuations in radiation intensity at the beginning of the X-ray pulse [29].

As it can be seen from Figure 13, the X-ray response of the poly-PbO detector I_{peak} has two components: the signal due to the X-ray generation of charge carriers I_{signal} and the signal due to injection $I_{\text{injection}}$. The injection current builds up during the irradiation reaching a steady-state value after ~2 s, while the X-ray generated current remains unchanged. Moreover, the level of $I_{\text{injection}}$ changes with the chopper rotation frequency f, where $t_{\text{pulse}} = 1/2f$. In Figure 14, the ratio of steady-state currents $(I_{\text{injection}}/I_{\text{peak}}) \times 100\%$ is plotted as a function of f [29]. At the higher frequencies (smaller pulse durations), $I_{\text{injection}}$ has a larger contribution to the total current (corresponding to higher $I_{\text{injection}}/I_{\text{peak}}$ ratio on the graph, and therefore, lower $I_{\text{signal}}/I_{\text{peak}}$ ratio). At the end of the irradiation, $I_{\text{injection}}$ gradually decays over time, which appears as signal lag. As seen from Figure 13, after the exposure terminates, the signal almost instantaneously drops to the steady-state level of $I_{\text{injection}}$ reached during the irradiation, after which it is rolling off.

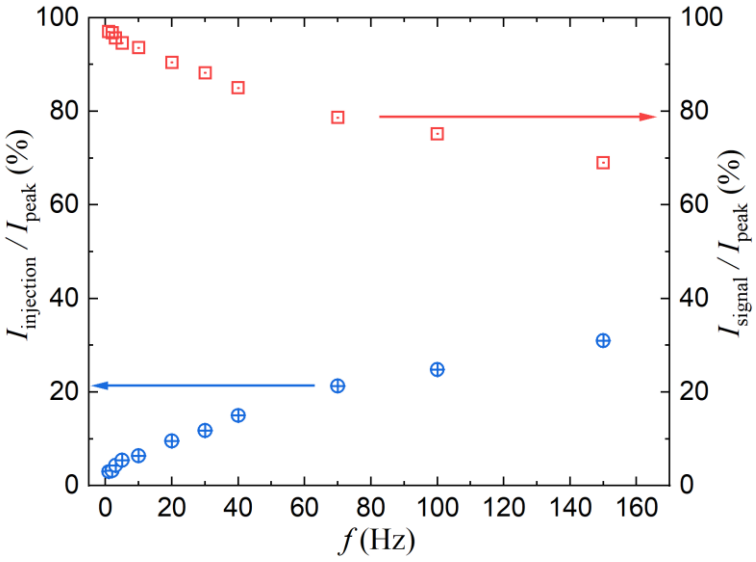

Figure 14. The ratios of $I_{injection}/I_{peak}$ and I_{signal}/I_{peak} are plotted as a function of the chopper frequency f for $F = 2$ V/μm [29].

The signal lag was calculated as a percentage of I_{peak} and plotted in Figure 15, that shows how signal lag decays with time (represented by a number of read-out frames) for different frame rates [29]. The amplitude of lag is proportional to the X-ray pulse duration t_{pulse}: for a 1-s X-ray exposure, the lag decays to a level below 1% after a few seconds, while for 10-ms pulse it takes less than 50 ms. Also, lag is more severe at shorter exposures. This agrees with the previous observation of higher $I_{\text{injection}}/I_{\text{peak}}$ ratio for higher chopper frequency (i.e., shorter X-ray pulses) shown in Figure 14.

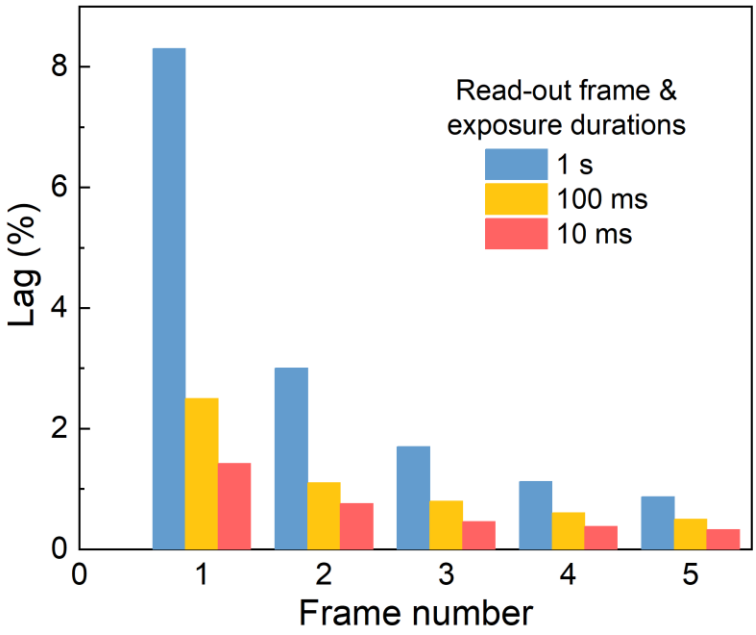

Figure 15. The signal lag (presented as a ratio of I_{peak} in percent) is shown as the function of a frame number. The frame read-out time is the same as exposure duration [29].

Despite that the total X-ray generated charge measured by the XPM technique is being overestimated due to the presence of the injection current, leading to inaccurate X-ray sensitivity $W_{\pm}$, this method is very useful to investigate the behaviour of signal lag, particularly in poly-PbO. It was previously believed that in disordered materials, lag is linked to the release of the previously trapped carriers from the deep trapping sites in the energy band tails [89]. If the exposure duration t_{pulse} is shorter than the de-trapping time from these sites, then some carriers get released after the X-ray exposure is ceased, contributing to signal lag. In this case, the release time and the signal

lag should not depend on t_{pulse}, since it is a fundamental property of material and not an experimental parameter. Moreover, signal lag should decrease with the application of a stronger electric field, since charge schubweg ($s = \mu\tau F$) increases with the field, making charge de-trapping more efficient. However, Figure 12 (b) demonstrates that the lag is scalable with the electric field, while Figures 14 and 15 show that lag is proportional to exposure duration t_{pulse}. Therefore, signal lag in poly-PbO cannot be related to the charge trapping and detrapping during their drift across the bulk of the photoconductor. In addition, the previous investigation of lag dependence on the material of the bias electrode [18] suggests that the bulk charge trapping is not the dominant mechanism for the signal lag in poly-PbO.

An acceptable explanation of this peculiar behaviour is based on the time-dependent X-ray–induced local enhancement of the electric field at the interface between the metal electrode and the photoconductor, triggering injection from the bias electrode into the poly-PbO. During the XPM measurements, a high flux of X-rays is used to generate a measurable signal, thus creating a relatively large amount of charge carriers across the photoconductor. When the carriers get trapped, they modify the electric field inside of the photoconductor. Those carriers that are trapped at the metal/photoconductor interface (the surface of the photoconductor has an abundant concentration of trapping sites) might cause a local enhancement of the electric field. This, in turn, triggers charge injection, which builds up during the exposure, and introduces uncertainty in measured $W_{\pm}$ values [87,88]. The injection current builds up until an equilibrium state between the trapped and released carriers at the interface is achieved. As the X-ray exposure terminates, the local electric field gradually returns to its initial level (i.e., applied field) and the residual injection current decreases as well.

The kinetics of the injection current build-up during exposure was further examined with pulsed X-rays [29]. Figure 16 shows the response of the poly-PbO detector to two consecutive 100-ms pulses, plotted in a semi-log scale. The signal is composed of two components: fast C-A and slow A-B. The fast C-A component is associated with the transit of the X-ray generated carriers through the detector, while the slow A-B component represents the contribution of the injection current [87,88]. The X-ray pulse duration and the interval between pulses decreases as the chopper frequency increases. As a result, point B shifts toward the A region, thus resulting in larger injection current levels (see Figures 14 and 15). It would be very tempting to use only the C-A

portion of the signal for the $W_{\pm}$ calculations; however, the position of point A will vary with experimental conditions such as X-ray pulse duration and exposure. Indeed, as shown in Figure 15, lag depends on X-ray pulse duration. Since the value of the signal from the C-A section is inversely correlated to lag, the C-A portion also depends on experimental conditions. This suggests that for materials with dynamic types of injection caused by local enhancement of the electric field, XPM measurements inherently overestimate $W_{\pm}$ values. Therefore $W_{\pm}$ measurements were verified with an alternative technique insensitive to injection, such as PHS.

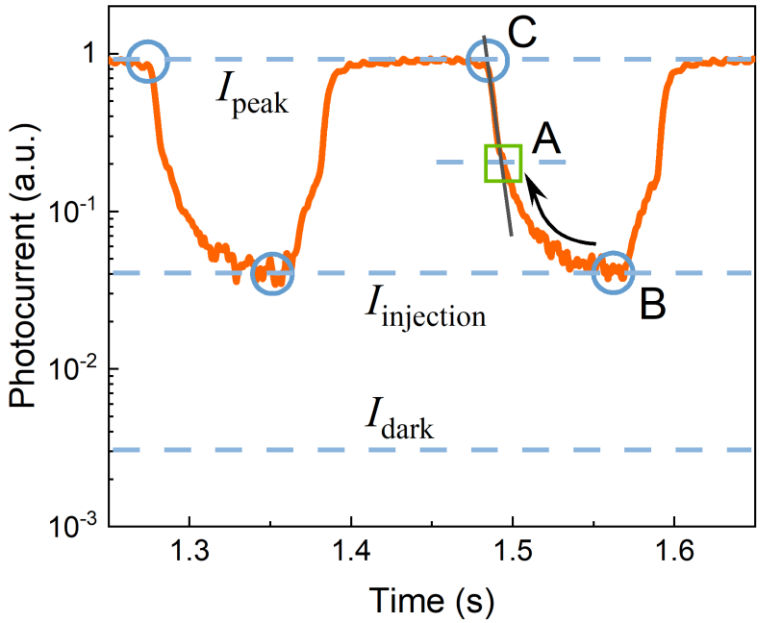

Figure 16. The response of poly-PbO detector to subsequent 100-ms X-ray pulses at $F = 2$ V/μm plotted in the semi-log scale (taken from the middle section of the graph shown in Figure 13). Points C and B represent the total current and the injection current levels, respectively, while point A defines the inflection point in the signal decay, i.e., the beginning of lag [29].

A typical pulse height spectrum of poly-PbO obtained with 59.5 keV gamma photons from the ^{241}Am source is shown in Figure 17 [29]. The spectrum is asymmetrical and obscured by the background noise (injection current and noise from electronics) at lower channel numbers. From the measured spectrum, the $\mu\tau$ product of the charge carriers and the value of $W_{\pm}$ which corresponds to the position of the spectral peak could be determined [90]. However, due to the asymmetrical shape of the spectrum, a numerical simulation must be applied to accurately

determine the peak position [90–95]. For the given experimental conditions, nearly uniform charge generation in the photoconductor is expected since at the photon energy 59.5 keV, the attenuation depth of PbO is $\delta \approx 300$ μm, which is much larger than the detector thickness (d = 42 μm) [6]. Therefore, the PbO layer was divided into virtual slices and assuming uniform generation, the collection efficiency from every slice was calculated using the depth-dependent Hecht formula. This formula describes the collection efficiency $\eta(x)$ (i.e., the ratio of collected charge carriers N_{col} to the total number of carriers generated by the X-ray photons N_{gen}) as follows [90–95]:

$$\eta(x) = \frac{N_{\mathrm{col}}(x)}{N_{\mathrm{gen}}} = \frac{s_{\mathrm{h}}}{d}\left(1 - e^{-\frac{d-x}{s_h}}\right) + \frac{s_e}{d}\left(1 - e^{-\frac{x}{s_e}}\right), \quad (3)$$

where x is the distance from the radiation receiving electrode (ITO in this case) to the charge generation site, $s_{\mathrm{h,e}}$ is the hole and electron schubweg, respectively. Afterwards, the Hecht fit was convolved with noise spectrum and the result was used to fit the measured spectrum. After a fit was received, the true peak position was determined from the unconvolved Hecht fit (see Figure 17). The Hecht fit shows how the true peak position S is affected by the system noise, which is typical for materials with significant differences in the carrier's schubwegs [90–95]. From the true peak position S, the EHP creation energy $W_{\pm}$ can be derived as:

$$W_{\pm} = \varepsilon / S, \quad (4)$$

where ε = 59.5 keV is the energy of the emitted from ^{241}Am source photon.

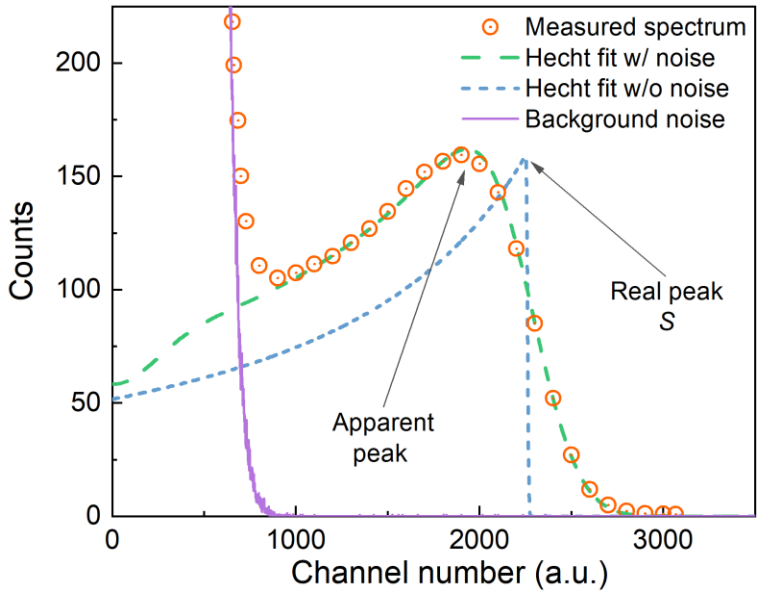

Figure 17. Pulse height spectrum measured with 42-μm poly-PbO detector at F = 10 V/μm, ε = 59.5 keV, shaping time τ_s = 50 μs and superimposed with noisy and noiseless Hecht fits. Background counts are shown to dominate the spectral waveform below channel ~800. The measured position of the noise-free spectral peak is shown to be affected by the system noise [29].

Following this procedure, the Hecht fitting provided the values of the mobility-lifetime products for holes and electrons: $\mu_h\tau_h = 4.1 \times 10^{-8}$ cm^2/V, $\mu_e\tau_e \approx 10^{-9}$ cm^2/V. $\mu\tau$ values are assigned to a type of carrier based on the previous reports that revealed that holes are the faster carrier in poly-PbO [55,96]. The field dependence of $W_{\pm}$ for different shaping times τ_s, derived from PHS measurements, is shown in Figure 18 [29]. $W_{\pm}$ decreases with both F and τ_s, and reaches the value ~17 eV/ehp at F = 10 V/μm and τ_s = 17 μs. The dashed line shows a predicted by Klein rule value of $W_{\pm}^0 \approx 6$ eV/ehp.

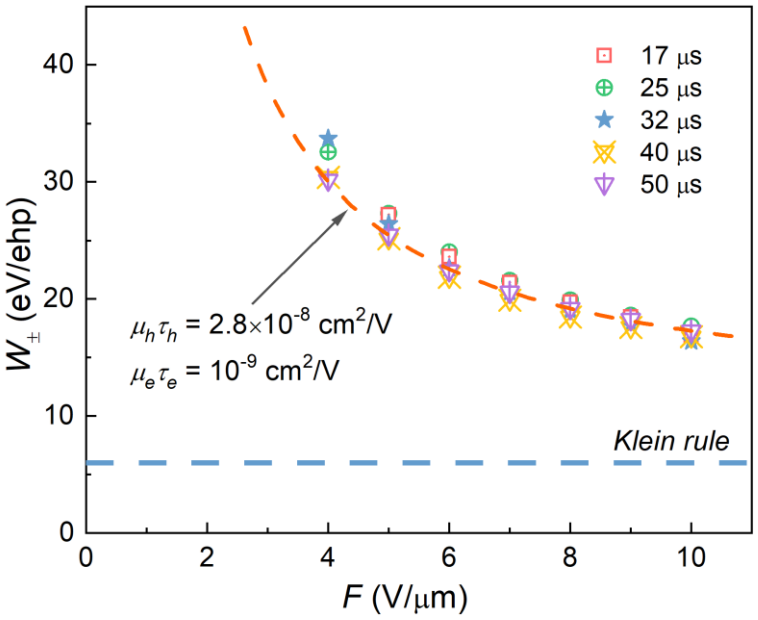

Figure 18. Measured from PHS values of $W_{\pm}$ are plotted as a function of F for different τ_s [29].

The field dependence of $W_{\pm}$ was used to verify $\mu\tau$ values obtained from PHS measurements, following the procedure in [97], where X-ray sensitivity is given by:

$$\frac{N_{\mathrm{col}}}{N_{\mathrm{inc}}} = x_{\mathrm{h}}\left[\left(1-e^{-\frac{1}{\Delta}}\right)+\frac{1}{\frac{\Delta}{x_{\mathrm{h}}}-1}\left(e^{-\frac{1}{x_{\mathrm{h}}}}-e^{-\frac{1}{\Delta}}\right)\right]+x_{\mathrm{e}}\left[\left(1-e^{-\frac{1}{\Delta}}\right)-\frac{1}{\frac{\Delta}{x_{\mathrm{e}}}+1}\left(1-e^{-\frac{1}{x_{\mathrm{e}}}-\frac{1}{\Delta}}\right)\right], \tag{5}$$

where $x_{\mathrm{h}}, x_{\mathrm{e}}$ are normalized hole and electron schubweg, respectively $\left(x_{\mathrm{e,h}} = s_{\mathrm{e,h}}/d\right)$, Δ is a normalized attenuation depth $\Delta = \delta/d$ and N_{inc} is the number of incident X-ray photons. Considering uniform absorption, equation (5) can be simplified to:

$$\frac{N_{\mathrm{col}}}{N_{\mathrm{inc}}} = \frac{1}{\Delta}\left[x_{\mathrm{h}}\left(1+x_{\mathrm{h}}\left(e^{-\frac{1}{x_{\mathrm{h}}}}-1\right)\right)+x_{\mathrm{e}}\left(1+x_{\mathrm{e}}\left(e^{-\frac{1}{x_{\mathrm{e}}}}-1\right)\right)\right], \tag{6}$$

assuming that for large Δ (i.e., uniform absorption): $\left(1-e^{-\frac{1}{\Delta}}\right)\rightarrow\frac{1}{\Delta}$; $\frac{1}{\frac{\Delta}{x_{\mathrm{e,h}}}\pm1}\rightarrow\frac{x_{\mathrm{e,h}}}{\Delta}$; $e^{-\frac{1}{\Delta}}\rightarrow 1$. It should be noted that equations (5) and (6) provide a generic expression of photoconductor sensitivity. They account for both *X-ray absorption efficiency* and *charge collection efficiency*. To derive the *charge collection efficiency* alone from the PHS measurements, equation (6) should be divided by absorption efficiency $\left(1-e^{-\frac{1}{\Delta}}\right)$, which for large Δ reaches $\frac{1}{\Delta}$. Therefore, the expression for charge collection efficiency for the case of uniform absorption takes the form:

$$\eta = \frac{N_{\mathrm{col}}}{N_{\mathrm{gen}}} = x_{\mathrm{h}}\left(1 + x_{\mathrm{h}}\left(e^{-\frac{1}{x_{\mathrm{h}}}} - 1\right)\right) + x_{\mathrm{e}}\left(1 + x_{\mathrm{e}}\left(e^{-\frac{1}{x_{\mathrm{e}}}} - 1\right)\right), \quad (7)$$

where $N_{\mathrm{gen}} = N_{\mathrm{inc}}/\Delta$. Interestingly, the same expression (7) can be obtained by integrating equation (3) over x and normalizing by thickness d. Fitting field dependence of $W_{\pm}$ (shown in Figure 18) with equation (7) provided $\mu\tau$ values for holes and electrons that are similar to values obtained from spectrum fitting: $\mu_{\mathrm{h}}\tau_{\mathrm{h}} = 2.8 \times 10^{-8}$ cm^2/V, $\mu_{\mathrm{e}}\tau_{\mathrm{e}} \approx 10^{-9}$ cm^2/V.

The asymmetrical shape of the spectrum observed by the PHS measurements that is shown in Figure 17 is typical for materials with a substantial difference between the schubwegs of electrons and holes and for the case of the ballistic deficit resulting from insufficient shaping time [80,90,91,95]. Moreover, the non-Gaussian shape of the spectrum remains even under higher applied electric fields and longer shaping times, suggesting that at the fields used here, the transit time of the slower carriers (i.e., electrons) is much longer than the shaping times. Similar behaviour was observed in other materials, like CdTe and CdZnTe, which are currently employed in gamma-detectors [90,91,98]. Because holes are much slower than electrons in these materials, they possess a relatively long transit time which results in a ballistic deficit and asymmetrical PHS spectrum.

From the mobility-lifetime products of $\mu_{\mathrm{h}}\tau_{\mathrm{h}} \approx 4.1 \times 10^{-8}$ cm^2/V (for faster carriers, holes) and $\mu_{\mathrm{e}}\tau_{\mathrm{e}} \approx 10^{-9}$ cm^2/V (for the slow carrier, electrons) obtained from the PHS spectra fitting, one can calculate the carrier schubwegs. At F = 10 V/μm, the hole schubweg $s_{\mathrm{h}} = 41$ μm, which is almost identical to the poly-PbO thickness of $d = 42$ μm. It is not surprising that at this particular field, when $d \approx s_{\mathrm{h}}$, the charge collection efficiency is no longer dependent on the shaping time. As it is seen in Figure 18, at F = 10 V/μm, all data points overlap since most of X-ray generated holes are collected regardless of the shaping time used in the experiment. Since for electrons $\mu_{\mathrm{e}}\tau_{\mathrm{e}} \approx 10^{-9}$ cm^2/V is much lower than for holes, they do not contribute significantly to the signal on the microseconds scale.

From the mobility-lifetime products measured with PHS and the carriers mobility measured, for example, with a conventional Time-of-Flight (TOF) or an advanced photogenerated Charge Extraction by Linearly Increasing Voltage (photo-CELIV) techniques, one can estimate the lifetime of the carriers. For this purpose, the hole mobility μ_{h} was separately measured in this sample using a photo-CELIV technique, similarly to how it was previously done in [55], which reached a value of $\mu_{\mathrm{h}} \approx 0.008$ cm^2/Vs at relatively low electric field of 1 V/μm (measurements at

higher electric field were technically unfeasible due to the limitations of the photo-CELIV experimental setup). Although hole mobility in poly-PbO increases with the electric field, this dependence was omitted for the sake of rough estimate, which gives a lifetime of drifting holes at low electric field $\tau_{\mathrm{h}} = \mu_{\mathrm{h}}\tau_{\mathrm{h}}/\mu_{\mathrm{h}} \approx 5.1$ μs.

Electron lifetime can be estimated in a similar way. However, due to the low mobility of electrons in poly-PbO and the limited capability of the photo-CELIV apparatus to characterize transport in such a thick layer, a previously measured value of $\mu_{\mathrm{e}} \approx 2 \times 10^{-5}$ cm^2/Vs at F = 10 V/μm in a 5-μm thick poly-PbO layer was used [96] and extrapolated to the 42-μm thick layer used for the PHS measurements, since mobility in materials with dispersive charge transport is scalable with their thickness [99,100]. Because the hole mobility of the 42-μm-thick sample is about an order of magnitude smaller than that of the 5-μm-thick sample [55], the same ratio can be applied to electrons. Therefore, for 42-μm-thick sample, the electron mobility is estimated as $\mu_{\mathrm{e}} \approx 2 \times 10^{-6}$ cm^2/Vs, which gives the electron lifetime of $\tau_{\mathrm{e}} \approx 0.5$ ms, and the electron transit time of ~21 ms at maximal F = 10 V/μm. These calculations support an initial hypothesis that electrons are responsible for the ballistic deficit in the PHS measurements. In order to collect slower electrons, the shaping time should be on the order of milliseconds (3 orders of magnitude higher than currently used), which would inevitably lead to a significant noise increase [101] that would obscure the useful signal.

Overall, more accurate measurements of the X-ray sensitivity in poly-PbO with PHS technique demonstrated that despite the values of $W_{\pm}$ are higher than the predicted $W_{\pm}^{0}$ even at the relatively strong electric fields, $W_{\pm}$ still compare very favourably with that in a-Se (17 eV/ehp and 45 eV/ehp at 10 V/μm for poly-PbO and a-Se, respectively). The combination of a higher quantum efficiency over a wider energy range, together with higher charge yield, makes poly-PbO a very promising candidate to replace a-Se photoconductors in the next generation of direct conversion digital X-ray medical imaging detectors. An investigation of the signal lag kinetics with the pulsed XPM technique in the poly-PbO detector revealed that its temporal performance is limited by the configuration of the detector, rather than by the fundamental charge transport properties of poly-PbO. This finding suggests an alternative approach to improving the PbO technology: to separate a poly-PbO photoconductor from the bias electrode by a blocking layer that would prevent charge injection while allowing collection of the photogenerated charge, similar to how it was previously

done for a-Se [86,87]. The development of such a multilayer blocking structure would substantially improve the performance of the poly-PbO–based detector by reducing signal lag and dark current, which would permit its use in real-time imaging. The development and characterization of the multilayer structures based on the Lead Oxide photoconductor is described in the next sections.

4. X-ray performance of a-PbO

A technological step that replaces the structural disorder in poly-PbO with a homogeneous a-PbO structure, by introducing ion bombardment into the deposition process as described in Section 2, significantly reduces signal lag, and improves the temporal performance of the a-PbO–based X-ray detector. This was demonstrated with a-PbO single-pixel detector prototype that consists of 8-μm thick a-PbO layer deposited on an ITO-coated glass substrate, and a gold contact, 1 mm in diameter, that was sputtered *ex-situ* atop the a-PbO film [30].

A typical response of a-PbO to a 4-s X-ray pulse is shown in Figure 19 (a). The X-ray response exhibits constant signal amplitude during the exposure, which rapidly drops to the dark current level after exposure terminates, with almost no signal lag. The a-PbO photoconductor demonstrates a remarkable improvement of the temporal performance in comparison to poly-PbO, also illustrated in Figure 19 (a). Indeed, the photocurrent in the poly-PbO detector builds up during the exposure, followed by relatively long lag. Figure 19 (b) illustrates the normalized X-ray response of the a-PbO detector to 100-ms exposures measured at different electric fields. Signal lag in a-PbO is scalable with the applied electric field, showing no lag improvement at higher fields.

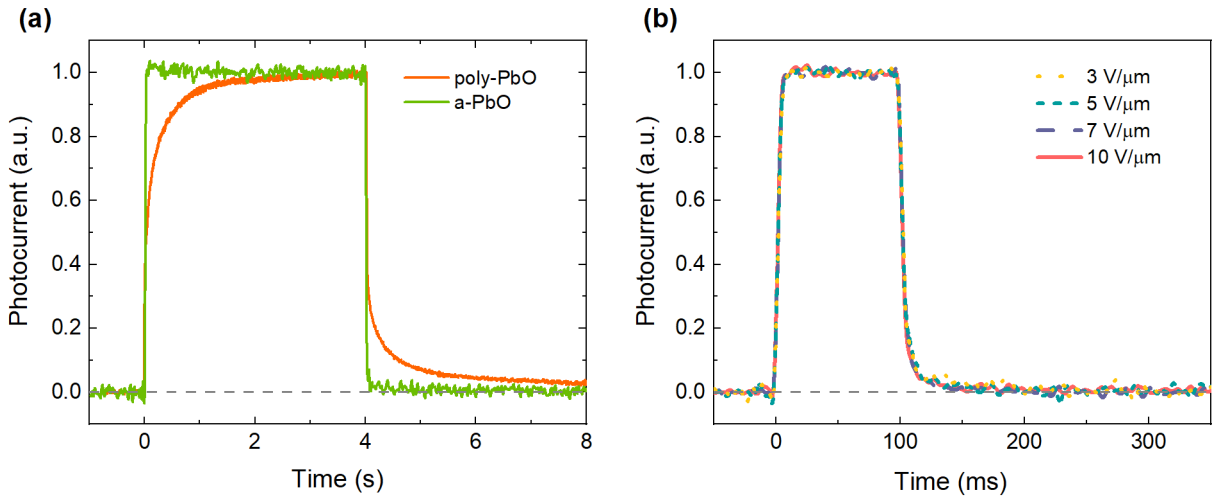

Figure 19. (a) The normalized X-ray response of a-PbO at F = 10 V/μm to 4-s X-ray exposure and that of poly-PbO. (b) The normalized response of a-PbO to 100-ms X-ray pulse at different applied electric fields. The X-ray signals were offset corrected for the dark current [30].

The X-ray sensitivity of a-PbO was characterized in terms of the EHP creation energy $W_{\pm}$ using XPM technique [30]. Figure 20 shows the measured $W_{\pm}$ at different electric fields F up to 20 V/μm: $W_{\pm}$ decreases with F and reaches the value of 22 eV/ehp and 18 eV/ehp at 10 V/μm and 20 V/μm, respectively. It should be noted that the measurements performed using short (100 ms) and long (1 s) X-ray pulses provided essentially the same values within ~3% error, which is in stark contrast to poly-PbO. The inset to Figure 20 shows $W_{\pm}$ plotted versus reciprocal electric field $1/F$ and a linear fit extrapolation that reaches ~14 eV/ehp at "infinite" electric field, which is nearly two times larger than the theoretically predicted $W_{\pm}^{0}$ by Klein rule for PbO.

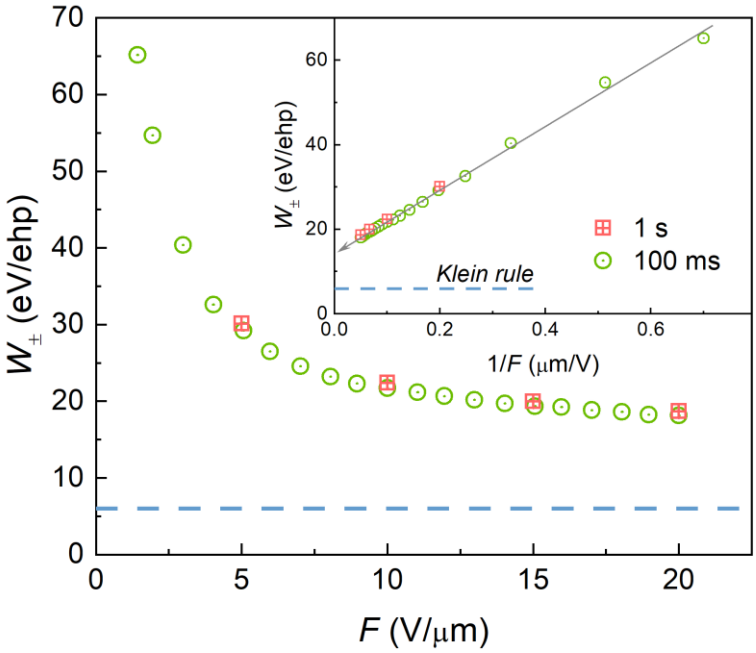

Figure 20. Measured values of $W_{\pm}$ are plotted as a function of F for 100-ms and 1-s exposures. The inset to the Figure shows $W_{\pm}$ plotted as a function of $1/F$ [30].

To make a deeper insight into the temporal performance of the a-PbO detector, signal lag was measured at various experimental conditions, relevant to those used in fluoroscopy, using the pulsed XPM technique [24,25] and plotted in Figure 21 [30]. For this purpose, the detector was exposed to a short (4 ms and 10 ms) X-ray pulse and an X-ray response was readout every 33 ms i.e., at 30 frames per second (fps) read-out rate. The lag was determined as the ratio of the residual current after exposure to the X-ray signal value. For example, following the convention described in [24,25], the residual signal after the first frame, i.e., in 33 ms after termination of exposure, was found to be ~1.4% for 10-ms X-ray pulse. The signal lag during consequent frames was measured with 33-ms intervals showing the lag values <1% of the signal magnitude during the exposure. As seen from Figure 21, the signal lag of a-PbO increases with exposure duration, which was previously observed in other materials, like a-Se and poly-PbO [24,29]. Thus, the first frame lag of a-PbO was found to be 0.4% and 1.4% after single X-ray pulses of 4 ms and 10 ms, respectively. The lag dropped to undetectable values after the first frame for the shortest pulse duration (4 ms) and after the second frame for 10 ms pulse. While the data obtained compares favorably with lag measured in a-Se detectors of 1.5% and 3.7% for same pulse durations [21,25,26], it is also important to check the residual signal under longer exposures. To simulate such conditions, the a-

PbO detector was subjected to extended exposures of 100 ms, 1 s and 4 s. The corresponding values for the first frame lag are: 3.2%, 4.1% and 4.7%, respectively. The obtained values are also comparable with those measured on a-Se direct conversion and CsI indirect conversion detectors, which normally exhibit first frame lag values less than 10% and 5%, respectively [2,24,27,102,103]. It should be noted that lag in these detectors was measured in the pulsed fluoroscopy mode, i.e., with sequence of short exposures 1–8 ms every 33 ms so that detector material has time to "rest" and recover between exposures. Nevertheless, as this is seen from Figure 21, with the subsequent frames the lag quickly drops even for long exposures; it is no longer detected after the fourth frame for 100-ms pulse duration and after the eighth frame for 1-s pulse. For the longest pulse of 4 s, the lag is still at ~2% after eight frames, although this long pulse of X-rays represents extreme operation conditions with extra load on the detector.

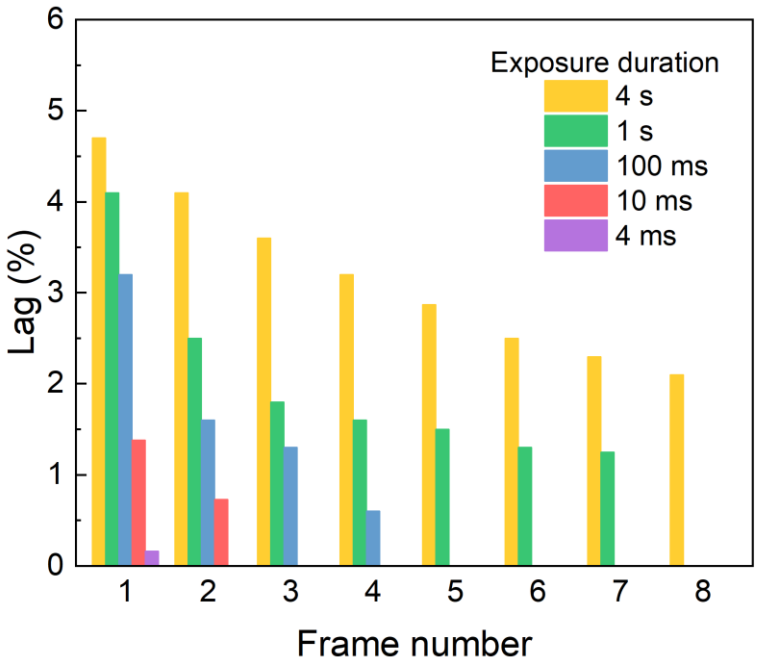

Figure 21. The signal lag in a-PbO was measured at a 30-fps read-out rate and 10 V/μm for different exposure durations [30].

Temporal performance is one of the most important characteristics of the photoconductor while considering its application in real-time fluoroscopic imaging. During fluoroscopy-guided operations, which is one the most challenging and demanding radiation medical procedures, the

detector is exposed to very short (1–10 ms) X-ray pulses, while the read-out rate is very fast, up to 30 fps [5,25,27]. Such a fast image acquisition rate is necessary to capture the motion of human biological functions (for example, a heart beating) without a blur, thus requiring a detector capable of low lag operation. Otherwise, the residual signal from the previous frame would roll over to the subsequent frame, causing signal build-up and misrepresentation of the image. Therefore, a quasi-rectangular shape of the X-ray response of the detector, and the absence of lag are important Figures of merit to evaluate the readiness of a photoconductor for direct conversion X-ray medical imaging detectors. a-PbO demonstrates significant signal lag suppression in comparison with its polycrystalline counterpart (see Figures 19 and 21). For a pulse duration of 4 ms, most relevant to fluoroscopic procedures, the lag after the first frame was as small as 0.4%, and even for the extended exposures, the observed lag was below 5%, thus making the temporal performance of a-PbO comparable with CsI-based detectors, which are currently used in commercial fluoroscopic systems.

Lag in a-PbO depends on the exposure duration, but it is scalable with the applied electric field (see Figures 19 (b) and 21). Similar behaviour was observed in a-Se photoconductor and was linked to electronic processes at the electrode/photoconductor interface that facilitate injection [24]. The analogy with a-Se suggests charge injection from the bias electrode as the primary cause for a lag in the a-PbO. The injection current builds-up during exposure [87,88] interferes with X-ray sensitivity measurements, and misleadingly reduces $W_{\pm}$ values for longer X-ray pulse durations [29]. However, $W_{\pm}$ measurements performed in a-PbO remain within ~3% of the measured values for an increase in pulse duration by a factor of 10 (see Figure 20), indicating an insignificant contribution of X-ray–triggered injection on $W_{\pm}$ measurements in a-PbO. The obtained $W_{\pm}$ values compare very favourably with those reported for a-Se: at F = 10 V/μm, $W_{\pm}$ of a-PbO is ~22 eV/ehp, which is about a half the a-Se value, measured at the same electric field [86].

Overall, these findings suggest an interesting and non-obvious approach to the improvement of X-ray response: to replace the spatial disorder of grain boundaries in polycrystalline films with a uniform disorder in amorphous layers. Such a structural transformation facilitates significant lag improvement in PbO, while preserving its high X-ray sensitivity (i.e., low $W_{\pm}$). In addition, the deposition process behind this structural transformation, also results in a void-free, homogeneous, stoichiometric layer.

Finally, it should be noted that the proposed low-cost optimization of the deposition process which was applied to PbO can potentially be applied (with certain customization, of course) to other materials, like PbI_2, HgI_2 and CdZnTe. Since these materials possess a similar layer structure and suffer from similar artifacts, the advancement of the deposition process with ion bombardment and *amorphization* of the layer structure might also pave the way for many other photoconductors with practical application in commercial devices.

References

[1] F. Busse, W. Ruetten, B. Sandkamp, P. L. Alving, R. J. M. Bastiaens & T. Ducourant. Design and performance of a high-quality cardiac flat detector. *Proc. SPIE* 4682, 819–827 (2002).

[2] P. R. Granfors, D. Albagli, J. E. Tkaczyk, R. Aufrichtig, H. Netel, G. Brunst, J. M. Boudry & D. Luo. Performance of a flat-panel cardiac detector. *Proc. SPIE* 4320, 77 (2001).

[3] M. Simon, K.-J. Engel, B. Menser, X. Badel & J. Linnros. Challenges of pixelated scintillators in medical X-ray imaging. *Nucl. Instrum. Meth. Phys. Res. Sect. A Accel. Spectrom., Detect. Assoc. Equip.* 591 (1), 291–295 (2008).

[4] A. Datta, Z. Zhong & S. Motakef. A new generation of direct X-ray detectors for medical and synchrotron imaging applications. *Sci. Rep.* 10 (1), 20097 (2020).

[5] S. O. Kasap & J. A. Rowlands. Direct-conversion flat-panel X-ray image sensors for digital radiography. *Proc. IEEE* 90 (4), 591–604 (2002).

[6] S. Kasap, J. B. Frey, G. Belev, O. Tousignant, H. Mani, J. Greenspan, L. Laperriere, O. Bubon, A. Reznik, G. DeCrescenzo, K. S. Karim & J. A. Rowlands. Amorphous and Polycrystalline Photoconductors for Direct Conversion Flat Panel X-Ray Image Sensors. *Sensors* 11 (5), 5112–5157 (2011).

[7] B. T. Polischuk, S. Savard, V. Loustaneau, M. Hansroul, S. Cadieux & A. Vaque. Se-based flat-panel detector for screening mammography. *Proc. SPIE* 4320, 582 (2001).

[8] R. R. Karthieka, R. N. Begum & T. Prakash. Direct conversion X-ray sensing nature of bismuth (III) iodide thick films. *Chinese J. Phys.* 71, 643–650 (2021).

[9] Y. Liu, H. Sun, D. Yang, P. Wangyang, X. Gao, Z. Gou & X. Zhu. Electrical properties of x-ray detector based on bismuth tri-iodide single crystal with electrode configuration considering. *Mater. Res. Express* 6 (5), 055902 (2019).

[10] H. Sun, B. Zhao, X. Zhu, S. Zhu, D. Yang, P. Wangyang & X. Gao. Laser-induced surface recrystallization of polycrystalline PbI_2 thick films for X-ray detector application. *Appl. Surf. Sci.* 427, 1146–1151 (2018).

[11] J. F. Condeles & M. Mulato. Polycrystalline lead iodide films produced by solution evaporation and tested in the mammography X-ray energy range. *J. Phys. Chem. Solids* 89, 39–44 (2016).

[12] R. A. Street, S. E. Ready, K. Van Schuylenbergh, J. Ho, J. B. Boyce, P. Nylen, K. Shah, L. Melekhov & H. Hermon. Comparison of PbI_2 and HgI_2 for direct detection active matrix x-ray image sensors. *J. Appl. Phys.* 91 (5), 3345–3355 (2002).

[13] D. Lee, K. Lee & J. Seo. High signal-to-noise ratio HgI_2 X-ray detector assisted with ultraviolet radiation. *Nucl. Instruments Methods Phys. Res. Sect. A Accel. Spectrometers, Detect. Assoc. Equip.* 941, 162364 (2019).

[14] L. E. Antonuk, Y. El-Mohri, Q. Zhao & H. Jiang. Exploration of strategies for implementation of screen-printed mercuric iodide converters in direct detection AMFPIs for digital breast tomosynthesis. *Proc. SPIE* 10132 (2017).

[15] L. Zhou, Z. Huang, X. Zhao, Y. He, L. Chen, M. Xu, K. Zhao, S. Zhang & X. Ouyang. A High-Resistivity ZnO Film-Based Photoconductive X-Ray Detector. *IEEE Photonics Technol. Lett.* 31 (5), 365–368 (2019).

[16] S. Lee, J. S. Kim, K. R. Ko, G. H. Lee, D. J. Lee, D. wook Kim, J. E. Kim, H. K. Kim, D. W. Kim & S. Im. Direct Thermal Growth of Large Scale Cl-doped CdTe Film for Low Voltage High Resolution X-ray Image Sensor. *Sci. Rep.* 8 (1), 14810 (2018).

[17] Y. V. Znamenshchykov, V. V. Kosyak, O. K. Kononov, I. O. Shpetnyi, V. I. Grebinaha, P. M. Fochuk & A. S. Opanasyuk. Electrical, structural and optical properties of $Cd_{1-x}Zn_xTe$ thick polycrystalline films. *Vacuum* 149, 270–278 (2018).

[18] M. Simon, R. A. Ford, A. R. Franklin, S. P. Grabowski, B. Menser, G. Much, A. Nascetti, M. Overdick, M. J. Powell & D. U. Wiechert. Analysis of lead oxide (PbO) layers for direct conversion X-ray detection. *IEEE Trans. Nucl. Sci.* 52 (5), 2035–2040 (2005).

[19] S. Tokuda, S. Adachi, T. Sato, T. Yoshimuta, H. Nagata, K. Uehara, Y. Izumi, O. Teranuma & S. Yamada. Experimental evaluation of a novel CdZnTe flat-panel x-ray detector for digital radiography and fluoroscopy. *Proc. SPIE* 4320, 140 (2001).

[20] S. Tokuda, H. Kishihara, S. Adachi & T. Sato. Improvement of temporal response and output uniformity of polycrystalline CdZnTe films for high-sensitivity x-ray imaging. *Proc. SPIE – Int. Soc. Opt. Eng.* 5030 II, 861 (2003).

[21] S. Adachi, N. Hori, K. Sato, S. Tokuda, T. Sato, K. Uehara, Y. Izumi, H. Nagata, Y. Yoshimura & S. Yamada. Experimental evaluation of a-Se and CdTe flat-panel x-ray detectors for digital radiography and fluoroscopy. *Proc. SPIE* 3977, 38 (2000).

[22] G. Zentai, L. Partain, R. Pavlyuchkova, C. Proano, M. Schieber, K. Shah, P. Bennett, L. Melekhov & H. Gilboa. Comparison of Mercuric Iodide and Lead Iodide X-Ray Detectors for X-Ray Imaging Applications. *IEEE Trans. Nucl. Sci.* 53 (5), 2506–2512 (2006).

[23] P. R. Bennett, K. S. Shah, Y. Dmitriev, M. Klugerman, T. Gupta, M. Squillante, R. Street, L. Partain, G. Zentai & R. Pavyluchova. Polycrystalline lead iodide films for digital X-ray sensors. *Nucl. Instr. Meth. Phys. Res. Sect. A Accel. Spectrom., Detect. Assoc. Equip.* 505 (1), 269–272 (2003).

[24] O. Tousignant, Y. Demers, L. Laperriere, H. Mani, P. Gauthier & J. Leboeuf. Spatial and temporal image characteristics of a real-time large area a-Se x-ray detector. *Proc. SPIE* 5745 (1), 207 (2005).

[25] A. Tsukamoto, S. Yamada, T. Tomisaki, M. Tanaka, T. Sakaguchi, H. Asahina, K. Suzuki & M. Ikeda. Development and evaluation of a large-area selenium-based flat-panel detector for real-time radiography and fluoroscopy. *Proc. SPIE* 3659, 14–23 (1999).

[26] A. Tsukamoto, S. Yamada, T. Tomisaki, M. Tanaka, T. Sakaguchi, H. Asahina & M. Nishiki. Development of a selenium-based flat-panel detector for real-time radiography and fluoroscopy. *Proc. SPIE* 3336, 388 (1998).

[27] D. C. Hunt, O. Tousignant & J. A. Rowlands. Evaluation of the imaging properties of an

amorphous selenium-based flat panel detector for digital fluoroscopy. *Med. Phys.* 31 (5), 1166–1175 (2004).

[28] J. A. Rowlands. Material change for X-ray detectors. *Nature* 550 (7674), 47–48 (2017).

[29] O. Semeniuk, O. Grynko, G. Decrescenzo, G. Juska, K. Wang & A. Reznik. Characterization of polycrystalline lead oxide for application in direct conversion X-ray detectors. *Sci. Rep.* 7 (1), 8659 (2017).

[30] O. Semeniuk, O. Grynko, G. Juska & A. Reznik. Amorphous lead oxide (a-PbO): suppression of signal lag via engineering of the layer structure. *Sci. Rep.* 7 (1), 13272 (2017).

[31] O. Grynko, T. Thibault, E. Pineau, G. Juska & A. Reznik. Bilayer lead oxide X-ray photoconductor for lag-free operation. *Sci. Rep.* 10 (1), 20117 (2020).

[32] O. Grynko, T. Thibault, E. Pineau & A. Reznik. Engineering of a Blocking Layer Structure for Low-Lag Operation of the a-PbO-Based X-Ray Detector. *IEEE Trans. Electron Devices* 68 (5), 2335–2341 (2021).

[33] L. Heijne, P. Schagen & H. Bruining. Television Pick-up Tube for both Light and X-Ray Pictures. *Nature* 173 (4396), 220–220 (1954).

[34] E. H. Stupp & R. S. Levitt. The Plumbicon *in Photoelectronic Imaging Devices, Vol. 2: Devices and Their Evaluation* (eds. L. M. Biberman & S. Nudelman), 275–300 (Springer, 1971).

[35] E. F. DeHaan, A. van der Drift & P. P. M. Schampers. The "Plumbicon", A New Television Camera Tube. *Philips Tech. Rev.* 25 (6), 133–151 (1964).

[36] M. Simon, R. A. Ford, A. R. Franklin, S. P. Grabowski, B. Menser, G. Much, A. Nascetti, M. Overdick, M. J. Powell & D. U. Wiechert. PbO as direct conversion x-ray detector material. *Proc. SPIE* 5368, 188 (2004).

[37] O. Semeniuk, A. Reznik & V. Sukhovatkin. Amorphous lead oxide based energy detection devices and methods of manufacture thereof. *U.S. Patent* 10,163,970 B2 (2018).

[38] G. Zentai. Comparison of CMOS and a-Si flat panel imagers for X-ray imaging. *2011 IEEE Int. Conf. Imag. Syst. Tech.* 194–200 (2011).

[39] G. Zentai. Photoconductor-based (direct) large-area x-ray imagers. *J. Soc. Inf. Disp.* 17 (6), 543 (2009).

[40] Y. Wang & V. Chodavarapu. Differential Wide Temperature Range CMOS Interface Circuit for Capacitive MEMS Pressure Sensors. *Sensors* 15 (2), 4253–4263 (2015).

[41] K. Oka, H. Unoki & T. Sakudo. Growth of single crystals of lead monoxide. *J. Cryst. Growth* 47 (4), 568–572 (1979).

[42] R. C. Keezer, D. L. Bowman & J. H. Becker. Electrical and Optical Properties of Lead Oxide Single Crystals. *J. Appl. Phys.* 39 (4), 2062–2066 (1968).

[43] P. Veluchamy & H. Minoura. Simple electrochemical method for the preparation of a highly oriented and highly photoactive α-PbO film. *Appl. Phys. Lett.* 65 (19), 2431–2433 (1994).

[44] I. Zhitomirsky, L. Gal-Or, A. Kohn & H. W. Hennicke. Electrochemical preparation of PbO films. *J. Mater. Sci. Lett.* 14 (11), 807–810 (1995).

[45] B. Thangaraju & P. Kaliannan. Optical and structural studies on spray deposited α-PbO thin films. *Semicond. Sci. Technol.* 15 (6), 542–545 (2000).

[46] S. Venkataraj, J. Geurts, H. Weis, O. Kappertz, W. K. Njoroge, R. Jayavel & M. Wuttig. Structural and optical properties of thin lead oxide films produced by reactive direct current magnetron sputtering. *J. Vac. Sci. Technol. A Vacuum, Surfaces, Film.* 19 (6), 2870 (2001).

[47] Y. Pauleau & E. Harry. Reactive sputter-deposition and characterization of lead oxide films. *J. Vac. Sci. Technol. A Vacuum, Surfaces, Film.* 14 (4), 2207–2214 (1996).

[48] S. Cho, S. Kang, C. Kwon, M.-S. Yun, J. Park, S. Park, J.-Y. Choi, C. Mun, H. Lee & S. Nam. Effect of Annealing on the X-ray Detection Properties of Nano-sized Polycrystalline Lead Oxide Films. *Jpn. J. Appl. Phys.* 47 (9), 7393–7397 (2008).

[49] L. D. Madsen & L. Weaver. Characterization of Lead Oxide Thin Films Produced by Chemical Vapor Deposition. *J. Am. Ceram. Soc.* 81 (4), 988–996 (2005).

[50] G. R. Dai & J. Y. Xu. Low pressure chemical vapor deposition of PbO thin film from lead dichloride. *J. Mater. Sci. Lett.* 17 (12), 969–971 (1998).

[51] M. Baleva & V. Tuncheva. Laser-assisted deposition of PbO films. *J. Mater. Sci. Lett.* 13 (1), 3–5 (1994).

[52] M. Simon, D. U. Wiechert & C. Feldmann. Lead oxide based photosensitive device and its manufacturing method. *U.S. Patent* 7,649,179 B2 (2010).

[53] O. Semeniuk, A. Csik, S. Kökényesi & A. Reznik. Ion-assisted deposition of amorphous PbO layers. *J. Mater. Sci.* 52 (13), 7937–7946 (2017).

[54] D. U. Wiechert, S. P. Grabowski & M. Simon. Raman spectroscopic investigation of evaporated PbO layers. *Thin Solid Films* 484 (1), 73–82 (2005).

[55] O. Semeniuk, G. Juska, J.-O. Oelerich, M. Wiemer, S. D. Baranovskii & A. Reznik. Charge transport mechanism in lead oxide revealed by CELIV technique. *Sci. Rep.* 6 (1), 33359 (2016).

[56] J. Berashevich, O. Semeniuk, O. Rubel, J. A. Rowlands & A. Reznik. Lead monoxide α-PbO: electronic properties and point defect formation. *J. Phys. Condens. Matter* 25 (7), 075803 (2013).

[57] A. Anders. A structure zone diagram including plasma-based deposition and ion etching. *Thin Solid Films* 518 (15), 4087–4090 (2010).

[58] J. A. Thornton. Influence of apparatus geometry and deposition conditions on the structure and topography of thick sputtered coatings. *J. Vac. Sci. Technol.* 11 (4), 666–670 (1974).

[59] J. A. Thornton. Influence of substrate temperature and deposition rate on structure of thick sputtered Cu coatings. *J. Vac. Sci. Technol.* 12 (4), 830–835 (1975).

[60] K. Müller. Model for ion-assisted thin-film densification. *J. Appl. Phys.* 59 (8), 2803–2807 (1986).

[61] K. H. Muller. Models For Microstructure Evolution During Optical Thin Film Growth. *Modeling of Optical Thin Films* 0821, 36 (1988).

[62] R. B. Sargent. Effects of surface diffusion on thin-film morphology: a computer study. *Modeling of Optical Thin Films II* 1324, 13 (1990).

[63] H. R. Kaufman & J. M. Harper. Ion-assist applications of broad-beam ion sources. *Adv. Thin Film Coat. Opt. Appl.* 5527, 50 (2004).

[64] N. Oudini, G. J. M. Hagelaar, J.-P. Boeuf & L. Garrrigues. Physics and modeling of an end-Hall (gridless) ion source. *J. Appl. Phys.* 109 (7), 073310 (2011).

[65] L. Mahoney, D. Burtner, D. Siegfried & F. Collins. A New End-Hall Ion Source with Improved Performance. *Soc.Vac. Coat. 49th Ann. Tech. Conf. Proc.,* 706–711 (2006).

[66] H. R. Kaufman & J. M. E. Harper. Ion doses for low-energy ion-assist applications. *J. Vac. Sci. Technol. A Vacuum, Surfaces, Film.* 22 (1), 221–224 (2004).

[67] M. G. Krishna, K. N. Rao & S. Mohan. Optical properties of ion assisted deposited zirconia thin films. *J. Vac. Sci. Technol. A Vacuum, Surfaces, Film.* 10 (6), 3451–3455 (1992).

[68] T. H. Allen. Properties Of Ion Assisted Deposited Silica And Titania Films. *Optical Thin Films* 0325, 93–100 (1982).

[69] T. R. Jensen, J. Warren & R. L. Johnson. Ion-assisted deposition of moisture-stable hafnium oxide films for ultraviolet applications. *Appl. Opt.* 41 (16), 3205 (2002).

[70] R. P. Netterfield, W. G. Sainty, P. J. Martin & S. H. Sie. Properties of CeO_2 thin films prepared by oxygen-ion-assisted deposition. *Appl. Opt.* 24 (14), 2267 (1985).

[71] K. Wang, S. Abbaszadeh, K. S. Karim, J. A. Rowlands & A. Reznik. Reactive Ion-Assisted Deposition of Cerium Oxide Hole-Blocking Contact for Leakage-Current Suppression in an Amorphous Selenium Multilayer Structure. *IEEE Sens. J.* 15 (7), 3871–3876 (2015).

[72] J. R. McNeil, A. C. Barron, S. R. Wilson & W. C. Herrmann. Ion-assisted deposition of optical thin films: low energy vs high energy bombardment. *Appl. Opt.* 23 (4), 552 (1984).

[73] L. Wang, M.-H. Yoon, G. Lu, Y. Yang, A. Facchetti & T. J. Marks. High-performance transparent inorganic–organic hybrid thin-film n-type transistors. *Nat. Mater.* 5 (11), 893–900 (2006).

[74] M. Tan, Y. Deng & Y. Hao. Enhanced Thermoelectric Properties and Superlattice Structure of a Bi_2Te_3/ZrB_2 Film Prepared by Ion-Beam-Assisted Deposition. *J. Phys. Chem. C* 117 (40), 20415–20420 (2013).

[75] S. Tepavcevic, Y. Choi & L. Hanley. Surface Polymerization by Ion-Assisted Deposition for Polythiophene Film Growth. *J. Am. Chem. Soc.* 125 (9), 2396–2397 (2003).

[76] M. S. Farhan, E. Zalnezhad, A. R. Bushroa & A. A. D. Sarhan. Electrical and optical properties of indium-tin oxide (ITO) films by ion-assisted deposition (IAD) at room temperature. *Int. J. Precis. Eng. Manuf.* 14 (8), 1465–1469 (2013).

[77] X. W. Zhang, H.-G. Boyen, N. Deyneka, P. Ziemann, F. Banhart & M. Schreck. Epitaxy of cubic boron nitride on (001)-oriented diamond. *Nat. Mater.* 2 (5), 312–315 (2003).

[78] C. A. Klein. Bandgap Dependence and Related Features of Radiation Ionization Energies in Semiconductors. *J. Appl. Phys.* 39 (4), 2029–2038 (1968).

[79] C. Haugen, S. O. Kasap & J. A. Rowlands. Charge transport and electron-hole-pair creation energy in stabilized a-Se x-ray photoconductors. *J. Phys. D. Appl. Phys.* 32 (3), 200–207 (1999).

[80] M. Blevis, D. C. Hunt & J. A. Rowlands. Measurement of x-ray photogeneration in amorphous selenium. *J. Appl. Phys.* 85 (11), 7958–7963 (1999).

[81] M. F. Stone, W. Zhao, B. V. Jacak, P. O'Connor, B. Yu & P. Rehak. The x-ray sensitivity of amorphous selenium for mammography. *Med. Phys.* 29 (3), 319–324 (2002).

[82] G. Bertuccio & R. Casiraghi. Study of silicon carbide for X-ray detection and spectroscopy. *IEEE Trans. Nucl. Sci.* 50 (1), 175–185 (2003).

[83] A. M. Barnett, J. E. Lees, D. J. Bassford & J. S. Ng. Determination of the electron-hole pair creation energy in $Al_{0.8}Ga_{0.2}As$. *J. Instrum.* 7 (6), P06016 (2012).

[84] G. Bertuccio & D. Maiocchi. Electron-hole pair generation energy in gallium arsenide by x- and γ-photons. *J. Appl. Phys.* 92 (3), 1248–1255 (2002).

[85] A. Rowlands, G. DeCrescenzo & N. Araj. X-ray imaging using amorphous selenium: Determination of x-ray sensitivity by pulse height spectroscopy. *Med. Phys.* 19 (4), 1065–1069 (1992).

[86] S. Kasap, J. B. Frey, G. Belev, O. Tousignant, H. Mani, L. Laperriere, A. Reznik & J. A. Rowlands. Amorphous selenium and its alloys from early xeroradiography to high resolution X-ray image detectors and ultrasensitive imaging tubes. *Phys. Stat. Sol. (B)* 246 (8), 1794–1805 (2009).

[87] S. Abbaszadeh, C. C. Scott, O. Bubon, A. Reznik & K. S. Karim. Enhanced Detection Efficiency of Direct Conversion X-ray Detector Using Polyimide as Hole-Blocking Layer. *Sci. Rep.* 3 (1), 3360 (2013).

[88] B. Zhao & W. Zhao. Temporal performance of amorphous selenium mammography detectors. *Med. Phys.* 32 (1), 128–136 (2004).

[89] W. Zhao, G. DeCrescenzo & J. A. Rowlands. Investigation of lag and ghosting in amorphous selenium flat-panel x-ray detectors. *Proc. SPIE* 4682, 9–20 (2002).

[90] F. Olschner, J. C. Lund & I. Stern. Monte Carlo simulation of gamma ray spectra from semiconductor detectors. *IEEE Trans. Nucl. Sci.* 36 (1), 1176–1179 (1989).

[91] H. H. Barrett, J. D. Eskin & H. B. Barber. Charge Transport in Arrays of Semiconductor Gamma-Ray Detectors. *Phys. Rev. Lett.* 75 (1), 156–159 (1995).

[92] O. Kim, T. J. Kwon, J. K. Kim & J. H. Ha. A New Approach for Evaluating the Mobility-lifetime Products of Electron-hole Pairs in Semiconductor Detectors. *J. Korean Phys. Soc.* 59 (1), 20–26 (2011).

[93] G. Scannavini, P. Chirco, G. Baldazzi, G. Guidi, E. Querzola, P. Partemi, M. Rossi, M. Zanarini, F. Casali & E. Caroli. Computer simulation of charge trapping and ballistic deficit effects on gamma-ray spectra from CdTe semiconductor detectors. *Nucl. Instrum. Meth. Phys. Res. Sect. A Accel. Spectrom., Detect. Assoc. Equip.* 353 (1–3), 80–84 (1994).

[94] S. Miyajima, K. Imagawa & M. Matsumoto. CdZnTe detector in diagnostic x-ray spectroscopy. *Med. Phys.* 29 (7), 1421–1429 (2002).

[95] W. Akutagawa & K. Zanio. Gamma Response of Semi-insulating Material in the Presence of Trapping and Detrapping. *J. Appl. Phys.* 40 (9), 3838–3854 (1969).

[96] O. Semeniuk, G. Juska, J. O. Oelerich, K. Jandieri, S. D. Baranovskii & A. Reznik. Transport of electrons in lead oxide studied by CELIV technique. *J. Phys. D. Appl. Phys.* 50 (3), 035103 (2017).

[97] Z. Kabir & S. O. Kasap. Charge collection and absorption-limited sensitivity of x-ray photoconductors: Applications to a-Se and HgI_2. *Appl. Phys. Lett.* 80 (9), 1664–1666 (2002).

[98] R. Redus. Efficiency of Amptek XR-100T-CdTe and CZT detectors. *Application Note ANCZT-1, Rev. 2* (2002).

[99] H. Scher & E. W. Montroll. Anomalous transit-time dispersion in amorphous solids. *Phys. Rev. B* 12 (6), 2455–2477 (1975).

[100] G. Pfister & H. Scher. Dispersive (non-Gaussian) transient transport in disordered solids. *Adv. Phys.* 27 (5), 747–798 (1978).

[101] P. W. Nicholson. *Nuclear Electronics* (Wiley, 1974).

[102] J. H. Siewerdsen, I. A. Cunningham & D. A. Jaffray. A framework for noise-power spectrum analysis of multidimensional images. *Med. Phys.* 29 (11), 2655–2671 (2002).

[103] P. R. Granfors, R. Aufrichtig, G. E. Possin, B. W. Giambattista, Z. S. Huang, J. Liu & B. Ma. Performance of a 41×41 cm^2 amorphous silicon flat panel x-ray detector designed for angiographic and R&F imaging applications. *Med. Phys.* 30 (10), 2715–2726 (2003).

Chapter 3

Bilayer a-PbO/poly-PbO detector

This topic has been elaborated in the following publication:

Oleksandr Grynko, Tristen Thibault, Emma Pineau, Gytis Juska, Alla Reznik. Bilayer lead oxide X-ray photoconductor for lag-free operation. *Scientific Reports*, Volume 10, Article number 20117 (2020). DOI: 10.1038/s41598-020-77050-w

The full text of the publication is listed below.

Bilayer Lead Oxide X-ray Photoconductor for Lag-free Operation

Oleksandr Grynko[1*], Tristen Thibault[2], Emma Pineau[2], Gytis Juska[3], Alla Reznik[2,4]

1. Chemistry and Materials Science Program, Lakehead University, 955 Oliver Road, Thunder Bay, ON, P7B 5E1, Canada.
2. Physics Department, Lakehead University, 955 Oliver Road, Thunder Bay, ON, P7B 5E1, Canada.
3. Department of Solid State Electronics, Vilnius University, Saulėtekio 9 III k., 10222 Vilnius, Lithuania.
4. Thunder Bay Regional Health Research Institute, 980 Oliver Road, Thunder Bay, ON, P7B 6V4, Canada.

**e-mail*: ogrynko@lakeheadu.ca (O. Grynko).

Abstract

Polycrystalline Lead Oxide (poly-PbO) was considered one of the most promising photoconductors for the direct conversion X-ray medical imaging detectors due to its previous success in optical imaging, i.e., as an optical target in so-called Plumbicon video pick-up tubes. However, a signal lag, which accompanies X-ray excitation, makes poly-PbO inapplicable as an X-ray–to–charge transducer in real-time X-ray imaging. In contrast, the recently synthesized Amorphous Lead Oxide (a-PbO) photoconductor is essentially lag-free. Here, we report on our approach to a PbO detector where a thin layer of a-PbO is combined with a thick layer of poly-PbO for lag-free operation. In the presented a-PbO/poly-PbO bilayer structure, the poly-PbO layer serves as an X-ray–to–charge transducer while the a-PbO acts as a lag prevention layer. The hole mobility in the a-PbO/poly-PbO bilayer structure was measured by photo-Charge Extraction by Linearly Increasing Voltage technique at different temperatures and electric fields to investigate charge transport properties. It was found that the hole mobility is similar to that in a-Se – currently

the only commercially viable photoconductor for the direct conversion X-ray detectors. Evaluation of the X-ray temporal performance demonstrated complete suppression of signal lag, allowing operation of the a-PbO/poly-PbO detector in real-time imaging.

Introduction

Direct conversion detectors opened a new era in X-ray medical imaging because of the number of advantages intrinsic to the direct conversion scheme, such as spatial resolution that is limited only by the pixel dimensions and high dose efficiency even at low radiation exposure.

In the direct conversion method, incident X-rays are absorbed in a layer of photoconductor that directly generates electron-hole pairs, which are afterwards separated by an electric field to produce an electrical signal. The photogenerated electrons and holes drift towards the opposite electrodes, making it possible to create an image with a thick detector layer while maintaining high spatial resolution. The first commercial mammographic direct conversion detectors based on amorphous selenium (a-Se) photoconductor to directly convert incident X-rays to charge, which is subsequently electronically read out by a two-dimensional array of a-Si:H thin film transistors (TFTs), made a breakthrough in the breast imaging field due to the excellent detectability of small breast lesions [1].

Currently, the only commercially feasible photoconductor for X-ray imaging is a-Se, which limits the extensive use of the direct conversion scheme. Indeed, a-Se has a low atomic number *Z*, and thus, is efficient only when low-energy X-rays are used, e.g., in mammography. To expand the benefits of direct conversion detectors over the diagnostic energy range, i.e., in radiography and fluoroscopy, a-Se must be substituted by a high-*Z* material, which can efficiently absorb higher energy X-rays.

Since X-ray imaging detectors should normally have a large active area (one cannot converge X-rays), single crystalline photoconductors are ruled out from the application in direct conversion detectors in conjunction with large area a-Si:H flat panel technology (i.e., active matrix flat panel imagers or AMFPIs). Thus, it is imperative to focus on amorphous and polycrystalline phases of high-*Z* photoconductors, that can be directly deposited on an imaging array of a large area. Potential X-ray photoconductors such as polycrystalline layers of BiI_3 [2], PbI_2 [3,4], HgI_2 [5-7],

ZnO [8], CdTe [9], $Cd_{1-x}Zn_xTe$ [10], and PbO [11] have been investigated and have shown potential for use in direct conversion detectors. The X-ray–to–charge conversion rate of these materials is 3-8 times larger than that of a-Se and thus, they are capable of X-ray quantum noise limited operation at low exposures, since the X-ray quantum noise can prevail over the electronic noise. The performance of these polycrystalline photoconductors is far from ideal due to either a large dark current, incomplete charge collection, or inadequate temporal response to X-ray irradiation, appearing as a residual current after X-ray exposure is terminated, i.e., signal lag (or from a combination of these problems). In addition, the deposition of poly-CdTe and poly-$Cd_{1-x}Zn_xTe$ layers requires a high substrate temperature (400 – 600 °C), which is incompatible with most of the readout electronics, or requires a hybrid deposition method, where the film is firstly deposited on the glass or alumina substrate and then coupled to the readout circuitry. The latter involves very precise alignment of the photoconductor relative to the matrix array to achieve proper pixel-to-pixel bonding that is technologically challenging, especially for high-resolution detectors.

Another promising class of materials to be used in radiation detection are perovskite semiconductors [12]; however, they are at a very early stage of the development (suffering from material instability, signal lag and, comparatively high dark current, technological difficulties in manufacturing a thick and uniform layer over a large area) and are not mature enough to be considered as a practical solution to improve radiation medical imaging.

It should be mentioned that among the potential X-ray–to–charge transducers listed above, polycrystalline Lead Oxide (poly-PbO) is especially promising because, similarly to a-Se, it has a long history of commercial utilization in optical imaging. Previously, thin layers of poly-PbO were used in “Plumbicon” video pick-up tubes that were widely used for broadcast, fluoroscopy and digital subtraction angiography in conjunction with image intensifiers. However, the first prototype of poly-PbO based X-ray detector with the radiography-thick photoconductor film was unsuccessful. The photoconductor exhibited signal lag [13] that did not permit the use of PbO detectors in real time fluoroscopic imaging, which is the most clinically demanding application [14].

Recently, we reported on the development of a new polymorphic form of the PbO material, namely amorphous Lead Oxide (a-PbO), which had not been previously synthesized [15]. In contrast to

its polycrystalline counterpart, a-PbO is dense, capable of withstanding higher electric fields with lower dark current and exhibits no signal lag [16]. In this work, we use a-PbO in a bilayer PbO structure, where a thick layer of poly-PbO serves as a recording and charge transport layer while a thin layer of a-PbO acts as a lag-preventing layer.

The use of multilayer photoconductive structures is a standard solution in direct conversion detectors. Indeed, practical a-Se direct conversion detectors utilize a multilayered structure, consisting of a thick photoconducting layer of stabilized a-Se, sandwiched between one or two adjacent blocking layers needed to maintain an acceptable level of dark current.

In the majority of those detectors, two blocking layers are identified as *n*-like (hole blocking) and *p*-like (electron blocking). Examples of *n*-like layers are a-Se alloyed with a small percent of As and doped with alkali metal (usually Na or LiF) [17-23], cold-deposited a-Se [19,20], Sb_2S_3 [24] and CeO_2 [23,25]. Among *p*-like layers are As_2Se_3 [17-20,24], a-Se doped with Cl [22], and Sb_2S_3 [24-26]. Additional layers may be used, such as Arsenic-rich a-Se layers to retard crystallite formation at the interface [24,26,27]; and protective overcoating layer such as nigrosine [28], Parylene [29], epoxy resin [26]. As it is seen, the manufacturing of an a-Se based detector requires multistage doping and alloying with different elements, normally performed in one deposition cycle without breaking the vacuum. This process is technically challenging and requires precise control to avoid cross-contamination, leading to high deposition cost [30].

Our approach to combine two allotropic forms of the same material, namely, PbO, in a blocking structure reduces technical complexity, in comparison with a-Se technology. At the same time, it will allow to combine excellent (low) ionization energy inherent to PbO, adequate hole mobilities and low dark current at practical electric fields. This holds a potential to make the direct conversion system simpler and hence, more economical to manufacture. Although we do not claim that the developed technology can be immediately used in commercial products, we show that it allows for lag-free real-time imaging in the diagnostic energy range. We also report on the direct measurements of hole mobilities and demonstrate, for the first time, the application of the bilayer PbO structure as a direct conversion X-ray detector.

Results

Experimental sample

A schematic presentation of a bilayer Lead Oxide structure is shown in Figure 1a. The bottom 2 μm lag-preventing a-PbO layer was deposited on an ITO-coated glass substrate (bottom biased electrode) by an ion-assisted thermal evaporation technique [31]. Subsequently, the a-PbO layer was covered by a 12 μm layer of poly-PbO (recording and charge transport layer) using conventional thermal evaporation [31]. Although this sequential deposition of amorphous and polycrystalline layers was performed in a single deposition cycle (without breaking the vacuum), it should be noted that it can be done in separate evaporators, giving essentially identical results. Finally, a 200 nm thick Au contact was sputtered atop a-PbO/poly-PbO structure by magnetron sputtering to serve as the top readout electrode.

The SEM image of the cross-section of the sample is shown in Figure 1b. As can be seen, the thin and dense layer of amorphous material in the lower part of the structure transforms into a less dense, inhomogeneous disordered layer of polycrystalline material. It should be noted that the structure of the poly-PbO layer in the presented bilayer structure is slightly different from the previously reported single poly-PbO layer structure. Indeed, a single poly-PbO film is essentially a porous network of individual platelets oriented mainly in the growth direction [31], whereas the layer in the current sample consists of overlapping flakes.

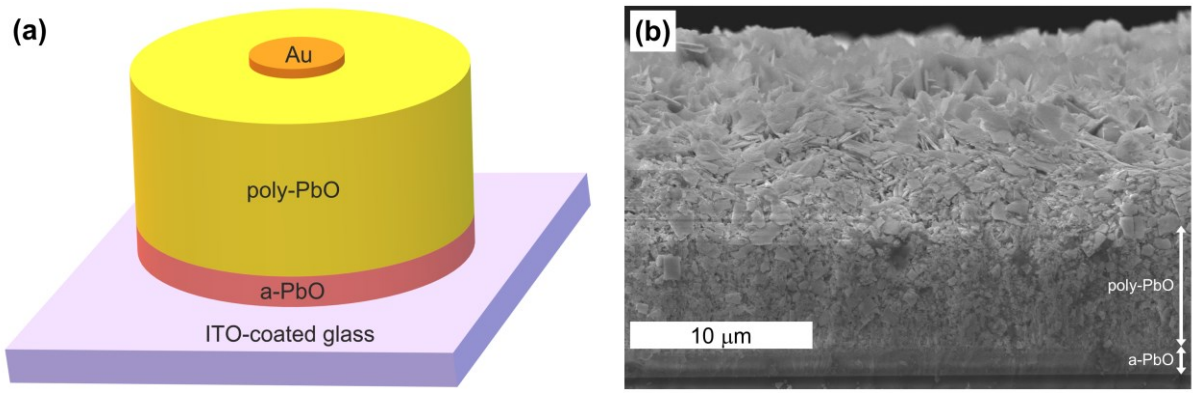

Figure 1. Schematic diagram (a) and cross-sectional SEM image (b) of a bilayer a-PbO/poly-PbO structure.

Mobility measurements

Hole mobility was measured by the photo-Charge Extraction by Linearly Increasing Voltage (CELIV) technique in a range of electric fields (0.03–0.22 V/μm) and temperatures (260–350 K). The choice of CELIV was determined by its proven efficacy in the evaluation of field and temperature dependencies of mobilities in single poly-PbO layers, characterized by dispersive carrier transport with mobilities which decrease in the course of time. This feature makes a conventional Time-of-Flight (TOF) technique ineffective for transport characterization. In contrast, the theory of CELIV was recently extended to dispersive transport regime [32] making it a technique of choice as an alternative to TOF for disordered materials with dispersive transport.

In photo-CELIV, a light pulse is used to generate charge carriers in the volume of an unbiased sample. The wavelength of optical excitation (595 nm) was chosen to provide a uniform bulk absorption so that electron-hole pairs are generated in the volume of the layer. Subsequently, a linearly increasing voltage is applied to the sample to extract the photo-generated carriers. As the applied voltage increases, so does the photocurrent since charge carriers are extracted faster. At the end of the extraction, when most carriers have been collected, the photocurrent decays (Figure 2).

The carrier mobility is derived from the measured time needed to reach the peak of the photocurrent. For disordered materials with dispersive transport, the mobility is calculated using an equation

$$\mu = \frac{\alpha(\alpha+1)}{2\alpha+1}\frac{d^2}{t_{peak}^2 A}, \tag{1}$$

where d – detector's thickness, t_{peak} – time to the peak of the photocurrent, A – slope of the voltage ramp, α – dispersion parameter derived from the relationship [32]

$$t_{peak} \sim A^{-\frac{1}{1+\alpha}}. \tag{2}$$

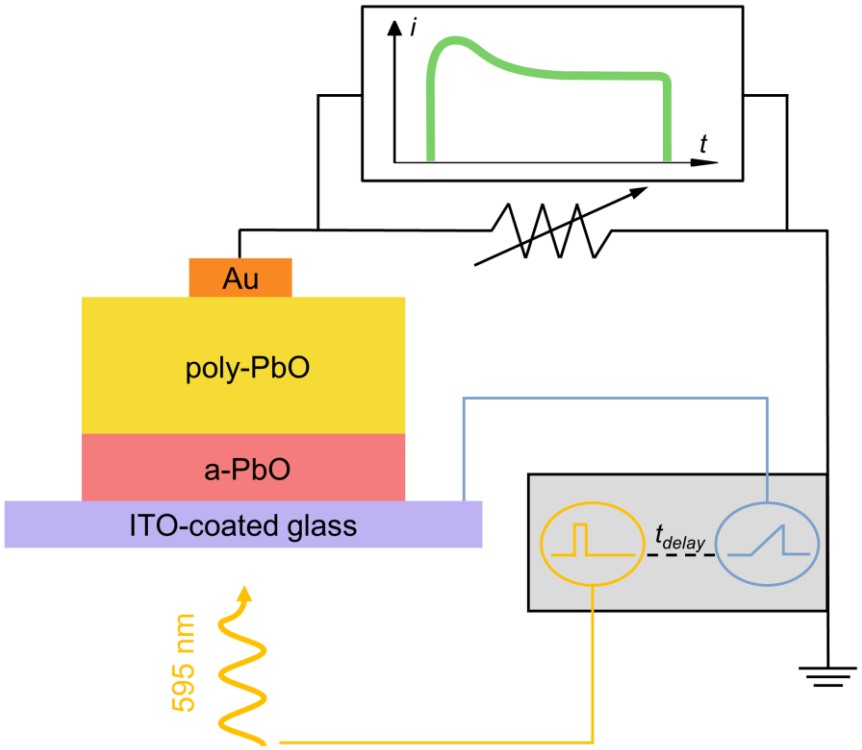

Figure 2. Schematic diagram of photo-CELIV experimental apparatus.

A typical CELIV response at given experimental conditions is shown in Figure 3, where T – temperature, R_{osc} – input resistance of the oscilloscope, t_{pulse} – duration of a light pulse, and t_{delay} – time delay between the light and voltage pulses. The dark-response, which is a capacitive component of the current, was subtracted from the photo-response, and the peak time was measured from the differential photocurrent transient.

To satisfy the requirements of the CELIV model and to prevent the accumulation of space charge [33], the magnitude and duration of the light pulse were adjusted to make the amplitude of the photocurrent (differential signal) smaller than the capacitive (dark) signal; and the input resistance of the oscilloscope was adjusted to minimize the RC-component of the signal. Also, since it has been previously shown that holes are much faster carriers in poly-PbO [32,34], the experimental conditions were tuned (i.e., a voltage pulse of low amplitude and short duration was used throughout the experiments) to make the photocurrent caused by the drift of holes only, so that slower electrons do not contribute to the recorded photocurrent.

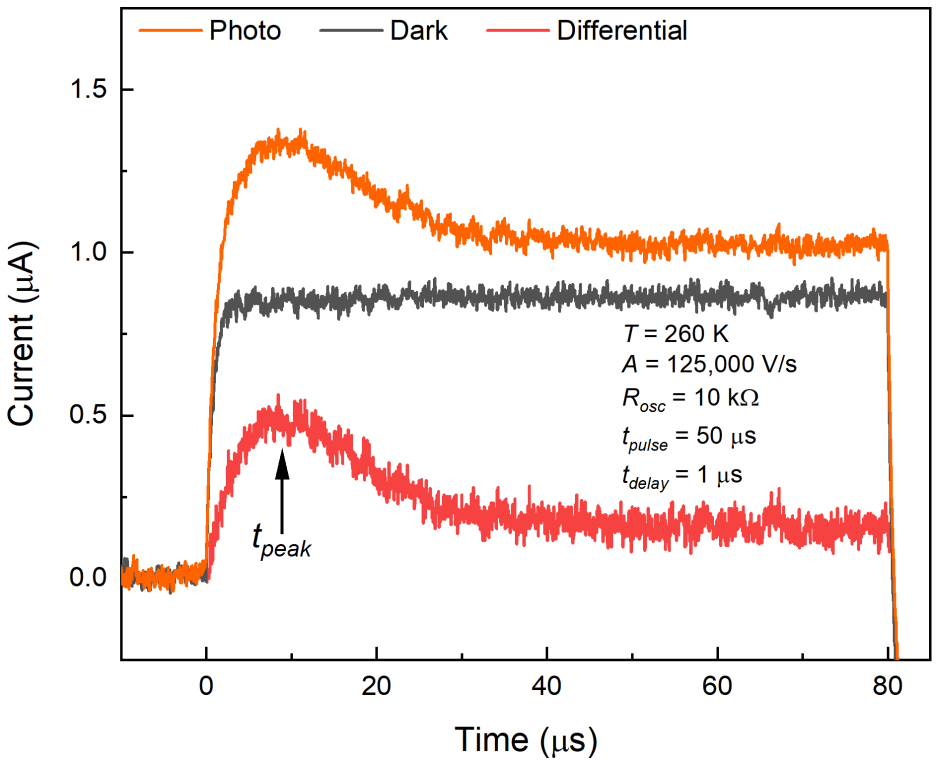

Figure 3. A typical photo-CELIV, dark-CELIV current transients, and differential curve. The peak time is measured from the differential signal, exhibiting an apparent photo-peak.

Figure 4 shows experimentally measured time to peak dependence on the voltage ramp at different temperatures. A slope of a log-log fit curve yields a value of the dispersion parameter $\alpha = 0.42$, from equation (2). The dispersion parameter is temperature independent, similarly to what has been found in single poly-PbO layers [32]; however, its value is twice larger than that in single poly-PbO.

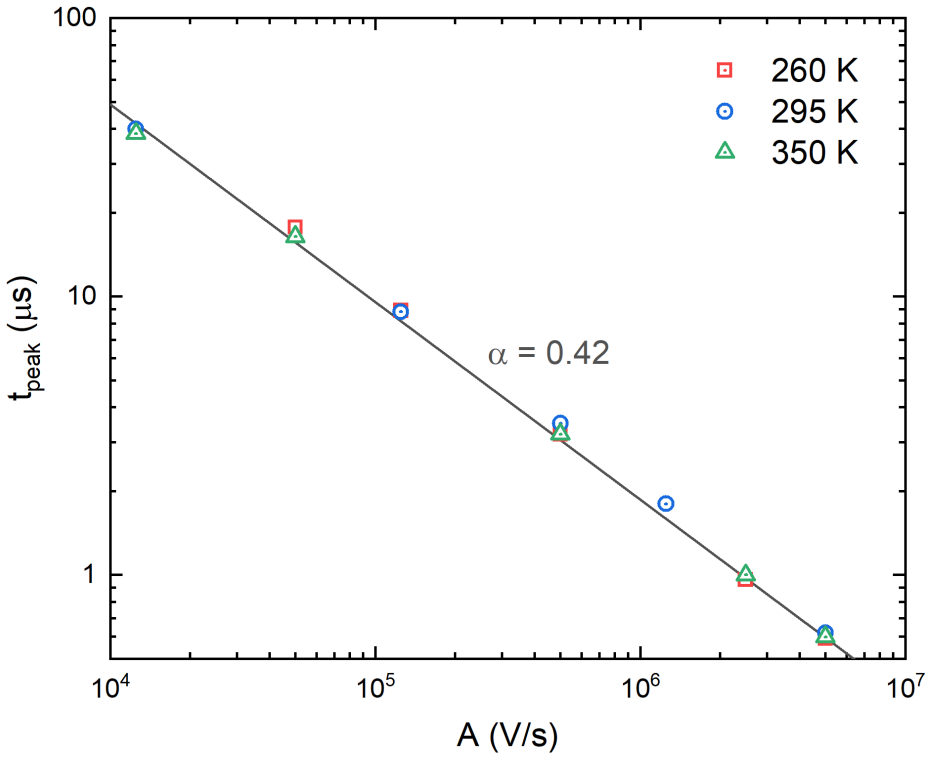

Figure 4. Time to peak dependence on voltage ramp at different temperatures. The dispersion parameter derived from a slope of a log-log fit line is independent of temperature.

The mobility of holes $\mu(F)$ was calculated using equation (1) for electric field at the time of maximum extraction $\left(F = \frac{A \cdot t_{peak}}{d}\right)$ at different voltage ramps A and temperatures (Figure 5). Hole mobility is strongly dependent on the electric field and reaches a value of 0.35 cm^2/Vs at 0.22 V/µm. To compare, the mobility of holes in a-Se is 0.15 cm^2/Vs at 1 V/µm at room temperature [35]. The weak dependence of mobility on temperature and the strong dependence on applied field indicates a dispersive transport regime mainly governed by spatial inhomogeneity [32].

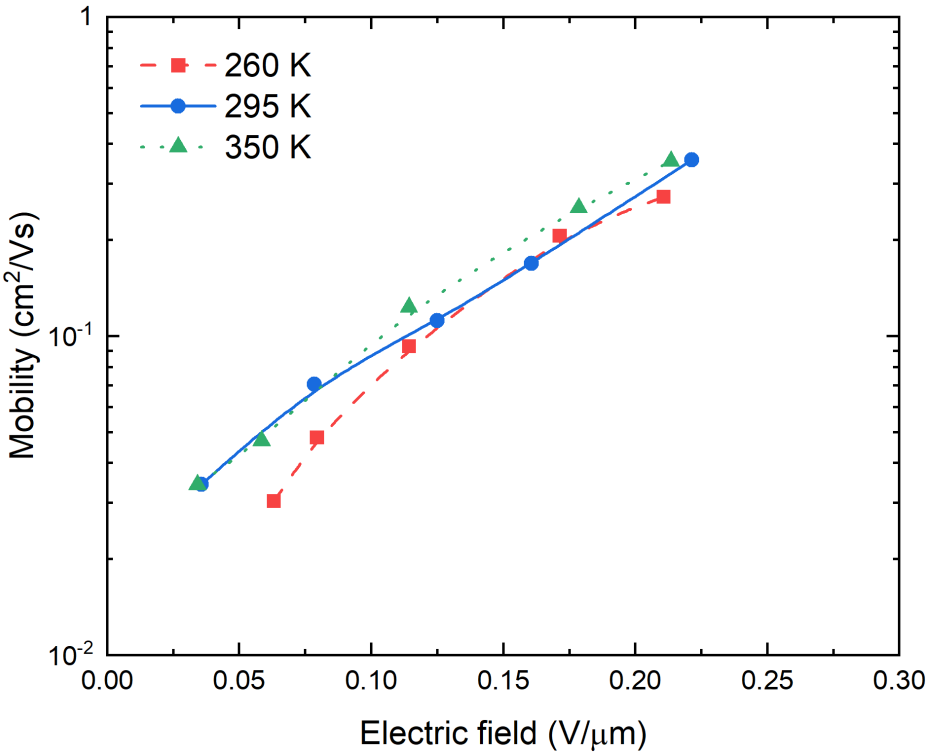

Figure 5. Hole mobility dependence on electric field at different temperatures. The mobility is independent of temperature but have a strong dependence on electric field.

Temporal performance evaluation

The temporal performance was examined by the X-ray induced Photocurrent Method (XPM) in a pulsed mode. The photocurrent in a bilayer PbO structure was measured at an electric field of 10 V/μm (negative bias on ITO) under 1 s long X-ray exposure, modulated using a rotating chopper at various frequencies in the range of 10-60 Hz and 50 % duty cycle (Figure 6). In this test, image lag would reveal itself as an increase in the signal in each frame [36].

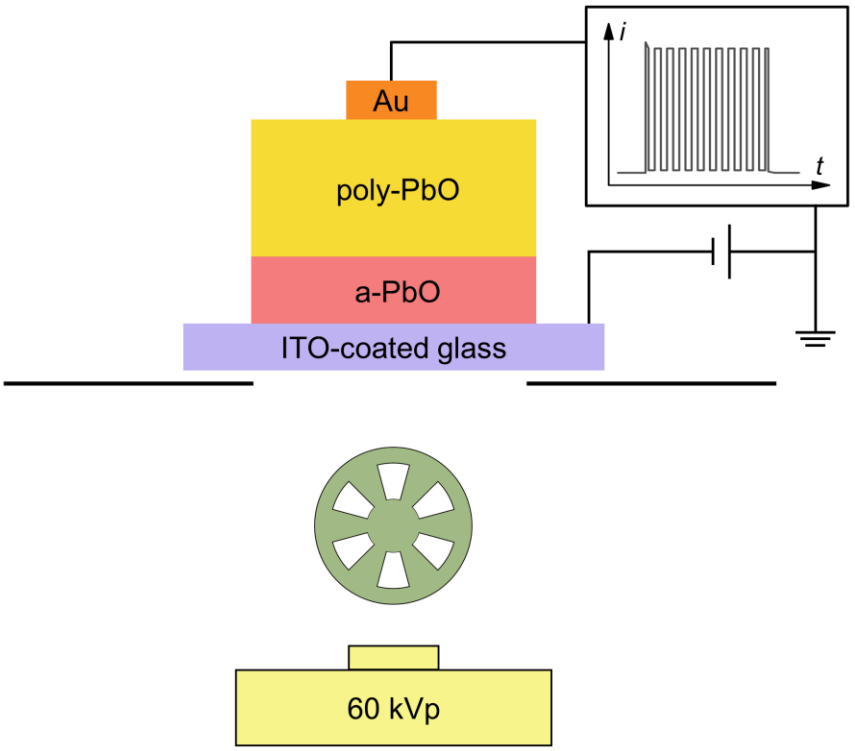

Figure 6. Schematic diagram of XPM setup in a fluoroscopic mode.

To demonstrate this, Figure 7 compares outputs of a bilayer PbO structure and a single poly-PbO layer biased at 5 V/μm and irradiated with X-rays pulsed at a frequency of 10 frames per second (fps). The exposure was 2 s long, during which both samples were exposed to 20 X-ray pulses (100 ms alternating intervals with open and closed chopper). When irradiated with pulsed X-rays, a rise of the photocurrent level with each subsequent frame is evident in the single poly-PbO layer. In addition, there is a well-pronounced residual signal, that decays to zero in approximately 2 s after the termination of X-ray exposure. In contrast, a bilayer a-PbO/poly-PbO structure shows a stable photocurrent value and no signal lag.

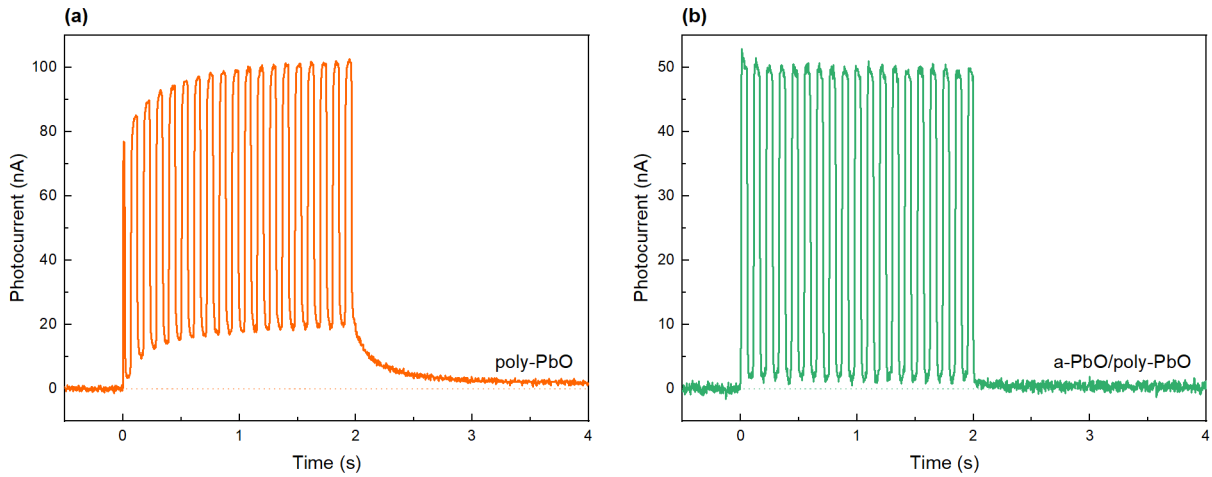

Figure 7. Comparison of X-ray response to pulsed irradiation of (a) poly-PbO and (b) bilayer a-PbO/poly-PbO detectors. Poly-PbO exhibits signal build-up and prolonged residual signal after the termination of X-ray pulse, while bilayer PbO detector shows perfect temporal response. It should be noted that the poly-PbO sample used in this experiment is thicker than a-PbO/poly-PbO, thus it yields a higher amplitude of X-ray response.

The temporal performance of the bilayer detector shows a nearly constant amplitude of the signal in each frame even at a high readout rate (Figure 8). A uniform amplitude during the X-ray exposure indicates no build-up of the injection current, allowing maintenance of constant dark current. After the termination of the X-ray pulse, the photocurrent drops rapidly to zero level with no residual signal, proving lag-free operation.

Frequency of 30 fps used in this experiment corresponds to readout rate conventionally used in a real-time fluoroscopy imaging. A reduced frame rate can be used to increase the signal-to-noise ratio (SNR) of the detector and to moderate patient dose. A higher readout rate might be necessary when one must image a rapidly changing process, such as heart beating (cardiac imaging and coronary catheterization) [37].

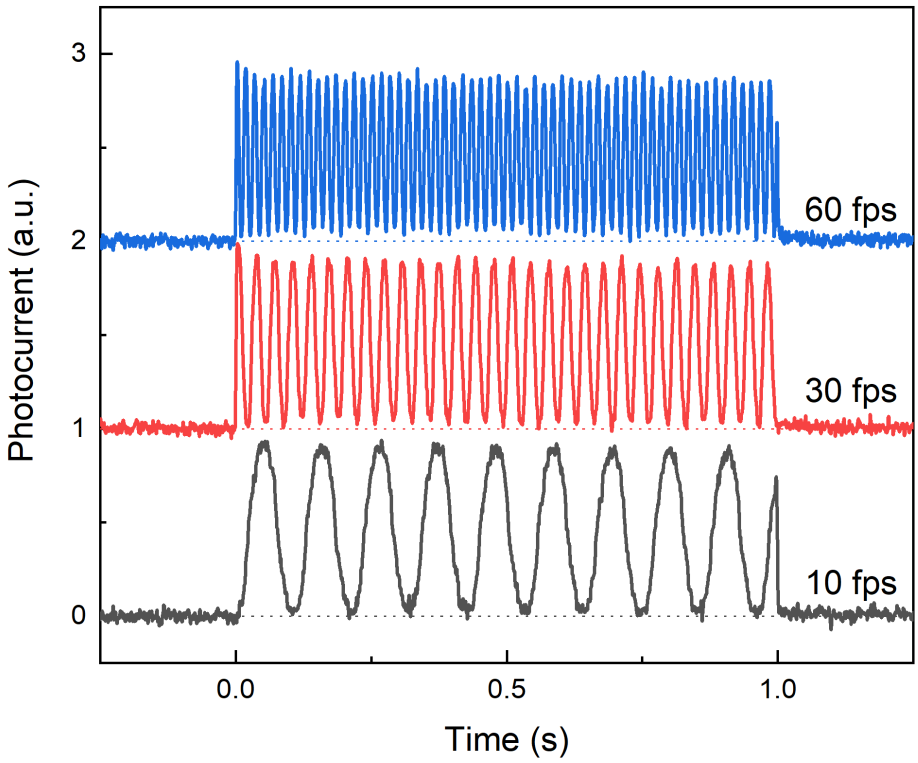

Figure 8. A bilayer detector's response to X-ray irradiation pulsed at different frequencies. Each waveform was normalized and shifted for better visualization. The first and the last frames are affected by asynchronization between the chopper and X-ray pulse, and nonuniformity of exposure at the beginning of the pulse.

Discussion

The performance of a-PbO/poly-PbO bilayer structure has been investigated in terms of whether combining these PbO polymorphs into a multilayer structure allows to consolidate the adequate hole mobility inherent in poly-PbO with the excellent X-ray temporal response inherent in a-PbO layers. CELIV measurements confirmed that hole transport in the bilayer structure is dispersive and qualitatively similar to that in single layers of poly-PbO [32]. Weak temperature dependency of mobility μ and dispersion parameter α, and strong field dependence of μ indicates that dispersion is governed by spatial disorder rather than energy disorder. Mobility of holes reaches value of 0.35 cm^2/Vs at relatively low field 0.22 V/μm (the upper value of the applied electric field was limited by the bandwidth of the function generator). The fact that mobility increases rapidly with an increase in electric field is very desirable since it provides a tool to improve the carrier schubweg

i.e. the average distance drifted before a carrier is lost to traps (schubweg is a product of the carrier drift mobility μ, the lifetime τ and field F, i.e. $\mu\tau F$) and to avoid depth dependent charge collection. Both the dispersion parameter and hole mobility obtained for a bilayer a-PbO/poly-PbO structure are somewhat higher than those for poly-PbO. This can be attributed to the differences in structural heterogeneity between a single poly-PbO and that grown on a-PbO: depositing a poly-PbO layer on a-PbO sublayer makes hole transport less dispersive and increases hole mobility.

Evaluation of the temporal response of the bilayer structure with the pulsed X-ray radiation did not reveal signal lag – a major obstacle for application of poly-PbO layers in the direct conversion X-ray detectors. Indeed, the presence of signal lag and subsequently, image lag, does not permit to use poly-PbO detectors in the most demanding clinical application that is real time fluoroscopic imaging. Dynamic readout, as that used in real time applications, requires very little to no lag at the end of each frame, otherwise previous images will be superimposed with the subsequent ones, thus resulting in a misleading view. The elimination of signal lag can be explained by decreasing charge trapping at a-PbO/poly-PbO interface and suppressing X-ray triggered injection caused by local enhancement of the electric field at the interface between the electrode and photoconductor [13]. In a bilayer configuration, a lag-preventing layer of a-PbO separates poly-PbO from the electrode, preventing charge injection and eliminating image lag.

Despite this, the dark current of a bilayer structure is still higher than the recommended value for digital flat panel detectors (~ 10 pA/mm^2) [38]. Further decrease in the dark current may be achieved by using a thin blocking layer between the electrodes and PbO bilayer. One of the most suitable candidates is polyimide (PI). It is a well-developed material that was already successfully used with a-Se photoconductors [36]. Careful optimization of the film's thickness allows the tuning of its resistivity to prevent significant voltage drop across the blocking layer as well as redistribution of the electric field inside the structure [39]. It should be noted that polyimide film can be easily applied by a conventional spin coating technique, in contrast to complicated process of growing of the doped layers mentioned earlier. The development of the PI blocking layer to be used in a-PbO/poly-PbO-based X-ray detectors is left for future work.

Overall, our results demonstrate that combining an a-PbO lag-preventing layer with a poly-PbO X-ray–receiving layer in a bilayer structure allows to obtain lag-free operation while preserving

adequate hole mobilities (relative to other disordered photoconductors) needed for adequate schubweg and high efficiency in collecting X-ray generated charge.

Methods

Sample preparation

The bilayer PbO sample was thermally evaporated on Indium Tin Oxide (ITO) coated glass substrate. To form a-PbO layer, a high purity (5N) yellow PbO powder was evaporated at the temperature ~1000 °C in atmosphere of ionized oxygen at the pressure ~0.1 Pa. The growing layer was continuously bombarded by Oxygen ions with energy ~70 eV. The poly-PbO layer was formed from the same powder and at the similar temperatures, but in contrast to a-PbO, evaporation took place in atmosphere of molecular oxygen at the pressure ~0.3 Pa. The substrate temperature was kept below 150 °C in both processes. A top gold contact was sputtered *ex situ* in a dedicated chamber. Since poly-PbO is known to degrade under ambient conditions by forming a hydro-cerussite compound [14], all measurements were performed in the protective atmosphere of dry Nitrogen.

CELIV apparatus

A sample was placed in a heating-cooling stage Linkam LTS350 that enables a precise temperature control in a wide range of temperatures. A 2-channel function generator Tektronix AFG 3022C was used to apply a linearly increasing voltage pulse on ITO and trigger a light pulse from the ITO side. The current transients were readout from Au electrode on the oscilloscope Tektronix TDS 2024C with adjustable input resistance. For an excitation LED light pulse with a radiant power ~ 100 μW and a wavelength of 595 nm, the attenuation depts in Lead Oxide is 90 μm [40], which is much larger than the detector's thickness of 14 μm. This provides a homogeneous generation of charge carriers through the bulk of the film. The range of electric fields used in these measurements was limited by the bandwidth of the function generator.

XPM apparatus

The sample was placed in the shielded Aluminum box with a 2-mm thick lead collimator. A negative DC bias was applied to the ITO from a high voltage power supply (Stanford Research Systems PS350), and the photocurrent was readout from the Au electrode on oscilloscope Tektronix TDS 2024C with input resistance of 1 MΩ. The X-ray tube (Dunlee PX1412CS, insert DU-304) with a Tungsten target and a 2-mm Al filter was used to generate 60 kVp X-ray pulse (tube current was 200 mA). A chopper controller (Stanford Research Systems SR540) drives a 2-mm thick Copper chopper to modulate an X-ray pulse at different frequencies and 50/50 duty cycle that was used to simulate a pulsed irradiation mode.

References

[1] Kasap, S. et al. Amorphous selenium and its alloys from early xeroradiography to high resolution X-ray image detectors and ultrasensitive imaging tubes. *Phys. Stat. Sol. (B)* **246**, 1794–1805 (2009).

[2] Liu, Y. et al. Electrical properties of x-ray detector based on bismuth tri-iodide single crystal with electrode configuration considering. *Mater. Res. Express* **6**, 055902 (2019).

[3] Sun, H. et al. Laser-induced surface recrystallization of polycrystalline PbI_2 thick films for X-ray detector application. *Appl. Surf. Sci*. **427**, 1146–1151 (2018).

[4] Condeles, J. F. & Mulato, M. Polycrystalline lead iodide films produced by solution evaporation and tested in the mammography X-ray energy range. *J. Phys. Chem. Solids* **89**, 39–44 (2016).

[5] Lee, D., Lee, K. & Seo, J. High signal-to-noise ratio HgI_2 X-ray detector assisted with ultraviolet radiation. *Nucl. Inst. Meth. Phys. Res. (A)* **941**, 162364 (2019).

[6] Antonuk, L. E., El-Mohri, Y., Zhao, Q. & Jiang, H. Exploration of strategies for implementation of screen-printed mercuric iodide converters in direct detection AMFPIs for digital breast tomosynthesis. *Med. Imaging 2017: Phys. Med. Imaging*, **101320A** (2017).

[7] Street, R. A. et al. Comparison of PbI_2 and HgI_2 for direct detection active matrix x-ray image sensors. *J. Appl. Phys*. **91** (5), 3345–3355 (2002).

[8] Zhou, L. et al. A high-resistivity ZnO film-based photoconductive X-ray detector. *IEEE Photon. Technol. Lett.* **31** (5), 365–368 (2019).

[9] Lee, S. et al. Direct thermal growth of large scale Cl-doped CdTe film for low voltage high resolution X-ray image sensor. *Sci. Rep*. **8**:14810, (2018).

[10] Znamenshchykov, Y. V. et al. Electrical, structural and optical properties of $Cd_{1-x}Zn_xTe$ thick polycrystalline films. *Vacuum* **149**, 270–278 (2018).

[11] Simon, M. et al. Analysis of lead oxide (PbO) layers for direct conversion X-ray detection. *IEEE Trans. Nucl. Sci.* **52** (5), 2035–2040 (2005).

[12] Rowlands, J. A. Medical Imaging. Material change for X-ray detectors. *Nature* **550**, 47–48 (2017).

[13] Semeniuk, O. et al. Characterization of polycrystalline lead oxide for application in direct conversion X-ray detectors. *Sci. Rep*. **7**:8659, (2017).

[14] Simon, M. et al. PbO as direct conversion x-ray detector material. *Med. Imaging 2004: Phys. Med. Imaging* **5368**, 188–199 (2004).

[15] Semeniuk, O., Sukhovatkin, V. & Reznik, A. Amorphous lead oxide based energy detection devices and methods of manufacture thereof. *U.S. Patent* 10,163,9701 B2 (2018).

[16] Semeniuk, O., Grynko, O., Juska, G. & Reznik, A. Amorphous lead oxide (a-PbO): Suppression of signal lag via engineering of the layer structure. *Sci. Rep*. **7**:13272 (2017).

[17] Polischuk, B. T. & A. Jean. Multilayer plate for X-ray imaging and method of producing same. *U.S. Patent* 5,880,472 (1999).

[18] Rougeot, H. M., Jean, A., Mani, H. & Shukri, Z. A. Indirect X-ray image detector for radiology. *U.S. Patent* 7,692,157 B2 (2010).

[19] Frey, J. B., Belev, G., Tousignant, O., Mani, H. & Kasap, S. O. Dark current in multilayer stabilized amorphous selenium X-ray photoconductors. *Phys. Stat. Sol. (C)* **6** (S1), S251–S254 (2009).

[20] Frey, J. B. et al. Dark current in multilayer stabilized amorphous selenium based photoconductive X-ray detectors. *J. Appl. Phys*. **112**, 014502 (2012).

[21] Manouchehri, F., Kabir, M. Z., Tousignant, O., Mani, H. & Devabhaktuni, V. K. Time and exposure dependent x-ray sensitivity in multilayer amorphous selenium detectors. *J. Phys. D: Appl. Phys.* **41**, 235106 (2008).

[22] Brauers, A. et al. Charge collection in a Se photoconductor on a thin film transistor array during X-ray imaging. *Mat. Res. Soc. Symp. Proc*. **467**, 919–924 (1997).

[23] Huang, H. & Abbaszadeh, S. Recent developments of amorphous selenium-based X-ray detectors: A review. *IEEE Sens. J.* **20**, 1694–1704 (2020).

[24] Imai, S. Radiation image detector. *U.S. Patent* 7,834,324 B2 (2010).

[25] Tanioka, K. et al. An avalanche-mode amorphous Selenium photoconductive layer for use as a camera tube target. *IEEE Electr. Device L.* **8**, 392–394 (1987).

[26] Irisawa, K., Noda, K., Hayashi, K., Yamane, K. & Miyake, K. Radiation detector. *U.S. Patent* 7,947,970 B2 (2011).

[27] Fender, W. D., Zanrosso, E. M., Leiga, A. G. & Manchego, R. Process for manufacturing an improved selenium alloy x-ray imaging member on transparent substrate. *U.S. Patent* 5,320,927 (1994).

[28] Fender, W. D., Speiser, R. C., Kramer, G. K. & Ceelen, H. P. Selenium alloy imaging member. *U.S. Patent* 4,770,965 (1988).

[29] Cheung, L., Bogdanovich, S., Ingal, E. & Williams, C. L. Amorphous selenium flat panel X-ray imager for tomosynthesis and static imaging. *U.S. Patent* 7,304,308 B2 (2007).

[30] Belev, G. S. Electrical properties of amorphous selenium based photoconductive devices for application in X-ray image detectors. *Ph.D. dissertation*, University of Saskatchewan, Saskatoon, SK, Canada (2007).

[31] Semeniuk, O., Csik, A., Kökényesi, S. & Reznik, A. Ion-assisted deposition of amorphous PbO layers. *J. Mat. Sci*. **52**, 7937–7946 (2017).

[32] Semeniuk, O. et al. Charge transport mechanism in lead oxide revealed by CELIV technique. *Sci. Rep.* **6**:33359, (2016).

[33] Juška, G., Arlauskas, K. & Genevičius K. Charge carrier transport and recombination in disordered materials. *Lith. J. Phys*. **56**, 182–189 (2016).

[34] Semeniuk, O. et al. Transport of electrons in lead oxide studied by CELIV technique. *J. Phys. D: Appl. Phys*. **50,** 035103 (2017).

[35] Kasap, S., Koughia, C., Berashevich, J., Johanson, R. & Reznik, A. Charge transport in pure and stabilized amorphous selenium: re-examination of the density of states distribution in the mobility gap and the role of defects. *J. Mat. Sci.: Mat. Electron*. **26**, 4644–4658 (2015).

[36] Abbaszadeh, S., Scott, C. C., Bubon, O., Reznik, A. & Karim, K. S. Enhanced detection efficiency of direct conversion x-ray detector using polyimide as hole-blocking layer. *Sci. Rep*. **3**:3360, (2013).

[37] Kruger, R. A. et al. Computerized fluoroscopy in real time for noninvasive visualization of the cardiovascular system. *Radiology*, **130** (1), 49–57 (1979).

[38] Kasap, S. et al. Amorphous and polycrystalline photoconductors for direct conversion flat panel x-ray image sensors. *Sensors* **11**, 5112–5157 (2011).

[39] Camlica, A. et al. Use of pulse-height spectroscopy to characterize the hole conduction mechanism of a polyimide blocking layer used in amorphous-selenium radiation detectors. *IEEE Trans. Electron Devices* **67**, 633–639 (2020).

[40] Biberman, L. M. & Nudelman, S. The Plumbicon in *Photoelectronic Imaging Devices, Vol. 2 Devices and Their Evaluation* (eds Stupp, E. H., Levitt, R. S.) 275–300 (Plenum, 1971).

Acknowledgements

Financial support from Teledyne DALSA, the Natural Sciences and Engineering Research Council of Canada (NSERC) and Mitacs Accelerate programs is gratefully acknowledged.

Author contributions

O.G. deposited experimental bilayer PbO sample, performed CELIV experiment and drafted the manuscript text. T.T. and E.P. performed XPM experiment. G.J. and A.R. examined and analyzed the obtained results. A.R. edited the manuscript text. All authors reviewed the manuscript.

Competing interests

The authors declare no competing interests.

Data availability

The datasets generated and analysed during the current study are available from the corresponding author on reasonable request.

Received: 23 June 2020; **Accepted**: 2 November 2020; **Published online**: 18 November 2020

Chapter 4

PI/a-PbO detector with blocking layer structure

This topic has been elaborated in the following publication:

Oleksandr Grynko, Tristen Thibault, Emma Pineau, Alla Reznik. Engineering of a Blocking Layer Structure for Low-Lag Operation of the a-PbO-Based X-Ray Detector. *IEEE Transactions on Electron Devices*, Volume 68, Issue 5, pp. 2335–2341 (2021). DOI: 10.1109/TED.2021.3067616.

The full text of the publication is listed below.

Engineering of a Blocking Layer Structure for Low-Lag Operation of the a-PbO Based X-ray Detector

Oleksandr Grynko, *Student Member, IEEE*, Tristen Thibault, Emma Pineau, Alla Reznik

O. Grynko is with the Chemistry and Materials Science Program, Lakehead University, Thunder Bay, ON, P7B 5E1, Canada (e-mail: ogrynko@lakeheadu.ca).

T. Thibault and E. Pineau are with the Physics Department, Lakehead University, Thunder Bay, ON, P7B 5E1, Canada (e-mails: ttthibau@lakeheadu.ca, enpineau@lakeheadu.ca).

A. Reznik is with the Physics Department, Lakehead University, Thunder Bay, ON, P7B 5E1, Canada and Thunder Bay Regional Health Research Institute, Thunder Bay, ON, P7B 6V4, Canada (e-mail: areznik@lakeheadu.ca).

Abstract—Direct conversion flat panel detectors are of great significance to the field of radiation medical imaging since they offer imaging performance and diagnostic capabilities not achievable with other methods. Currently, mammographic direct conversion detectors employ a layer of amorphous Selenium (a-Se) photoconductor. Although its properties ideally fit the requirements of mammography, where "soft" X-rays are used, a-Se cannot be used in high-energy X-ray procedures. To extend the diagnostic capabilities of the direct conversion detectors, Amorphous Lead Oxide (a-PbO) is proposed as an alternative photoconductor. It is a high effective atomic number material and thus has higher X-ray stopping power over the wide X-ray energy range. a-PbO is, therefore, a suitable candidate for applications in radiography, fluoroscopy, and digital tomosynthesis. Here we report on the development of a blocking structure with a polyimide (PI) layer needed to maintain low dark current at high electric fields. We demonstrate that a 1 μm thick PI blocking layer allows the operation of the detector at strong electric fields (≥10 V/μm) while suppressing the dark current to an innocuous level (<1 pA/mm^2). It also improves temporal performance by reducing signal lag. No ghosting effect was observed at exposure rates up to 1 R/s, however, at high radiation levels, the detector's sensitivity degrades. This degradation is not permanent as the detector restores its original sensitivity after several hours of rest in the dark without bias applied.

Index Terms—Lead Oxide, Polyimide, X-ray detectors, direct conversion, blocking layer

I. Introduction

The most common and important application of fluoroscopic X-ray imaging today is in image-guided diagnostic and therapeutic procedures where real-time (30 frames per second) image sequences are used to guide the interventional radiologist's mind and hand. Current state-of-the-art X-ray imaging technology for diagnostic X-ray energies is based on an indirect conversion method where a scintillator (e.g., CsI or Gd_2O_2S) first converts X-ray quanta into optical photons, which in turn diffuse through a phosphor and then are converted to electrons by an array of photodiodes [1]. This two-step conversion process reduces the X-ray–to–charge conversion gain and as a result, these detectors are quantum limited, so the signal-to-noise ratio (SNR) for a given pixel is proportional to the square root of the number of detected X-rays. Subsequently at the lowest exposure levels common in fluoroscopy (0.1–1 μR/frame) electronic noise dominates over the quantum noise and therefore, visibility of low contrast objects is compromised. In addition, the omnidirectional propagation of optical photons in the scintillator reduces the spatial resolution of the indirect conversion detectors [2], [3].

These issues can be overcome by the use of the direct conversion approach. "Direct conversion" means that X-rays are absorbed in a photoconductor that directly creates electron-hole pairs, which are subsequently separated by an applied electric field to generate a recordable signal [4], [5]. The charges are moved by a field making it possible to create an image with a thick detector layer without significant loss of resolution. Commercial direct conversion Flat Panel X-ray Imagers (FPXIs) are used in breast imaging, i.e., in mammography energy range, where they demonstrate superior image quality in comparison with the indirect conversion scheme [5], [6].

Two major components of FPXIs are a large area thin-film transistor (TFT) or complementary metal-oxide-semiconductor (CMOS) active-matrix array [7] (as used in flat panel displays, for example) and a photoconductive layer which is deposited directly onto the imaging array and acts as an X-ray–to–charge transducer. Currently, commercial FPXIs employ a layer of stabilized amorphous selenium (a-Se) photoconductor. Due to the low atomic number ($Z = 34$) of Selenium, a-Se–based detectors are efficient only for low-energy X-rays used in mammography. To extend

the diagnostic capabilities of the direct conversion detectors over radiographic, fluoroscopic, and digital breast tomosynthesis (DBT) energy range, a-Se has to be replaced with high-*Z*, wide-bandgap X-ray photoconductive material. In addition, for real-time applications, an X-ray photoconductor has to demonstrate an adequate temporal performance in terms of signal lag (i.e., a post-signal after X-ray irradiation): the lag should not exceed that of the scintillators. This is a strict requirement, since in state-of-the-art indirect conversion detectors lag is imperceptible. Indeed, the CsI-based detector with an a-Si TFT imager designed for cardiac imaging demonstrated the first frame lag of 2% (30 fps readout) [8]. An indirect detector with a Gd_2O_2S scintillator and a-Si:H TFT array showed a 2% lag after the lowest frame time of 0.2 s [9]. A more prominent example of the indirect conversion detector utilizes an advanced imaging array based on the CMOS technology and demonstrates the first frame lag below 0.1% at 30 fps [10].

Several photoconductors have been intensively investigated for this role during the last two decades, but large signal lag deemed them unapplicable for further consideration as X-ray–to–charge transducers in dynamic X-ray imaging: poly-PbI_2 (first frame lag ~30-50% [11], [12]), poly-HgI_2 (first frame lag ~10–20% [11]–[13]), poly-CdTe (lag at the first frame ~6–20% [14], [15] and ~30% after 0.5 s for the detector with CMOS imager [16]), poly-CdZnTe (first frame lag ~6–70% [17], [18]), and poly-PbO (1.5–7% lag after 1 s [19], [20]). Another candidate for the X-ray–to–charge transducer in direct conversion detectors are perovskites, a new family of emerging materials. Although promising, at least at the very early stage of their development, perovskites also demonstrate large signal lag [21]. If this problem will not be solved, all the efforts in the development of perovskite technology will come to naught.

So far, the only direct conversion detectors that could be considered for dynamic imaging are based on a-Se photoconductor. Indeed, although the main application of a-Se–based detectors was in static mammographic imaging, its performance was also evaluated for real-time applications in dynamic imaging, such as fluoroscopy and digital subtraction angiography (DSA). It typically exhibited a first frame lag at 30 fps of 2–6% [14], [22], [23], but faster response (lag <1%) was also reported [24]–[26].

One of the possible alternatives to a-Se with nearly lag-free operation is amorphous Lead Oxide (a-PbO) [27], [28]. It is a photoconductive material with a fast response, a potentially higher charge yield, high effective atomic number ($Z_{eff} \approx 79$), and higher X-ray stopping power over a wide

energy range [27], [28]. Indeed, for energies relevant to radiation medical imaging, the attenuation coefficient for a-PbO ranges from 704 cm^{-1} at 20 keV to 20 cm^{-1} at 140 keV, in comparison to 210 cm^{-1} and 1.3 cm^{-1} for a-Se for the same energies, respectively [29]. Since a-PbO is proposed as a substitute for a-Se in X-ray digital detectors with high dynamic range, an urgent problem arises to minimize the dark current and to develop an a-PbO blocking layer structure, similar to how it was achieved in a-Se.

The need for blocking structures arises from the strong electric field applied to the X-ray–to–charge transducer during detector operation. Typically, a field of 10 V/μm or higher must be applied to a photoconductor to achieve an acceptable charge collection efficiency. If preventive measures are not taken, the application of such a high electric field leads to the excessive injection of the charge carriers from the contacts into the photoconductor, causing a high dark current, subsequent deterioration of the SNR, and degradation of the visibility of low contrast objects at low exposures. In addition, the dark carriers may be trapped in the bulk of the photoconductor, thus modifying the internal electric field and affecting the photogeneration efficiency across the layer. An acceptable dark current density for X-ray detectors should preferably not exceed 1–10 pA/mm^2, depending on the clinical application [5].

Since the thermal generation of carriers in wide bandgap photoconductors used in imaging detectors is typically very small, the main source of dark current is attributed to an injection of carriers from the electrodes [30]. A practical approach to minimize the injection and to reduce the dark current to an acceptable level, is to introduce thin blocking layers between the photoconductor and the electrodes [31], [32].

In a-Se–based detectors, these blocking layers (with thicknesses much smaller than the photoconductor thickness) are made from specially alloyed and doped a-Se. The doping is designed to cause deep trapping of carriers injected from the adjacent electrodes but at the same time to allow the opposite sign carrier to be transported. By analogy with semiconductors, hole and electron blocking layers are called *n*-like and *p*-like layers, respectively. The dark current in such multilayer a-Se photoconductors is about 3 orders of magnitude smaller than that in a single a-Se layer with the same thickness and applied field [32].

An alternative approach to prevent injection is to use blocking layers made of a semi-insulating polymer, like cellulose acetate (CA) [33] or Polyimide (PI) [24]. It was previously shown that both

CA and PI polymers are compatible with a-Se technology and can serve as blocking layers in a-Se avalanche structures: CA layer improves stability against dielectric breakdown while the carrier mobilities are not compromised. As for PI, it bonds well to a-Se, it is compatible with a-Se deposition technology, and it enables stable operation at low dark currents without sudden breakdown and associated structural transformations. In addition, PI acts as a soft buffer layer reducing shear strain at the photoconductor-substrate interface and improves adhesion [34]. Similar to *n*-like and *p*-like layers in a-Se blocking structure, these polymers would need to prevent the injection of one type of carriers from the electrode while allowing the collection of the photogenerated carriers of the opposite sign. If the last condition is not met, the carriers will be trapped at the interface causing screening of the electric field and reduction of the detector's charge collection efficiency. Additionally, it can result in the degradation of temporal performance through increased lag and ghosting effect (i.e., change in X-ray sensitivity due to previous irradiation).

Here we report on our approach to a-PbO blocking structures with a thin layer of PI. This polymer layer can be easily and cost-efficiently applied even to large-area substrates using a standard spin-coating technique. Its charge blocking properties can be tuned by varying the thickness of the layer.

Although the use of a PI blocking layer in a-Se avalanche detectors is very encouraging for an application of PI in conjunction with the a-PbO photoconductor, concern remains regarding the possible degradation of temporal performance of a PI/a-PbO detector as often happens if a "foreign" layer is introduced into the structure. However, through investigation of the kinetics of the dark current, signal lag, and ghosting we demonstrate that no deterioration of temporal performance is observed while the dark current is reduced to an innocuous level. The above features make PI a practical approach for the development of a-PbO based X-ray digital detectors with a low dark current for a variety of applications.

II. Methods

A. Sample preparation

PI/a-PbO blocking layer structure is schematically shown in Fig. 1. In this configuration, a thin layer of PI was applied (under controlled parameters like spin speed and duration, curing

temperature and time) to the ITO-coated glass prior to the deposition of the a-PbO layer.

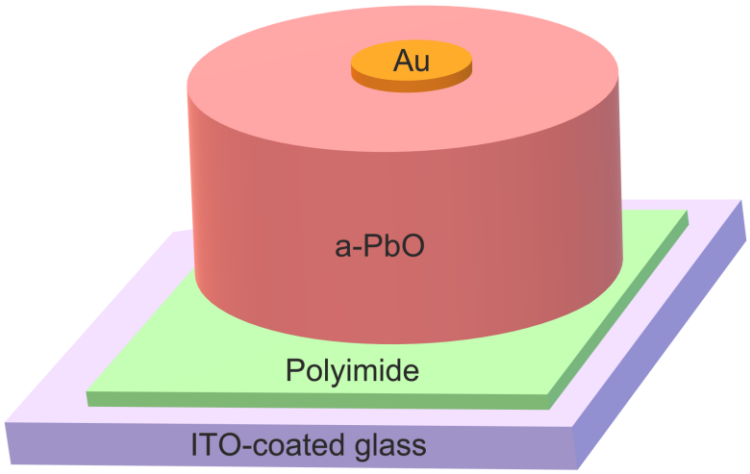

Fig. 1. Schematic of PI/a-PbO blocking structure.

The sample was prepared in a cleanroom environment as follows. Commercially supplied ITO-coated glass was sequentially cleaned with Acetone, Methanol, Isopropanol, and dry Nitrogen, and then placed for 10 minutes on the hot plate heated to 90 °C to remove any remaining solvents. A polyamic acid precursor dissolved in an n-methyl-2-pyrrolidone (NMP) based solvent was dispensed in the center of the stationary substrate. To obtain a 1 μm thick layer of PI, a spin-coating was done in three steps with parameters shown in Table I. At the first step, the substrate is spun at a low speed to allow the precursor to spread across the entire surface of the substrate. After that, a substrate is accelerated to a final speed, which is the main factor in the determination of the resulting PI layer thickness. After spinning, it is decelerated to a static state. The spin duration at the first step and the acceleration at the second step were adjusted to obtain a uniform thickness across the surface. After spin-coating, the substrate was placed on a hot plate, ramped to a high temperature (sufficient for complete dissociation of the NMP solvent carrier and full imidization of the polyimide film) and cured under constant dry Nitrogen flow with parameters shown in Table I.

TABLE I

POLYIMIDE LAYER COATING AND CURING PARAMETERS

Spin-coating			
	Step 1	Step 2	Step 3
Duration, s	5	30	7
Speed, rpm	500	6000	0
Acceleration, rpm per s	550	990	-1100

Curing	
Curing temperature, °C	350
Curing duration, min	30
Heating-cooling rate, °C/min	4
Nitrogen flow, sL/min	2

In order to be able to make an electrical connection to the ITO-side of the substrate, which is essential for electrical and X-ray characterization of the detector described further in the text, the edges of the substrate were masked with a Kapton polyimide tape prior to the spin-coating. The tape was peeled off after the coating.

A 19 μm thick layer of a-PbO was deposited afterwards by the ion-assisted thermal evaporation technique with the following parameters: base pressure ~$5 \cdot 10^{-5}$ Pa, process pressure ~$6 \cdot 10^{-2}$ Pa, furnace temperature ~1000 °C, substrate temperature ~100 °C, deposition rate ~0.2 μm/min, ion energy ~50 eV, ion flux ~0.2 mA/cm^2. A detailed description of the deposition process can be found in [35]. Finally, a gold contact, 20 nm in thickness and 1 mm in diameter, was sputtered atop of the a-PbO in a dedicated chamber.

B. Dark current kinetics measurement

Dark current was measured as a function of time for different bias voltages relevant to the direct conversion detector operation (Fig. 2(a)). The sample was placed in a light-tight shielded box to prevent photogeneration. A positive voltage (Stanford Research Systems PS350 power supply) was applied to the ITO electrode, and the dark current was read out from the Au electrode with Keithley 35617EBS electrometer. A power supply and an electrometer were connected through a

GPIB interface (Tektronix AD007) to a host computer which provided control and data acquisition. A 100 MΩ resistor was connected in parallel to the sample to allow the recovery current to flow in a circuit in between the measurements.

Prior to measurement, the sample was short-circuited in the dark for at least 10 hours to allow complete detrapping of charge carriers. The voltage was ramped at a rate of 5 V/s, and the dark current was read out every second during a 2 h period. After the decay is recorded, the voltage was ramped to zero at the same rate and the detector is left unbiased for 10 h.

C. Temporal performance characterization

The main goal of this work is to investigate the impact of the PI blocking layer on the temporal performance of a-PbO based X-ray detector and to evaluate signal lag and ghosting effects. Signal lag is a residual current after the termination of X-ray irradiation and ghosting is the degradation of the detector's sensitivity as a result of previous irradiation. In order to evaluate the detector's temporal performance in near clinical conditions, it is necessary to irradiate it with a sequence of short X-ray pulses (with a rate up to 30 frames per second (fps)) and to measure the current during the irradiation and with X-rays off.

The characterization was performed using the X-ray induced Photocurrent Method (XPM) in a pulsed mode, where a rotating chopper was used to modulate an X-ray pulse at a variable frequency. The experimental setup is shown in Fig. 2(b). A sample is placed in the shielded Aluminum box. Prior to measurement, the sample was short-circuited in the dark for at least 2 hours to allow complete detrapping of charge carriers. A positive dc bias was applied to the ITO from a high voltage power supply (Stanford Research Systems PS350), and the photocurrent was readout from the Au electrode on an oscilloscope (Tektronix TDS 2024C) with 1 MΩ native input resistance. A bias was applied to the sample for 10 minutes prior to irradiation to allow the dark current to stabilize and to drop to a level below 5 pA/mm^2. The X-ray tube (Dunlee PX1412CS, insert DU-304) with a Tungsten target was used to generate 1-s long 60 kVp X-ray pulses. At this energy and thickness of the sample, the detector has an absorption efficiency of 25%. A 1.3-mm Al filter was used to attenuate low-energy photons and minimize Compton backscattering noise, and a 2-mm Lead collimator was used to prevent stray scattering. The exposure was monitored by the Keithley 96035 ionization chamber; attenuation by a glass substrate and a chopper was considered when calculating total incident on the detector exposure. A chopper controller

(Stanford Research Systems SR540) drives a 2-mm thick Copper chopper with an adjustable frequency and a 50% duty cycle.

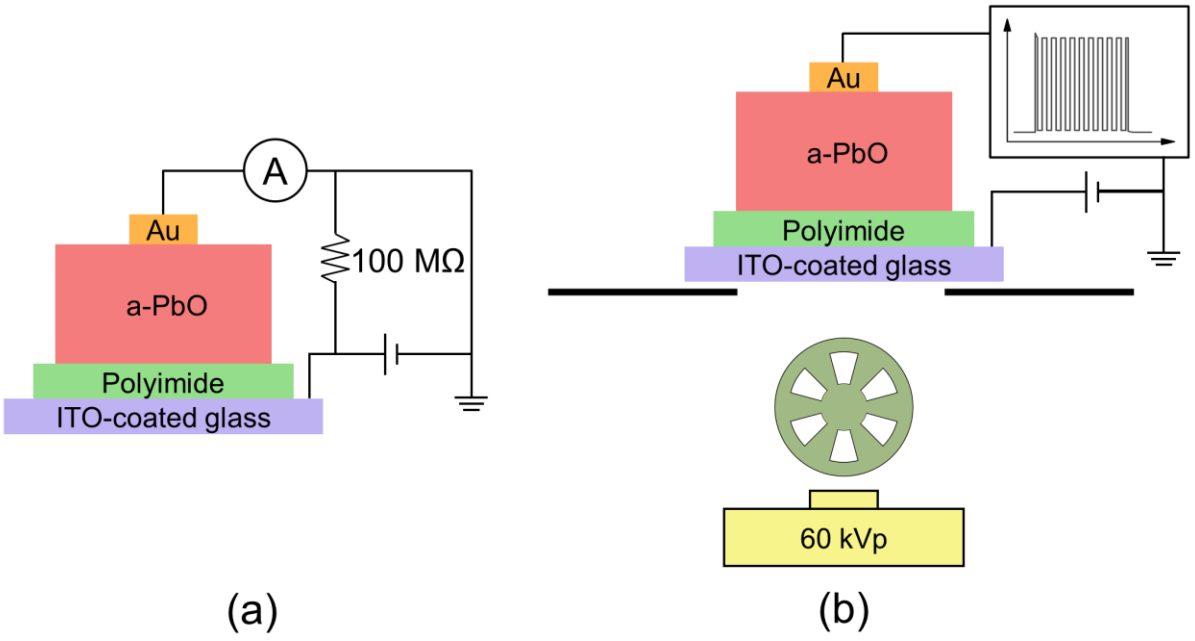

Fig. 2. Schematic experimental setup for (a) dark current kinetics measurement and (b) temporal performance characterization.

D. Lag and ghosting measurements

To evaluate lag and ghosting, the sample was irradiated with a train of 1-s long X-ray pulses modulated at a frequency of 5–30 Hz. 20 pulses were fired with an interval of 60 s, as shown in Fig. 3(a) (interval time was limited by the risk of overheating the X-ray tube).

A typical response to a continuous and modulated X-ray pulse is shown in Fig. 3(b). The photocurrents with X-rays on (PC_{on}) and off (PC_{off}) for every frame as well as the dark current prior to irradiation (DC) were recorded for each pulse. The first and the last frames were omitted due to asynchronization of the X-ray pulse and the chopper, and the initial overshoot in the X-ray pulse.

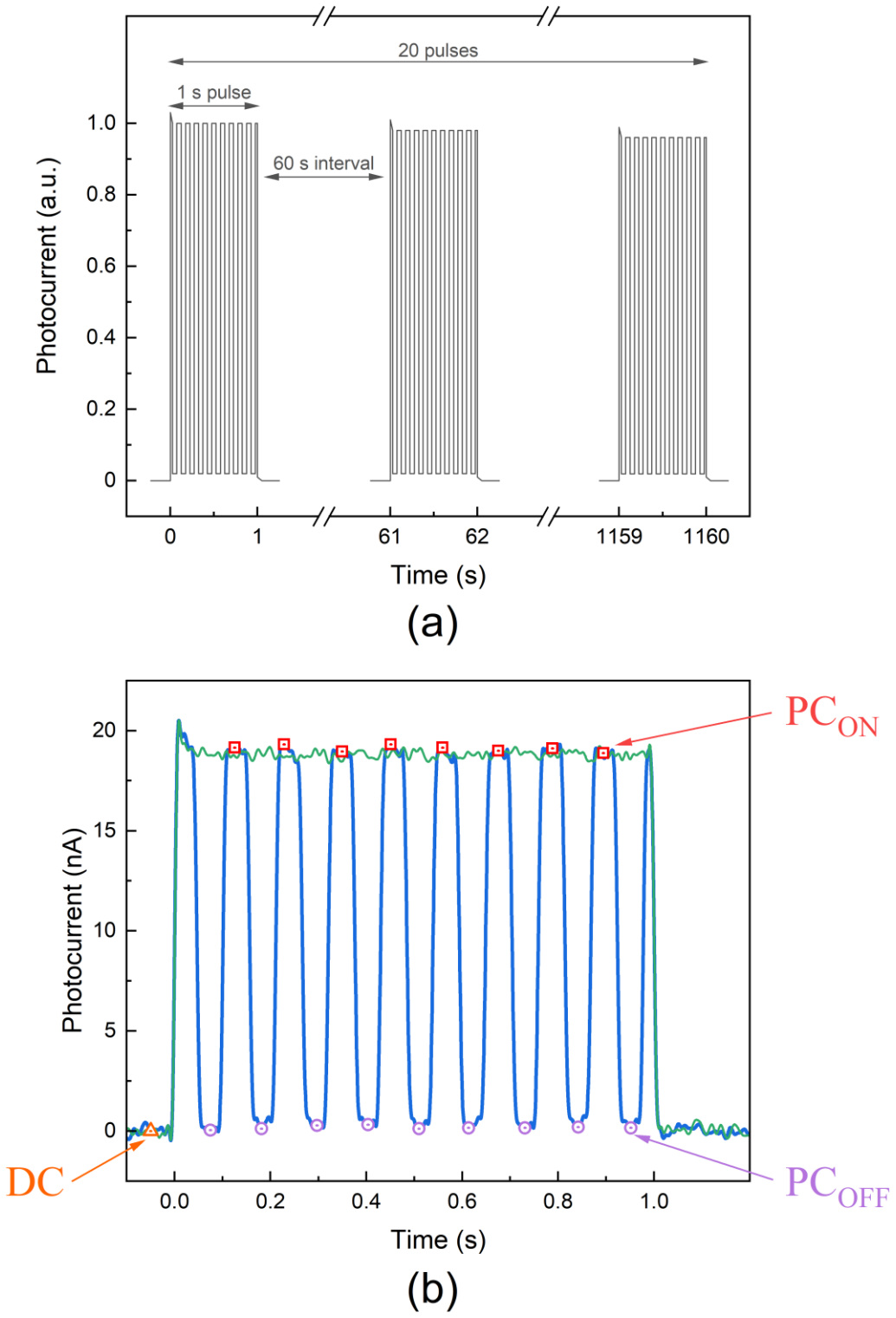

Fig. 3. (a) A sequence of modulated X-ray pulses used for temporal performance characterization. (b) Typical X-ray response to a continuous and modulated irradiation, and measured values within each pulse. *Note: Fig. 3(a) was not included in the original publication.*

Detector's sensitivity (S) is defined as the amplitude of the photocurrent during the irradiation (PC_{on}), corrected for the dark current (DC). The average values of the photo- and dark currents were used for each pulse. Signal lag (Lag) is quantified as a ratio of the photocurrent after the irradiation (when a chopper blade blocks X-rays, PC_{off}) to the detector's sensitivity. The ghosting effect can be quantified as a relative sensitivity – a ratio of the sensitivity at given pulse to the initial sensitivity of a well-rested detector. Sensitivity and lag values were calculated for each pulse n as:

$$S_n = \langle PC_{on} \rangle_n - DC_n \,, \tag{1}$$

$$Lag_n = \frac{\langle PC_{off} \rangle_n - DC_n}{S_n} \,. \tag{2}$$

III. Results and Discussion

A. Dark current kinetics measurement

Fig. 4 shows the decay of the dark current over time at different electric fields (5–20 V/μm). After a bias is applied, the current rapidly decays with time, reducing by nearly 2 orders of magnitude. At 10 V/μm, it drops from 30 pA/mm^2 to 0.2 pA/mm^2 within two hours. However, the dark current increases with the electric field: 0.1 pA/mm^2 at 5 V/μm and 0.7 pA/mm^2 at 20 V/μm after biasing for 2 hours.

This behaviour is similar to what has been observed in a-Se–based *n-i*, *i-p*, *n-i-p* blocking structures (where *i*-layer is stabilized a-Se), and in PI/a-Se: the dark current rapidly decreases with time by 1–3 orders of magnitude (depending on the layer configuration) over several hours. The lowest attainable steady-state dark current was achieved in *n-i-p* and PI/a-Se detectors: 0.01–0.05 pA/mm^2 at 10 V/μm [36], [37]. This minimal dark current was attributed to the bulk thermal generation in the PI/a-Se detector, but in the *n-i-p* detector, it was assigned to the electron injection [38] or balancing of the carrier trapping and detrapping rates due to Schottky emission over the barrier in *n*-layer [39]. Either way, the steady-state dark current in a-Se blocking structures is well below the tolerable level for detector applications of 1 pA/mm^2.

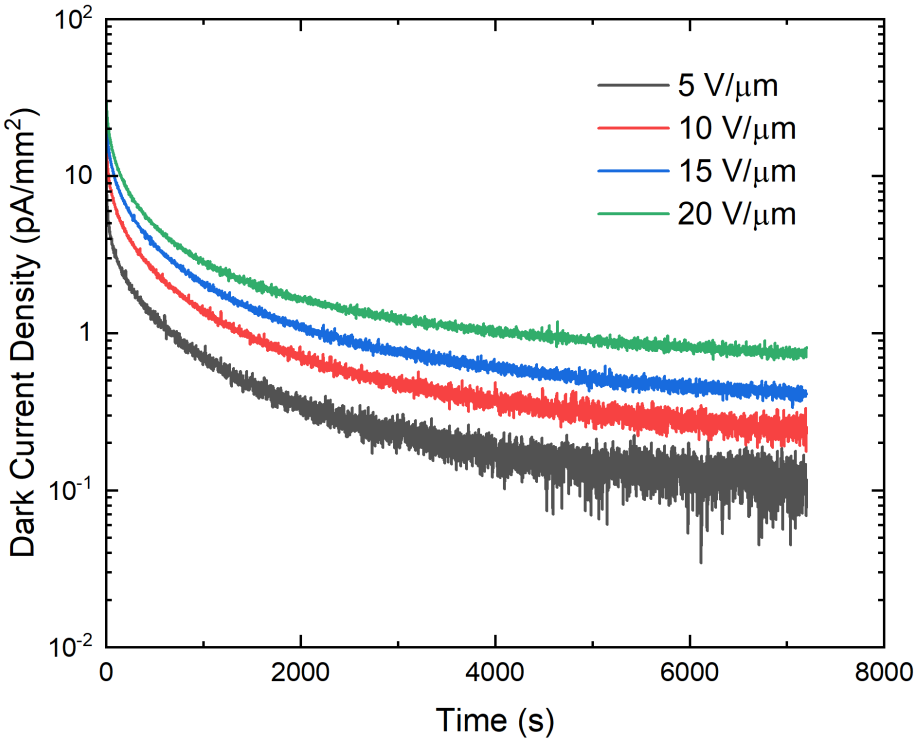

Fig. 4. Kinetics of dark current density at different electric fields.

Although further investigation of the dark current kinetics in PI/a-PbO is needed, it can be qualitatively explained in the following model. There are two main sources of the dark current: thermal generation in the bulk of the photoconductor and carrier injection from the electrodes. As PbO has a wide bandgap (~1.9 eV [5]), the bulk thermal generation is relatively small, thus carrier injection is dominant. After the positive bias is applied to the ITO, holes (major carriers in PbO [40]) are injected from the ITO into the PI layer and are accumulated at the ITO/PI interface. This causes screening of the electric field, suppressing further injection, and hence the dark current. After the hole injection is reduced, the electron injection from the negative Au electrode and the thermal generation in the bulk of a-PbO take dominant effect.

In a PI/a-PbO detector, the dark current has not reached a steady state after two hours, meaning that it is not completely suppressed yet. This gives a potential for further dark current reduction. Depending on the mechanism responsible for the final decaying portion of the dark current, it can be achieved by waiting for a longer time (a warm-up period of the detector), or by introducing a second blocking layer into the structure that would prevent injection of electrons. However, even in the current configuration, an acceptable dark current level of 1 pA/mm^2 can be easily achieved.

B. Temporal performance

When the detector is exposed to a continuous irradiation (Fig. 3(b)), it exhibits a quasi-rectangular response with a constant amplitude and low (<1%) lag. A small overshoot at the beginning of the pulse is a characteristic feature of the X-ray tube, not the detector, since a similar response was observed in the silicon photodiode used to trigger the oscilloscope. A uniform amplitude indicates that the dark current is constant and the photocurrent neither builds-up due to X-ray triggered injection (as observed, for example, in poly-PbO and early PI/a-Se detectors [20], [24]), nor decreases due to degradation of the internal electric field caused by the accumulation of X-ray–generated charge at the PI/a-PbO interface. Moreover, when the detector is exposed to a modulated irradiation, both the photocurrent during each frame and the amplitude in successive frames remain constant. This indicates the unhindered flow of photogenerated electrons from the photoconductor through the PI layer to the ITO electrode. Indeed, if an accumulation of photogenerated electrons at the interface would occur, a decrease in photocurrent at the end of each frame would be observed [37]. In [37], a small decrease in the photocurrent during each frame was attributed to a temporary change in the internal electric field, which is restored by hole injection from the anode, keeping the same amplitude of consecutive pulses. Therefore, our analysis of the X-ray response of the PI/a-PbO detector to a continuous and modulated irradiation suggests that the presence of the PI layer does not affect charge collection efficiency. This conclusion, together with a suggested mechanism responsible for the dark current kinetics (accumulation of the injected holes from the ITO and screening of the electric field) demonstrates that the PI layer indeed acts as a blocking layer, rather than an insulator.

Fig. 5 shows signal lag values for the PI/a-PbO detector calculated using (2) for various electric fields (5–20 V/μm), modulation frequencies (5–30 Hz), and incident exposures (1–4 R). Signal lag was found to be nearly constant at each pulse (at fixed field, frequency, and exposure), therefore, the values shown have been averaged over 20 pulses.

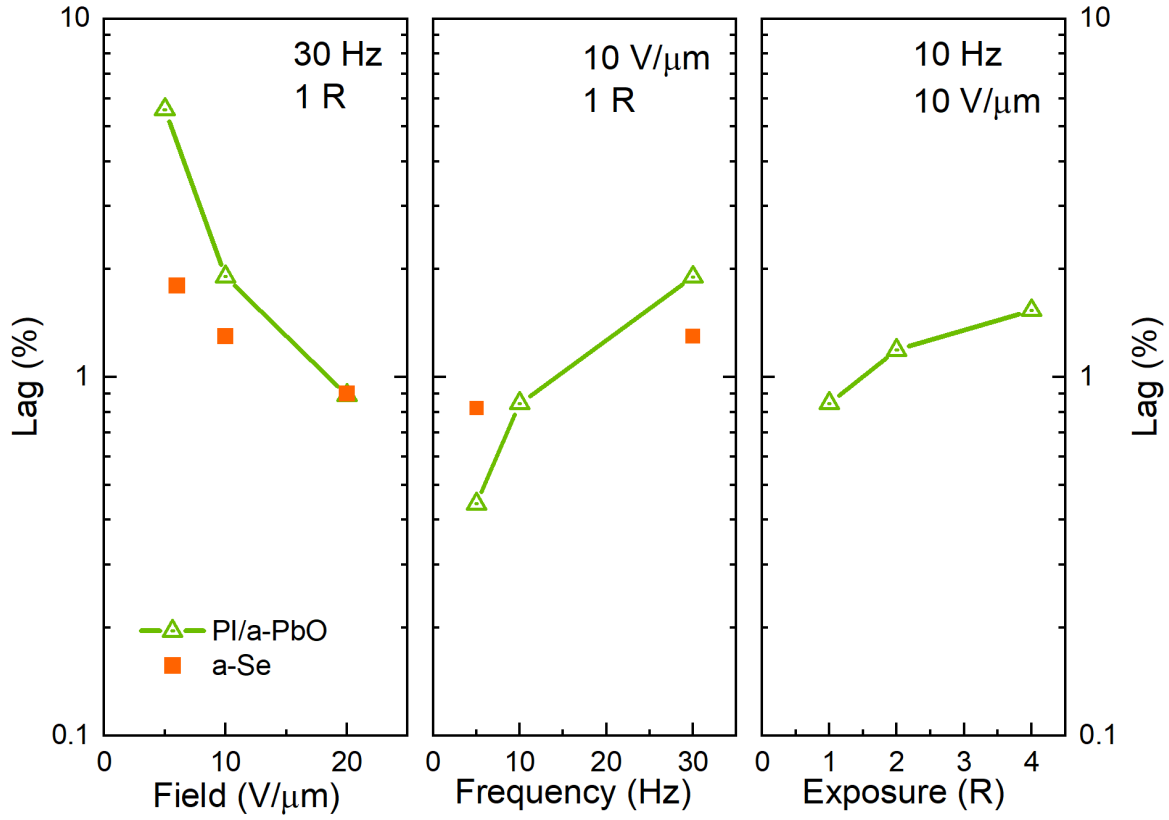

Fig. 5. Signal lag measured as a function of the electric field, modulation frequency and incident exposures in a PI/a-PbO detector. A dataset was connected with lines as a guide for the eyes. For an a-Se–based detector, lag values were extracted from the literature.

The application of a stronger electric field improves temporal performance and reduces signal lag. Its value decreases with field: 5.6% at 5 V/µm down to 0.9% at 20 V/µm (with a frequency fixed at 30 Hz). In contrast, lag increases at higher modulation frequencies and reaches 1.9% at 30 Hz and 10 V/µm. Incident exposure has little effect on the lag in the range investigated, which demonstrates the stability of the X-ray response at different exposure levels. It should be noted that the detector investigated here absorbs only 25% of the incident X-rays under given beam conditions, thus the *absorbed* dose by the photoconductor is the only ¼ of the *incident* dose.

To compare the temporal performance of a PI/a-PbO detector with an a-Se based detector, lag values were extracted from [24] and [25] (at the most advantageous bias polarity) and plotted on the same graph. In these works, lag in a-Se was measured with the same technique and under similar conditions (electric field, modulation frequency, exposure, interval between pulses),

however, the X-ray tube voltage was 28–32 kVp (in contrast to 60 kVp in this work). A blocking layer structure was also used in both a-Se detectors: a PI layer between the photoconductor and the substrate in [24] and two undisclosed blocking layers in [25]. Although a-Se detector mostly demonstrates a slightly faster response than PI/a-PbO (1.3% and 1.9% lag, respectively, at 10 V/μm, 30 Hz, and 1 R), at the higher field they have similar performance.

PI/a-PbO detector exhibits a remarkable improvement of temporal performance over other photoconductors considered for use in the direct conversion digital detectors (such as polycrystalline layers of PbO, PbI_2, HgI_2, CdTe, CdZeTe, and perovskites) [11–21] and marginal signal lag with a-Se [24]– [26], [37] and CsI [8], [10]. So far, a-PbO and a-Se are the only photoconductors where the lag problem was resolved. Combine with the high absorption efficiency of PbO in the diagnostic X-ray energy range and the low dark current of the blocking structure, the PI/a-PbO detector becomes the most favorable candidate for application in the real-time diagnostic imaging.

Degradation of sensitivity for different incident exposure levels is shown in Fig. 6. At the lower exposure rate, sensitivity remains nearly constant showing no ghosting effect. However, at the elevated radiation level, the detector's sensitivity drops with each subsequent pulse. For 4 R/s exposure, sensitivity decreases by 9% after 20 pulses (an accumulated exposure of 80 R). Note that it is not a permanent degradation of the detector; it restores its initial sensitivity after resting unbiased in a dark for a few hours. To compare, the a-Se detector had a 10% degradation of sensitivity after 20 R of a cumulative exposure [24] and 15% after 60 R of a cumulative exposure [25].

It should be noted that X-ray doses used here are much larger than those used in the clinical practice [41], [42], and thus represent operation under extreme load. Indeed, typical exposures to the patient in the dynamic imaging are 0.1–1 R for DBT (accumulated from multiple, usually 9–25, projections over less than 10 s period). For fluoroscopic imaging in surgery, exposure of some Roentgens can be accumulated over a period of up to a few hours. These values of exposure in the patient plane are equivalent to the incident on the detector exposure outside the patient (typically at the periphery of the detector); behind the patient, the exposure would be 10–100 times smaller.

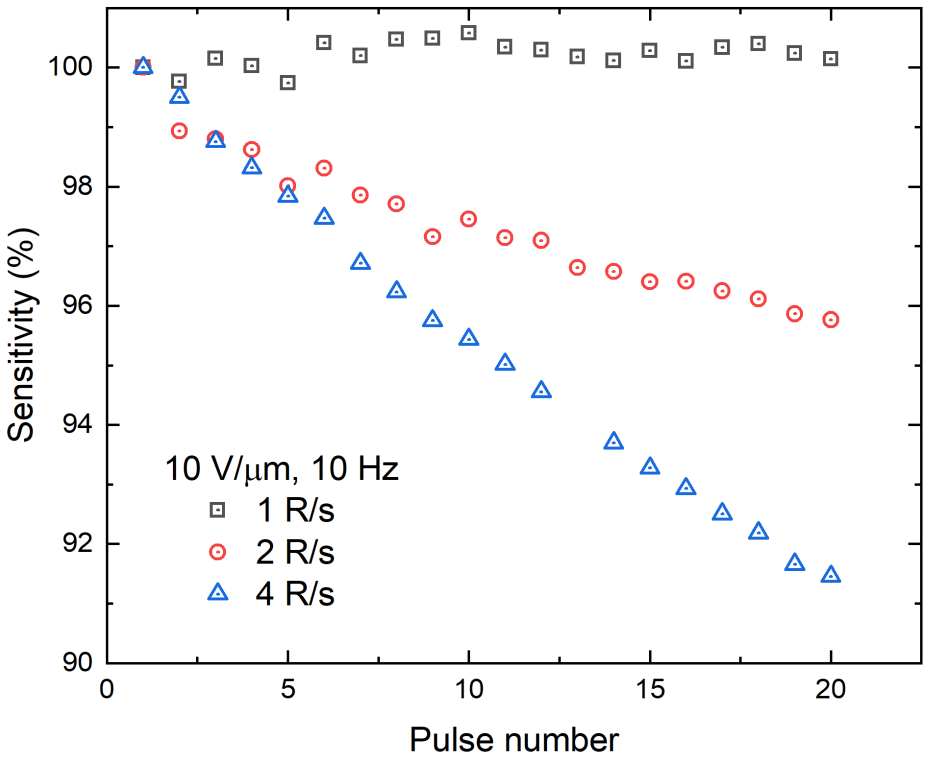

Fig. 6. Degradation of the detector's sensitivity (ghosting) with consecutive pulses at different incident exposure rates.

IV. Conclusion

A direct conversion X-ray detector based on the amorphous Lead Oxide photoconductor with a single blocking layer of polyimide was developed and evaluated. The application process of the PI blocking layer is simple, cost-efficient, and compatible with large-area fabrication. A PI/a-PbO detector satisfies requirements for low dark current (<1 pA/mm^2) at electric fields as high as 20 V/μm. The detector demonstrates temporal performance suitable for real-time imaging with lag values down to 0.9% at 30 Hz. The detector's response remains constant at a low exposure rate (< 1 R/s), but at a high radiation level, the sensitivity degrades. Overall, our approach to use a PI blocking layer in a-PbO–based detector permits the application of a higher electric field for enhanced charge collection and sensitivity while maintaining suitable temporal and dynamic properties in various clinical and industrial X-ray imaging applications.

References

[1] W. Zhao, G. Ristic, and J. A. Rowlands, "X-ray imaging performance of structured cesium iodide scintillators," *Med. Phys.*, vol. 31, no. 9, pp. 2594–2605, Aug. 2004, DOI: 10.1118/1.1782676.

[2] M. Simon, K.-J. Engel, B. Menser, X. Badel, and J. Linnros, "Challenges of pixelated scintillators in medical X-ray imaging," *Nucl. Instr. Meth. Phys. Res. Sect. A Accel. Spectrometers, Detect. Assoc. Equip.*, vol. 591, no. 1, pp. 291–295, Jun. 2008, DOI: 10.1016/j.nima.2008.03.077.

[3] A. Datta, Z. Zhong, and S. Motakef, "A new generation of direct X-ray detectors for medical and synchrotron imaging applications," *Sci. Rep.*, vol. 10, no. 1, p. 20097, Nov. 2020, DOI: 10.1038/s41598-020-76647-5

[4] S. O. Kasap and J. A. Rowlands, "Direct-conversion flat-panel X-ray image sensors for digital radiography," *Proc. IEEE*, vol. 90, no. 4, pp. 591–604, Apr. 2002, DOI: 10.1109/JPROC.2002.1002529.

[5] S. Kasap, J. B. Frey, G. Belev, O. Tousignant, H. Mani, J. Greenspan, L. Laperriere, O. Bubon, A. Reznik, G. DeCrescenzo, K. S. Karim, and J. A. Rowlands, "Amorphous and Polycrystalline Photoconductors for Direct Conversion Flat Panel X-Ray Image Sensors," *Sensors*, vol. 11, no. 5, pp. 5112–5157, May 2011, DOI: 10.3390/s110505112.

[6] B. T. Polischuk, S. Savard, V. Loustaneau, M. Hansroul, S. Cadieux, and A. Vaque, "Se-based flat-panel detector for screening mammography," *Proc. SPIE*, vol. 4320, pp. 582–589, Jun. 2001, DOI:10.1117/12.430884.

[7] G. Zentai, "Comparison of CMOS and a-Si flat panel imagers for X-ray imaging," in *2011 IEEE Int. Conf. Imaging Syst. Tech.*, May 2011, pp. 194–200, DOI: 10.1109/IST.2011.5962217.

[8] P. R. Granfors, "Performance characteristics of an amorphous silicon flat-panel x-ray imaging detector," *Proc. SPIE*, vol. 3659, pp. 480–490, May 1999, DOI: 10.1117/12.349525.

[9] J. H. Siewerdsen and D. A. Jaffray, "A ghost story: Spatio-temporal response

characteristics of an indirect-detection flat-panel imager," *Med. Phys.*, vol. 26, no. 8, pp. 1624–1641, Aug. 1999, DOI: 10.1118/1.598657.

[10] L. Korthout, D. Verbugt, J. Timpert, A. Mierop, W. de Haan, W. Maes, J. de Meulmeester, W. Muhammad, B. Dillen, H. Stoldt, Others, W. De Haan, J. De Meulmeester, I. Peters, and E. Fox, "A wafer-scale CMOS APS imager for medical X-ray applications," *Proc. 2009 Int. Image Sens. Work. Pap.*, vol. 70, pp. 22–28, 2009.

[11] R. A. Street, S. E. Ready, K. Van Schuylenbergh, J. Ho, J. B. Boyce, P. Nylen, K. Shah, L. Melekhov, and H. Hermon, "Comparison of PbI_2 and HgI_2 for direct detection active matrix x-ray image sensors," *J. Appl. Phys.*, vol. 91, no. 5, pp. 3345–3355, Mar. 2002, DOI: 10.1063/1.1436298.

[12] G. Zentai, L. D. Partain, R. Pavlyuchkova, C. Proano, G. F. Virshup, L. Melekhov, A. Zuck, B. N. Breen, O. Dagan, A. Vilensky, M. Schieber, H. Gilboa, P. Bennet, K. S. Shah, Y. N. Dmitriyev, J. A. Thomas, M. J. Yaffe, and D. M. Hunter, "Mercuric iodide and lead iodide x-ray detectors for radiographic and fluoroscopic medical imaging," *Proc. SPIE*, vol. 5030, pp. 77–91, Jun. 2003, DOI: 10.1117/12.480227.

[13] H. Jiang, Q. Zhao, L. E. Antonuk, Y. El-Mohri, and T. Gupta, "Development of active matrix flat panel imagers incorporating thin layers of polycrystalline HgI_2 for mammographic x-ray imaging," *Phys. Med. Biol.*, vol. 58, no. 3, pp. 703–714, Feb. 2013, DOI: 10.1088/0031-9155/58/3/703.

[14] S. Adachi, N. Hori, K. Sato, S. Tokuda, T. Sato, K. Uehara, Y. Izumi, H. Nagata, Y. Yoshimura, and S. Yamada, "Experimental evaluation of a-Se and CdTe flat-panel x-ray detectors for digital radiography and fluoroscopy," *Proc. SPIE*, vol. 3977, pp. 38–47, Apr. 2000, DOI: 10.1117/12.384511.

[15] K. M. Oh, Y. J. Heo, D. K. Kim, J. S. Kim, J. W. Shin, G. H. Lee, and S. H. Nam, "Improvement of the charge-carrier transport property of polycrystalline CdTe for digital fluoroscopy," *J. Inst.*, vol. 9, no. 5, p. C05033, May 2014, DOI: 10.1088/1748-0221/9/05/C05033.

[16] S. Lee, J. S. E. Kim, K. R. Ko, G. H. Lee, D. J. Lee, D. wook W. Kim, J. S. E. Kim, H. K. Kim, D. wook W. Kim, and S. Im, "Direct Thermal Growth of Large Scale Cl-doped CdTe

Film for Low Voltage High Resolution X-ray Image Sensor," *Sci. Rep.*, vol. 8, no. 1, p. 14810, Dec. 2018, DOI: 10.1038/s41598-018-33240-1.

[17] S. Tokuda, S. Adachi, T. Sato, T. Yoshimuta, H. Nagata, K. Uehara, Y. Izumi, O. Teranuma, and S. Yamada, "Experimental evaluation of a novel CdZnTe flat-panel x-ray detector for digital radiography and fluoroscopy," *Proc. SPIE*, vol. 4320, pp. 140–147, Jun. 2001, DOI: 10.1117/12.430924.

[18] S. Tokuda, H. Kishihara, S. Adachi, and T. Sato, "Improvement of temporal response and output uniformity of polycrystalline CdZnTe films for high-sensitivity x-ray imaging," *Proc. SPIE*, vol. 5030, pp. 861–870, Jun. 2003, DOI: 10.1117/12.479938.

[19] M. Simon, R. A. Ford, A. R. Franklin, S. P. Grabowski, B. Menser, G. Much, A. Nascetti, M. Overdick, M. J. Powell, and D. U. Wiechert, "PbO as direct conversion x-ray detector material," *Proc. SPIE*, vol. 5368, pp. 188–199, May 2004, DOI: 10.1117/12.533010.

[20] O. Semeniuk, O. Grynko, G. Decrescenzo, G. Juska, K. Wang, and A. Reznik, "Characterization of polycrystalline lead oxide for application in direct conversion X-ray detectors," *Sci. Rep.*, vol. 7, no. 1, p. 8659, Dec. 2017, DOI: 10.1038/s41598-017-09168-3.

[21] G. Kakavelakis, M. Gedda, A. Panagiotopoulos, E. Kymakis, T. D. Anthopoulos, and K. Petridis, "Metal Halide Perovskites for High-Energy Radiation Detection," *Adv. Sci.*, vol. 7, no. 22, p. 2002098, Nov. 2020, DOI: 10.1002/advs.202002098.

[22] W. Zhao, G. DeCrescenzo, S. O. Kasap, and J. A. Rowlands, "Ghosting caused by bulk charge trapping in direct conversion flat-panel detectors using amorphous selenium," *Med. Phys.*, vol. 32, no. 2, pp. 488–500, Jan. 2005, DOI: 10.1118/1.1843353.

[23] H. Kawashima, R. Tanaka, K. Ichikawa, K. Matsubara, H. Iida, and S. Sanada, "Investigation of image lag and modulation transfer function in fluoroscopy images obtained with a dynamic flat-panel detector," *Radiol. Phys. Technol.*, vol. 6, no. 2, pp. 367–374, Jul. 2013, DOI: 10.1007/s12194-013-0210-9.

[24] S. Abbaszadeh, C. C. Scott, O. Bubon, A. Reznik, and K. S. Karim, "Enhanced Detection Efficiency of Direct Conversion X-ray Detector Using Polyimide as Hole-Blocking Layer," *Sci. Rep.*, vol. 3, no. 1, p. 3360, Dec. 2013, DOI: 10.1038/srep03360.

[25] B. Zhao and W. Zhao, “Temporal performance of amorphous selenium mammography detectors,” *Med. Phys.*, vol. 32, no. 1, pp. 128–136, Dec. 2004, DOI: 10.1118/1.1827791.

[26] B. T. Polischuk, Z. Shukri, A. Legros, and H. Rougeot, “Selenium direct-converter structure for static and dynamic x-ray detection in medical imaging applications,” *Proc. SPIE*, vol. 3336, pp. 494–504, Jul. 1998, DOI: 10.1117/12.317051.

[27] O. Semeniuk, O. Grynko, G. Juska, and A. Reznik, “Amorphous lead oxide (a-PbO): suppression of signal lag via engineering of the layer structure,” *Sci. Rep.*, vol. 7, no. 1, p. 13272, Dec. 2017, DOI: 10.1038/s41598-017-13697-2.

[28] O. Grynko, T. Thibault, E. Pineau, G. Juska, and A. Reznik, “Bilayer lead oxide X-ray photoconductor for lag-free operation,” *Sci. Rep.*, vol. 10, no. 1, p. 20117, Dec. 2020, DOI: 10.1038/s41598-020-77050-w.

[29] J. H. Hubbell and S. M. Seltzer, “Tables of X-Ray Mass Attenuation Coefficients and Mass Energy-Absorption Coefficients from 1 keV to 20 MeV for Elements Z = 1 to 92 and 48 Additional Substances of Dosimetric Interest (version 1.4),” National Institute of Standards and Technology, Jul. 2004, DOI: 10.18434/T4D01F.

[30] M. Z Kabir, F. Manouchehri, S. A. Mahmood, V. K. Devabhaktuni, O. Tousignant, H. Mani, J. Greenspan, and P. Botka, “Modeling of dark current and ghosting in multilayer amorphous selenium x-ray detectors,” *Proc. SPIE*, vol. 6913, p. 69133U, Mar. 2008, DOI: 10.1117/12.770697.

[31] G. Belev and S. O. Kasap, “Reduction of the dark current in stabilized a-Se based X-ray detectors,” *J. Non. Cryst. Solids*, vol. 352, no. 9–20, pp. 1616–1620, Jun. 2006, DOI: 10.1016/j.jnoncrysol.2005.11.086.

[32] S. Kasap, J. B. Frey, G. Belev, O. Tousignant, H. Mani, L. Laperriere, A. Reznik, and J. A. Rowlands, “Amorphous selenium and its alloys from early xeroradiography to high resolution X-ray image detectors and ultrasensitive imaging tubes,” *phys. stat. sol. (b)*, vol. 246, no. 8, pp. 1794–1805, Aug. 2009, DOI: 10.1002/pssb.200982007.

[33] O. Bubon, G. DeCrescenzo, W. Zhao, Y. Ohkawa, K. Miyakawa, T. Matsubara, K. Kikuchi, K. Tanioka, M. Kubota, J. A. Rowlands, and A. Reznik, “Electroded avalanche amorphous selenium (a-Se) photosensor,” *Curr. Appl. Phys.*, vol. 12, no. 3, pp. 983–988,

May 2012, DOI: 10.1016/j.cap.2011.12.023.

[34] S. Abbaszadeh, K. Rom, O. Bubon, B. A. A. Weinstein, K. S. S. Karim, J. A. A. Rowlands, and A. Reznik, "The effect of the substrate on transient photodarkening in stabilized amorphous selenium," *J. Non. Cryst. Solids*, vol. 358, no. 17, pp. 2389–2392, Sep. 2012, DOI: 10.1016/j.jnoncrysol.2011.12.098.

[35] O. Semeniuk, A. Csik, S. Kökényesi, and A. Reznik, "Ion-assisted deposition of amorphous PbO layers," *J. Mater. Sci.*, vol. 52, no. 13, pp. 7937–7946, Jul. 2017, DOI: 10.1007/s10853-017-0998-5.

[36] J. B. Frey, K. Sadasivam, G. Belev, H. Mani, L. Laperriere, and S. Kasap, "Dark current–voltage characteristics of vacuum deposited multilayer amorphous selenium-alloy detectors and the effect of x-ray irradiation," *J. Vac. Sci. Technol. A*, vol. 37, no. 6, p. 061501, Dec. 2019, DOI: 10.1116/1.5121197.

[37] A. Camlica, M. Z. Kabir, J. Liang, P. M. Levine, D. L. Lee, and K. S. Karim, "Use of Pulse-Height Spectroscopy to Characterize the Hole Conduction Mechanism of a Polyimide Blocking Layer Used in Amorphous-Selenium Radiation Detectors," *IEEE Trans. Electron Devices*, vol. 67, no. 2, pp. 633–639, Feb. 2020, DOI: 10.1109/TED.2019.2958789.

[38] J. B. Frey, G. Belev, O. Tousignant, H. Mani, L. Laperriere, and S. O. Kasap, "Dark current in multilayer stabilized amorphous selenium based photoconductive x-ray detectors," *J. Appl. Phys.*, vol. 112, no. 1, p. 014502, Jul. 2012, DOI: 10.1063/1.4730135.

[39] S. A. Mahmood, M. Z. Kabir, O. Tousignant, H. Mani, J. Greenspan, and P. Botka, "Dark current in multilayer amorphous selenium x-ray imaging detectors," *Appl. Phys. Lett.*, vol. 92, no. 22, p. 223506, Jun. 2008, DOI: 10.1063/1.2938888.

[40] O. Semeniuk, G. Juska, J.-O. Oelerich, M. Wiemer, S. D. Baranovskii, and A. Reznik, "Charge transport mechanism in lead oxide revealed by CELIV technique," *Sci. Rep.*, vol. 6, no. 1, p. 33359, Dec. 2016, DOI: 10.1038/srep33359.

[41] J. Vilar-Palop, J. Vilar, I. Hernandez-Aguado, I. Gonzalez-Alvarez, and B. Lumbreras, "Updated effective doses in radiology," *J. Radiol. Prot.*, vol. 36, no. 4, pp. 975–990, Dec. 2016, DOI: 10.1088/0952-4746/36/4/975.

[42] A. M. Asbeutah, A. A. AlMajran, A. Brindhaban, and S. A. Asbeutah, "Comparison of

radiation doses between diagnostic full-field digital mammography (FFDM) and digital breast tomosynthesis (DBT): a clinical study," *J. Med. Radiat. Sci.*, vol. 67, no. 3, pp. 185–192, Sep. 2020, DOI: 10.1002/jmrs.405.

Acknowledgment

Financial support from Teledyne DALSA, the Natural Sciences and Engineering Research Council of Canada (NSERC) and Mitacs is gratefully acknowledged.

Manuscript received: January 18, 2021; **revised**: February 26, 2021; **accepted**: March 17, 2021.

Date of publication: March 29, 2021; **date of current version**: April 22, 2021.

Chapter 5

The X-ray Sensitivity of an Amorphous Lead Oxide Photoconductor

This topic has been elaborated in the following publication:

Oleksandr Grynko, Tristen Thibault, Emma Pineau, Alla Reznik. The X-ray Sensitivity of an Amorphous Lead Oxide Photoconductor. *Sensors* 21, 7321 (2021). DOI: 10.3390/s21217321.

The full text of the publication is listed below.

The X-ray Sensitivity of an Amorphous Lead Oxide Photoconductor

Oleksandr Grynko [1,*], Tristen Thibault [2], Emma Pineau [2] and Alla Reznik [2,3]

1 Chemistry and Materials Science Program, Lakehead University, Thunder Bay, ON, P7B 5E1, Canada; ogrynko@lakeheadu.ca

2 Physics Department, Lakehead University, Thunder Bay, ON, P7B 5E1, Canada; ttthibau@lakeheadu.ca (T.T.), enpineau@lakeheadu.ca (E.P.), areznik@lakeheadu.ca (A.R.)

3 Thunder Bay Regional Health Research Institute, Thunder Bay, ON, P7B 6V4, Canada

* Correspondence: ogrynko@lakeheadu.ca

Abstract: The photoconductor layer is an important component of direct conversion flat panel X-ray imagers (FPXI); thus, it should be carefully selected to meet the requirements for the X-ray imaging detector, and its properties should be clearly understood to develop the most optimal detector design. Currently, amorphous selenium (a-Se) is the only photoconductor utilized in commercial direct conversion FPXIs for low-energy mammographic imaging, but it is not practically feasible for higher-energy diagnostic imaging. Amorphous lead oxide (a-PbO) photoconductor is considered as a replacement to a-Se in radiography, fluoroscopy, and tomosynthesis applications. In this work, we investigated the X-ray sensitivity of a-PbO, one of the most important parameters for X-ray photoconductors, and examined the underlying mechanisms responsible for charge generation and recombination. The X-ray sensitivity in terms of electron–hole pair creation energy, $W_{\pm}$, was measured in a range of electric fields, X-ray energies, and exposure levels. $W_{\pm}$ decreases with the electric field and X-ray energy, saturating at 18–31 eV/ehp, depending on the energy of X-rays, but increases with the exposure rate. The peculiar dependencies of $W_{\pm}$ on these parameters lead to a conclusion that, at electric fields relevant to detector operation (~10 V/μm), the columnar recombination and the bulk recombination mechanisms interplay in the a-PbO photoconductor.

Keywords: lead oxide; X-ray detector; direct conversion; X-ray sensitivity; columnar recombination; Langevin recombination; Monte Carlo simulation

1. Introduction

The ever-growing demand for advanced radiation medical imaging techniques sustains continued research interest in novel materials and technologies for imaging detectors, based on the direct conversion of diagnostic X-rays. In direct conversion flat panel X-ray imagers (FPXIs), a uniform layer of the photoconductor is deposited over large area readout electronics based on either thin-film transistor (TFT) arrays or complementary metal-oxide-semiconductor (CMOS) active-matrix arrays. The photoconductor acts as a direct X-ray-to-charge transducer; i.e., it absorbs X-rays and directly creates electron–hole pairs (ehps), which are subsequently separated by a bias field to generate a signal.

Stabilized amorphous selenium (a-Se) is the most successful, commercially viable, large-area-compatible X-ray photoconductor used in direct conversion FPXIs for medical imaging due to its several distinct advantages over other potentially competing photoconductors [1,2]. Both X-ray-generated electrons and holes can drift in a-Se under appropriate conditions [3,4]. The dark current can be appropriately controlled by the use of blocking structures [5,6]. The X-ray attenuation coefficient, while not outstanding, is acceptable for the relatively soft X-rays in mammographic energy range (~20 keV) [1,3]. The fabrication technology of the practical photoconductive layers is mature enough, and thus cost-effective. Therefore, the most successful application of stabilized a-Se technology is in mammography where a-Se-based FPXIs became a dominant technology [1,7]. However, for higher energy applications such as radiography, fluoroscopy, and tomosynthesis, a-Se does not have sufficient X-ray stopping power, and thus, alternative materials are needed to expand the success of the direct conversion concept over the diagnostic energy range. In this regard, one should focus on the development of high-Z (atomic number), wide-bandgap photoconductors that can efficiently attenuate high-energy X-ray photons and are compatible with the FPXI technology. The latter requires the feasibility to be deposited over the imaging array under deposition conditions suitable for imaging electronics, such as a deposition temperature that imaging electronics can withstand (practically below 250 °C), a high deposition rate, and high uniformity across a large area [1].

The requirement for a relatively low deposition temperature makes single-crystalline photoconductors unsuitable for use in direct conversion imaging detectors. As for the disordered (polycrystalline and amorphous), high-Z semiconductors that can produce large-area detectors,

polycrystalline layers of PbI_2 [8–10], HgI_2 [10–12], CdTe [13], $Cd_{1-x}Zn_xTe$ [14], BiI_3 [15], ZnO [16], PbO [17,18], perovskites [19], and amorphous PbO (a-PbO) [20,21] are considered promising. However, at the current stage of their technology, the majority of the materials in this list exhibit signal lag—a residual current that continues to flow after X-ray exposure [17,18,22]. The presence of this residual signal has a detrimental effect on procedures with fast sequential image acquisition, such as real-time imaging (fluoroscopy) and 3D imaging (tomosynthesis), since part of the signal from a previous exposure combines with the next one. The resulting image can be inaccurate, misleading, and as such, can compromise the whole visualization advantage of real-time (fluoroscopic) imaging. For practical fluoroscopic applications, the residual signal should promptly decay to <10% in less than 33 ms, i.e., within the first frame, appertaining to a 30 frames per second (fps) read-out [23–27]. To the best of our knowledge, today, the only photoconductors exempted from the issue of signal lag are a-Se [5,28] and amorphous lead oxide—a new non-crystalline polymorph of PbO [29], in which signal lag was suppressed to a level <5% [20] that fits the requirements of fluoroscopic applications. In the continuous advancement of a-PbO technology, we recently reported on the development of a blocking structure for a-PbO detectors, in which a thin layer of polyimide (PI) is introduced between the electrode and a-PbO layer, thereby preventing their interaction. This blocking structure is needed to maintain low dark current (<1 pA/mm^2) in a strong operational electric field (≥10 V/μm), while preserving the temporal performance suitable for real-time imaging with lag values down to 0.9% at 30 fps read-out [21].

One of the most important parameters for X-ray photoconductors is its X-ray sensitivity, characterized in terms of the ehp creation energy $W_{\pm}$, which is the average energy required to generate a single detectable electron and hole pair. The lower the $W_{\pm}$, the higher the X-ray sensitivity of a photoconductor. This parameter accounts solely for the freed carriers, reflecting the fact that only a fraction of the X-ray-generated charges are collected. Indeed, a theoretical (or, intrinsic) ehp creation energy, $W_{\pm}^0$, can be estimated from the bandgap of the semiconductor, E_g, by an empirical formula, the so-called Klein rule: $W_{\pm}^0 \approx 3E_g$ [30]. However, in practice, in many photoconductors, including a-Se [31], poly-PbO [17,18,22], and a-PbO [20] ones, experimentally measured (or, effective) $W_{\pm}$ is not a material parameter, but a characteristic of the system which depends on the applied electric field F, X-ray energy E, photon flux (or exposure X), and

temperature T. Understanding of $W_{\pm}(F, E, X, T)$ dependencies in a-PbO photoconductors is crucial for the development and optimization of an a-PbO-based direct conversion X-ray imaging detector.

In this work, we investigated the X-ray sensitivity of an a-PbO photoconductor in terms of $W_{\pm}$ and examined the underlying mechanisms responsible for charge generation and recombination in this material through experimental measurements of $W_{\pm}$ and Monte Carlo simulations of photoelectron transport. $W_{\pm}$ was measured in a range of electric fields, X-ray energies, and exposures. The peculiar dependency of X-ray sensitivity on these parameters leads to a conclusion that the interplay of the columnar and bulk recombination mechanisms dominates in the a-PbO photoconductor at electric fields relevant to detector operation (i.e., 10 V/μm). Finally, we suggest a qualitative model for the charge generation and recombination processes in the a-PbO photoconductor that is supported by a Monte Carlo simulation.

2. Background

It was suggested that the intrinsic ehp creation energy, $W_{\pm}^{0}$, of a semiconductor depends on its bandgap E_g according to the relationship $W_{\pm}^{0} \approx 2.8E_g + \varepsilon_{ph}$ (Klein rule for crystalline semiconductors [30]) or $W_{\pm}^{0} \approx 2.2E_g + \varepsilon_{ph}$ (Que–Rowlands rule for amorphous solids [32]), where the term $\varepsilon_{ph} \approx 0.5 - 1$ eV is responsible for losses due to optical phonons. In practice, many low-mobility amorphous and polycrystalline semiconductors demonstrate effective $W_{\pm}$ that is higher than the intrinsic value. For example, $W_{\pm}$ is ~45 eV/ehp for a-Se [3], ~17 eV/ehp for poly-PbO [18], and ~22 eV/ehp for a-PbO [20] at a practical electric field of F = 10 V/μm, whereas theoretical values are within 5–7 eV/ehp. The fact that experimental $W_{\pm}$ exceeds the theoretical value indicates that a certain portion of the initially X-ray-generated charge undergoes deep trapping or recombination and thus does not contribute to the photo-signal, reducing the detector's sensitivity, and ultimately degrading the SNR of the image.

Generally speaking, the carriers can be trapped at localized states within the mobility gap of a-PbO, in either shallow or deep traps. However, a previous investigation of the ghosting effect [21] suggested that no deep trapping occurs in PI/a-PbO photoconductive structures, at least at the relatively low exposures used in this study. Ghosting is caused by deep bulk trapping of photogenerated carriers, which subsequently recombine with the drifting carriers of the opposite

sign, resulting in sensitivity degradation. Since no detectable ghosting effect was observed at relevant exposure rates, deep trapping can be ruled out as a primary cause for $W_{\pm}$ degradation. Additionally, the quasi-rectangular shape of the X-ray response indicates the unrestricted flow of the photogenerated carriers from the a-PbO photoconductive layer through the PI blocking layer into the ITO electrode [21], meaning that no accumulation of carriers in shallow states at the PI/a-PbO interface are expected as well. Therefore, a trapping mechanism can be excluded from the reasons for the carrier loss in a-PbO and will not be discussed further.

As for the recombination, there are three main theories that could explain the loss of the X-ray-generated carriers in the photoconductors: the bulk (Langevin), geminate (Onsager), and columnar (track) models [32–41]. Bulk Langevin recombination is a bimolecular process in which electrons and holes drift through the bulk of the photoconductor, due to the internal electric field within the layer, meet each other in space and time, and recombine. The two other intra-track mechanisms, i.e., geminate and columnar recombination, occur within the ionization column formed along the track of the energetic primary photoelectron. In the geminate model described by Onsager theory [42], the twin generated electron and hole pair recombine with each other while diffusing and drifting in the presence of their mutual Coulomb attraction and the applied electric field. Columnar recombination, first proposed by Jaffe [43] and expanded by Hirsch and Jahankhani [44], assumes that the photogenerated charge density inside the column is high enough so that the concept of independent geminate ehps is inapplicable. In this case, bimolecular recombination occurs between two non-geminate charges (i.e., electron and hole from two different twin pairs), just like in the bulk Langevin model, but within the ionization column.

The applicability of the recombination models depends on the properties of the material under consideration, and also on the source of excitation. For example, it was shown that the recombination of drifting holes with either drifting or trapped electrons in a-Se follows the bulk Langevin recombination mechanism [45,46]; initial recombination of optically excited carriers is controlled by the geminate mechanism [47], but columnar recombination prevails in the case of X-ray photogeneration [2,33,34,36]. On the other hand, geminate recombination controls the effective $W_{\pm}$ in X-ray irradiated anthracene, PVK, and in electron-bombarded SiO_2 ([32,39,40] and references therein). Although these materials have some common properties (i.e., low mobility), they have different recombination mechanisms. Therefore, one cannot rule out any of

these theories a priori, but must first assess their fitness based on the experimental results. Conveniently, the recombination rate of each mechanism depends uniquely on experimental parameters such as electric field, exposure, X-ray photon energy, and temperature, which can be used to identify the dominant process.

2.1. Exposure Dependency

Bulk bimolecular recombination in amorphous solids is usually described using the Langevin formalism, which states that the recombination rate is proportional to the concentration of both types of carriers. Therefore, if bulk recombination is a dominant process, the collected charge Q should change with exposure X according to $Q \sim X^{1/2}$ [40].

The situation is different for the intra-track mechanisms. With increasing radiation intensity, the number of primary photoelectron tracks proportionally increases, but the recombination within each track remains unaffected. This means that for geminate and columnar mechanisms, the collected charge increases linearly with the exposure, following $Q \sim X$ [39]. Additionally, geminate recombination is a monomolecular process; therefore, the recombination probability does not depend on the concentration of the surrounding charges (since the separation between the geminate electron and hole is the smallest distance between any two oppositely charged carriers), and thus the relationship $Q \sim X$ is adhered to again [41].

2.2. Field Dependency

The X-ray sensitivity in many X-ray photoconductors (i.e., a-Se, poly-PbO, a-PbO, perovskites) shows a very pronounced electric field dependency [3,18,20,48]. It is usually described as $W_{\pm}(F) = W_{\pm}^{0} + B/F$, where $W_{\pm}^{0}$ is the intrinsic ehp creation energy at an "infinite" field and B is a material-specific constant that depends on the energy of X-ray photons ([1,33] and references therein).

Regardless of the mechanism, the recombination rate is determined by the probability of carriers meeting in space. It ultimately depends on the interplay between three main driving forces: charge carrier thermal diffusion, charge carrier drift in the applied electric field, and mutual attraction between the oppositely charged carriers. The applied electric field acts to overcome mutual Coulombic attraction between photogenerated electrons and holes, increasing the recombination escape probability. This results in a higher number of freed ehps and lower $W_{\pm}$ [36].

Such field-dependent sensitivity is typical for both columnar and geminate recombination ([33,34] and references therein), although each of them has its own peculiarities. In the columnar model, at the very low electric fields (≲1 V/μm, when diffusion dominates over drift), $W_{\pm}$ is field-independent [41]. In the geminate model, the low-field portion of the photogeneration efficiency $\eta(F) = W_{\pm}^{0}/W_{\pm}(F)$ is a straight line with a slope-to-intercept ratio $R_{SI} = e^3/(8\pi\varepsilon_r\varepsilon_0 k^2T^2)$, where e—elementary charge, ε_r—relative permittivity of the photoconductor, ε_0—vacuum permittivity, and k—Boltzmann's constant ([33] and references therein).

The fraction of carriers lost to bulk recombination is proportional to F^{-2}, and thus the collected charge is given by $Q \sim 1/(1 + F^{-2})$ [41,49].

2.3. X-ray Energy Dependency

To the best of our knowledge, the only photoconductor whose X-ray energy dependency on $W_{\pm}$ has been examined (both experimentally [31,41,50–52] and theoretically [34,35,37,53–55]) is a-Se. As was discussed in [34] (and references therein), within the framework of the geminate recombination model, the initial separation between an electron and a hole controls the probability of their escape from recombination. Therefore, if the initial separation is independent of the incident photon energy, $W_{\pm}$ should be too, if the geminate recombination is the dominant process.

On the other hand, through the example of a-Se, it has been shown that the columnar recombination rate drops with increasing X-ray photon energy [33,34,53]. This is due to a rise in the mean separation of the electrons and holes within the ionization column. As the charge density decreases, the recombination rate between non-geminate electrons and holes within the column also declines. This increases the number of free electrons and holes which, in turn, leads to a reduction in $W_{\pm}$.

3. Materials and Methods

3.1. Detector Preparation

A single-pixel direct conversion digital detector based on an amorphous lead oxide (a-PbO) photoconductor with a single blocking layer of polyimide (PI) was used in this work. Commercially supplied pre-washed and vacuum-packed ITO-coated glass (bottom biasing electrode) was rinsed with acetone, methanol, and isopropanol; dried with dry nitrogen; and placed on a hot plate at 90 °C for 10

min, to ensure cleanliness. A 1 μm thick PI layer was then spin-coated onto the ITO-coated glass. 19 μm of a-PbO was deposited on the prepared substrate by ion-assisted thermal evaporation. Finally, a top Au contact (readout electrode) 1.1 mm in diameter was sputtered atop of the a-PbO, which provided an effective detector area of 0.95 mm^2. Detailed descriptions of the PI application and a-PbO deposition can be found in [21,56].

The density of the a-PbO photoconductor ρ was calculated from the mass m and volume of the film, which can be treated as a cylinder with a height d and radius r; thus, $\rho = m/(\pi r^2 d)$. The a-PbO deposition was performed using a shadow mask with a window of radius r = 6.25 mm. The photoconductor thickness d = 19 μm was measured with a stylus profilometer (KLA Tenchor Alpha-Step D-100, Milpitas, CA, USA). The glass substrate with the applied PI layer was weighed on a microbalance (Sartorius CP2P, Göttingen, Germany) before and after deposition of a-PbO film to calculate the mass of the photoconductor layer: m = 20.5 mg. The density was found to be ρ = 8.8 g/cm^3, which was 92% of the crystalline PbO density (9.53 g/cm^3), owing to high packing density and the absence of voids in the a-PbO layer [56].

3.2. Experimental Apparatus

X-ray characterization of the PI/a-PbO detector was performed using the X-ray-induced photocurrent method (XPM). The experimental setup is shown in Figure 1. A detector was placed in a shielded aluminum box. Prior to measurement, the detector was short-circuited in the dark to allow for the complete detrapping of charge carriers. A positive dc bias was applied to the ITO by a high voltage power supply (Stanford Research Systems PS350, Sunnyvale, CA, USA) to create a strong electric field in the photoconductor. The photocurrent due to the drifting carriers was read out from the Au electrode by an oscilloscope (Tektronix TDS 2024C, Beaverton, OR, USA) with a native input resistance of 1 MΩ. In this work, the electric field is referred to as an applied field to the detector $F = V_{bias}/(d_{PbO} + d_{PI})$, where V_{bias} is an applied bias, and d_{PbO} and d_{PI} are the thicknesses of the a-PbO and PI layers, respectively. After such a bias is applied, the dark current in the PI/a-PbO detector exponentially decreases with time due to the accumulation of trapped charge within the PI blocking layer [21]. Therefore, the bias was applied to the detector for 15 min prior to irradiation to allow the dark current to stabilize and to drop to a level below 5 pA/mm^2. An X-ray unit (tube Dunlee PX1412CS, insert DU-304, generator CPI Indico 100, Georgetown, ON, Canada) with a tungsten target was used to generate X-ray pulses. The tube voltage could be varied in the range of 40–100 kVp

and the tube current could be set in between 25 mA and 400 mA. 2-mm Lead collimators were used to form a narrow-beam geometry and to minimize scattering. An added filtration of Aluminum (type 1100, min 99.0% purity) was placed in the cassette in front of the X-ray tube to harden the X-ray beam. The exposure was monitored by dosimeter Keithley 35040 (Cleveland, OH, USA) with ionization chamber Keithley 96035 (Cleveland, OH, USA). The ion chamber was positioned midway between the detector and the tube to avoid any contribution of backscattered X-rays to the exposure reading.

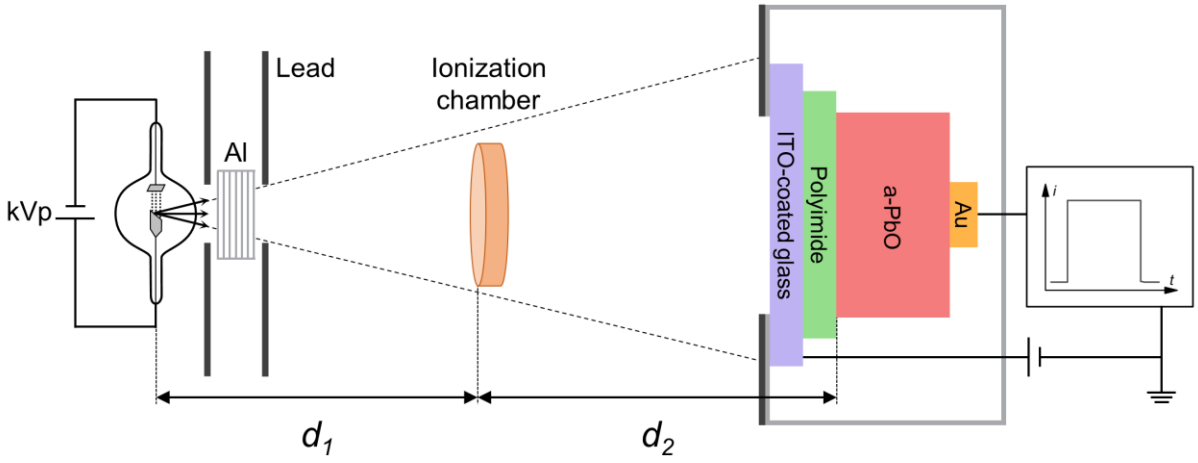

Figure 1. Schematics of the XPM setup (not to scale).

$W_{\pm}$ is derived as a ratio of the total energy absorbed in the photoconductor upon X-ray irradiation E_{abs} to the number of collected ehps N_{ehp}:

$$W_{\pm} = \frac{E_{abs}}{N_{ehp}}. \quad (1)$$

A detailed description of calculation of the absorbed energy, the number of collected charges, and X-ray sensitivity is provided in Appendix A.

3.3. Monte Carlo Simulations

Monte Carlo simulations of the electron trajectories in PbO were performed using the Stopping and Range of Electrons in Matter (SREM)-type Monte Carlo software CASINO (monte CArlo SImulation of electroNs in sOlids) [57]. A PbO sample was irradiated with an electron beam and transport of electrons was simulated, taking into account the physical interaction with the matter. The electron beam energies were selected to represent the kinetic energy of the ejected primary

photoelectrons $KE = h\nu - BE$, where $h\nu$ is the mean energy of the incident X-ray photons in the beam and BE is the binding energy of that photoelectron. Since the mean energies of the X-ray beams used in this work (see Figure A1a) were lower than the *K*-edge energy of PbO ($BE_K = 88$ keV), the photoelectrons were considered to be ejected from the L_3-subshell with binding energy $BE_{L_3} = 13$ keV [58].

The Monte Carlo simulation method and the physical models used were described in [59,60]. For each beam energy, the trajectory information (such as collision event coordinates and energy) from the 500 primary electrons, which included ~10^5–10^6 events (depending on the beam energy), was recorded and further analyzed. The energy difference between two consecutive events was calculated and used as the dissipated energy per collision event, and the coordinates were used to calculate a distance between these consecutive collision sites and the average total path length. Finally, the average ratio of the dissipated energy to the distance between collision sites was calculated for each electron beam energy, which can be treated as the rate of energy deposited in the photoconductor.

4. Results

Figure 2 shows a typical X-ray response of the PI/a-PbO detector to irradiation by a 100-ms X-ray pulse at different applied electric fields and a tube voltage of 60 kVp. Without irradiation, the detector produces only dark current in the order of several picoamps. Upon X-ray irradiation, the detector exhibits a quasi-rectangular response with a uniform amplitude. The photocurrent increases with the electric field and begins to saturate after 10 V/μm. After the irradiation is terminated, the photocurrent rapidly drops to a dark current level, demonstrating almost negligible signal lag. A detailed analysis of the temporal performance (evaluated in terms of signal lag and ghosting) of the a-PbO-based detectors can be found in [20,21].

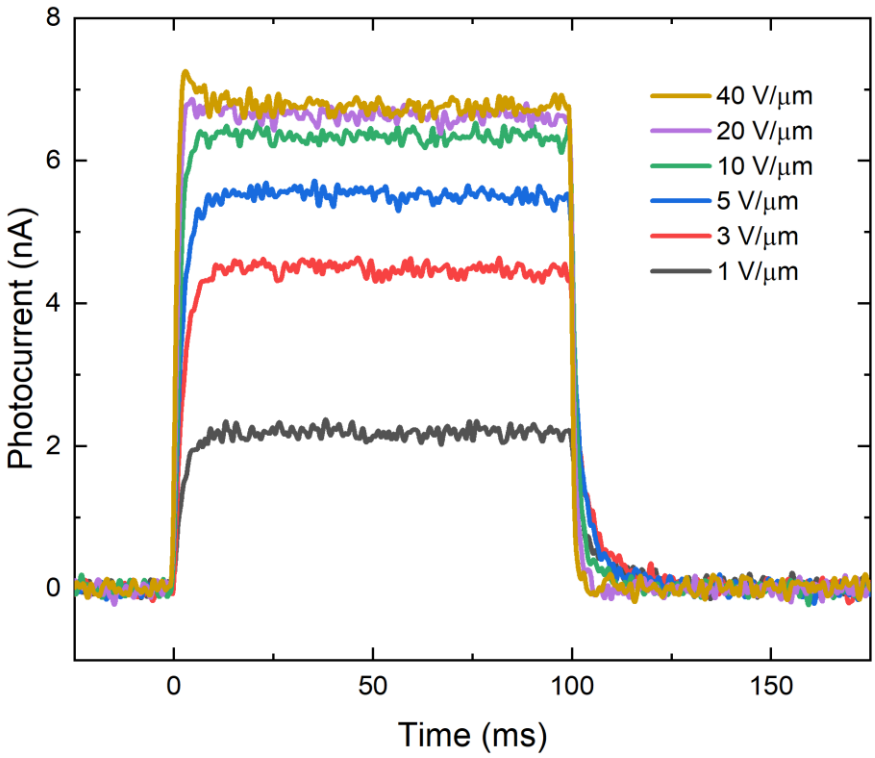

Figure 2. A typical X-ray response to 60 kVp irradiation at different electric fields.

$W_{\pm}$ values were calculated using Equation (1) and plotted as a function of the applied electric field or the reciprocal electric field for different tube voltages in Figure 3a,b, respectively. For the reasons discussed later in the text, the tube current and source-to-detector distance (SDD) were adjusted for each tube voltage to keep a constant exposure level in the photoconductor's plane of 100 mR. As is evident from Figure 3a,b, the sensitivity improves ($W_{\pm}$ decreases) as the field increases, rapidly saturating after 10 V/μm. The saturated values of $W_{\pm}$ depend on the tube voltage: 31, 22, 20, and 18 eV/ehp for 40, 60, 80, and 100 kVp, respectively. As it can be seen, $W_{\pm}$ decreases with increasing tube voltage, and thus with the mean energy of X-ray photons in the beam (see inset in Figure A1a).

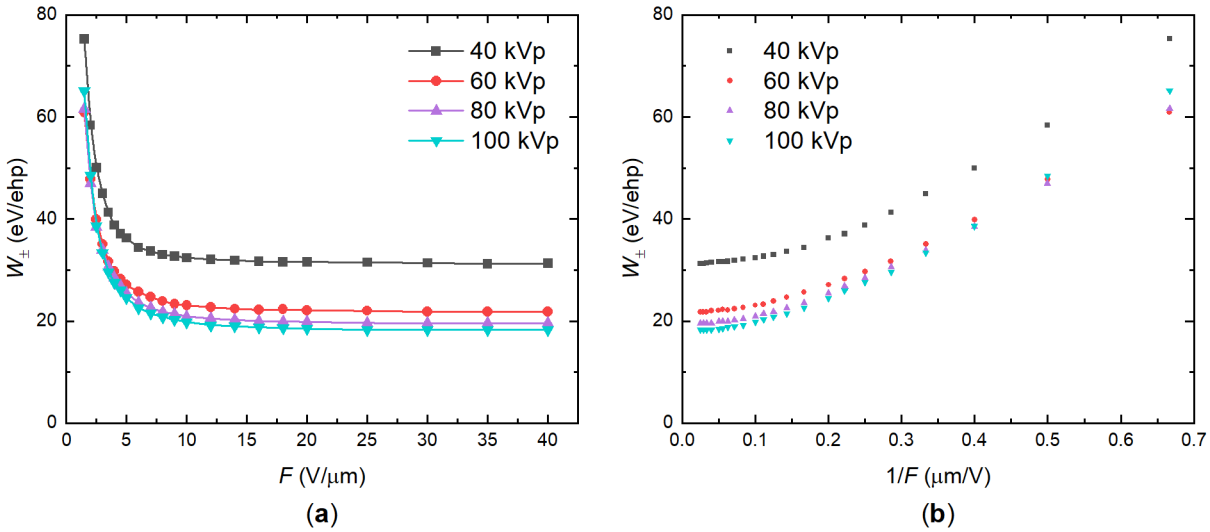

Figure 3. (**a**) $W_{\pm}$ as a function of the electric field at different X-ray tube voltages. $W_{\pm}$ decreases with the field and the energy of X-rays. (**b**) The same values replotted as a function of the reciprocal field $1/F$.

The effect of exposure (X-ray flux) is examined in Figure 4. It was found that $W_{\pm}$ changes with the exposure rate, but not with the exposure itself (i.e., $W_{\pm}$ is identical for two X-ray pulses with the same amplitude but different duration). Therefore, the exposure X dependency of $W_{\pm}$ was measured at a fixed pulse duration $t_{pulse} = 0.1$ s and plotted as a function of exposure rate $X_t = X/t_{pulse}$. Figure 4 shows these results in different electric fields and at different tube voltages: $W_{\pm}$ increases with the exposure rate. At lower fields, $W_{\pm}$ changes more drastically: almost 200% growth when the exposure changes by a factor of 50. The rate of change is similar for different tube voltages. It should be noted that the exposure rates used were much larger than typical radiation levels used in the clinical practices (~10^{-4} R/s for fluoroscopy and ~10^{-1} R/s for 3D mammography [61,62]). However, it was not feasible to use exposures in the micro-roentgens range due to the limited sensitivity of the oscilloscope.

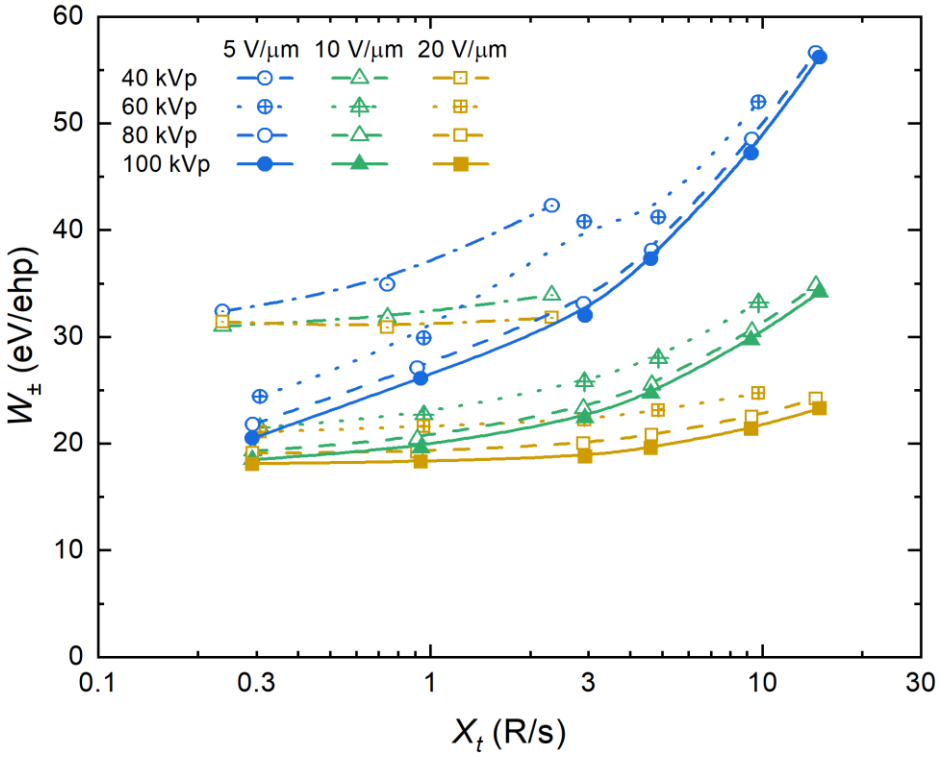

Figure 4. $W_\pm$ as a function of the exposure rate in different electric fields and at different tube voltages. $W_\pm$ increases with the exposure rate.

Since the exposure rate significantly affects the detector's sensitivity, all experiments were performed with the exposure fixed at the lower end of the available range (100 mR per 0.1 s), unless otherwise is specified. This was achieved by adjusting the tube current and SDD.

To investigate the effect of the X-ray photon energy on the $W_\pm$, one has to use a measure of energy that would take the complex shape of a polyenergetic X-ray spectrum into account. The most common parameters are the tube voltage kVp (or, equivalently, the maximum energy of X-ray photons in a beam) and the mean energy E_{mean} (calculated as the energy-weighted average). However, it should be noted that neither of these parameters characterizes a polyenergetic spectrum unambiguously and thus they should be treated as an approximate measure of the beam energy only [63].

$W_\pm$ for different X-ray tube voltages and corresponding mean X-ray energies are shown in Figure 5. The detector's sensitivity improves ($W_\pm$ decreases) as the energy of X-rays increases.

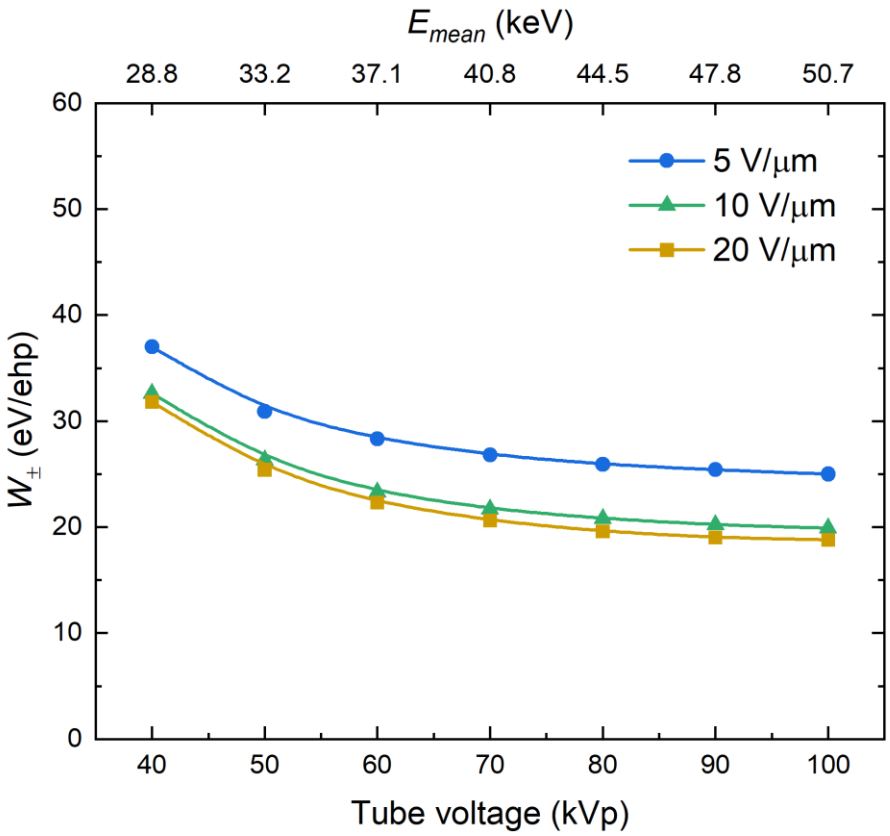

Figure 5. $W_{\pm}$ as a function of tube voltage at different electric fields. $W_{\pm}$ decreases as the energy of X-rays increases.

An alternative way to vary photon energy is by hardening the X-ray beam with added Al filtration. At a fixed tube voltage, a thicker Al filter attenuates the low-energy end of the spectrum and effectively shifts the mean energy towards a higher value. Figure 6 shows $W_{\pm}$ values as a function of mean X-ray energy for different electric fields and tube voltages. Within each tube voltage group, $W_{\pm}$ decreases as the mean energy increases. A discrepancy between $W_{\pm}$ values at the same F and E_{mean}, but different tube voltage, is not surprising, since, as it was mentioned earlier, E_{mean} alone is not a sufficient parameter to characterize the incident polyenergetic X-ray beam. Nevertheless, the trends of the dependencies in Figures 5 and 6 closely resemble each other.

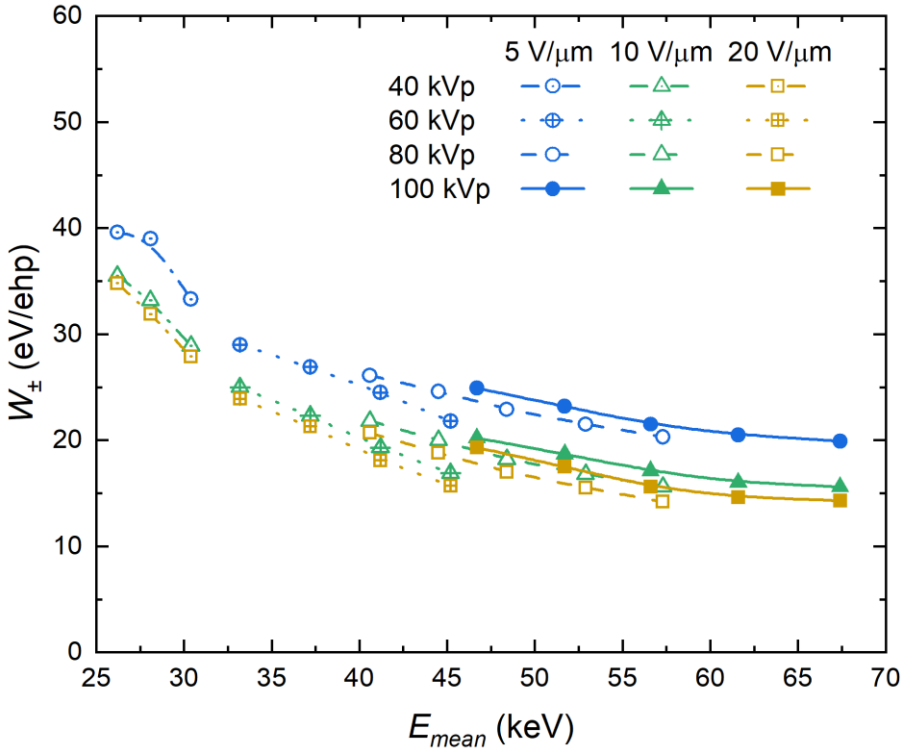

Figure 6. $W_{\pm}$ as a function of the mean energy of X-ray photons at different tube voltages and electric field strengths. $W_{\pm}$ decreases as the energy of X-rays increases.

The electron transport was simulated using the Monte Carlo software CASINO [57]. Table 1 summarizes the results of the simulations and Figure 7 shows an example of typical electron trajectories for 37.7-keV incident electrons in the PbO sample. The electron beam energy of 37.7 keV represents the kinetic energy of a primary photoelectron ejected from the L_3-subshell with the binding energy of 13 keV by the 100 kVp X-ray beam with a mean energy of 50.7 keV. The sample was irradiated by an electron beam from the top side; the electron trajectories are coloured according to their kinetic energy. As the primary electron traveled through the photoconductor, it collided with the atoms and gradually lost its energy. The average energy dissipated in a collision event did not appreciably vary with the initial energy of the primary photoelectron (Table 1). However, the average distance between the collisions (i.e., mean free path) and total path length (i.e., electron range) increased with the primary photoelectron energy, resulting in a declining energy deposition rate (Table 1).

Table 1. Results of the CASINO simulations.

Tube Voltage (kVp) / Mean X-ray Energy (keV)	Electron Energy (keV)	Dissipated Energy per Collision (eV)	Mean Free Path (nm)	Range (μm)	Energy Deposition Rate (eV/nm)
40 / 28.8	15.8	35.3	3.9	1.6	11.8
60 / 37.1	24.1	33.9	5.0	3.3	9.0
80 / 44.5	31.5	33.4	5.9	5.1	7.7
100 / 50.7	37.7	33.6	6.5	6.8	7.0

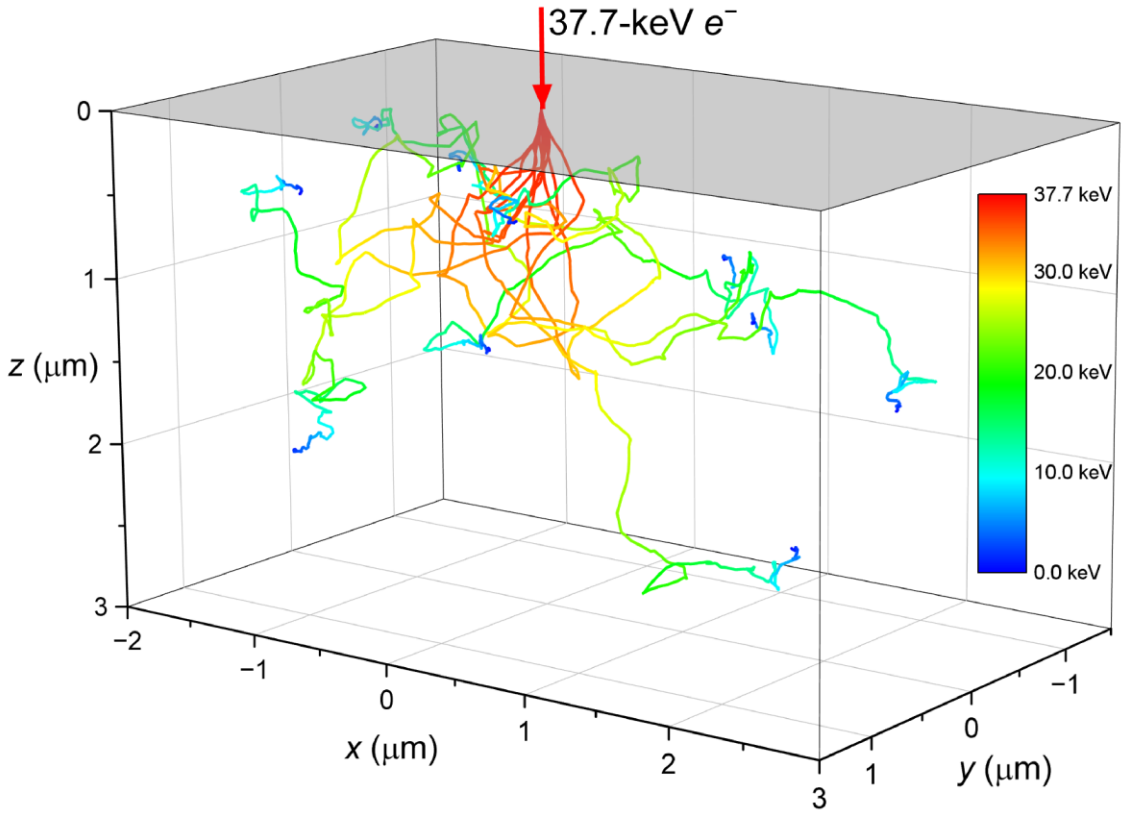

Figure 7. Typical electron trajectories in PbO for a 37.7-keV electron beam.

5. Discussion

The obtained experimental results show well-pronounced dependencies of $W_{\pm}$ on the electric field, X-ray energy, and exposure rate. Now we will try to take into account the presented dependencies in the recombination models, as was previously done for a-Se [33,34,36].

Firstly, let us consider a field dependency in a-PbO demonstrated in Figure 3. $W_{\pm}(F)$ firstly rapidly decreased according to $1/F$ (in the range of fields 1–10 V/μm), but started to saturate at higher fields with no further improvement observed, as is seen in Figure 3b. Replotting results from Figure 3 as $\eta(F)$ yields $R_{SI} = 0.6 - 2$ μm/V, depending on the X-ray energy; however, for a-PbO with $\varepsilon_r = 26$, Onsager theory requires a value of $R_{SI} = 0.041$ μm/V, which plays against the geminate recombination model as a plausible mechanism for photogenerated charge carrier loss in a-PbO.

Furthermore, analysis of the energy deposition during ehps generation and the X-ray energy dependency of the recombination rates rule out the geminate model completely. Indeed, Table 1 shows that the average portion of energy dissipated in a scattering event almost did not change with X-ray energy. Since photoelectric absorption is the main photon interaction mechanism in PbO for the diagnostic X-ray energy range [64], the deposited energy primarily causes ionization and excitation of atoms, i.e., ehps generation. Therefore, the same amount of ehps, on average, is generated in each collision event, and the separation of the geminate pairs remains the same. If geminate recombination is a dominant process, $W_{\pm}$ will be independent of X-ray energy. However, this is not the case: Figures 5 and 6 clearly illustrate that $W_{\pm}$ monotonically decreases with the energy of X-rays. This behaviour disagrees with Onsager formalism but adheres to the columnar model. The decrease of $W_{\pm}$ with gradually increasing energy of X-rays is due to the reduction in the columnar recombination rate caused by the lowering of the photogenerated charge carrier density along the track of primary photoelectron (since the average distance between ionizing events increases, as was demonstrated by our Monte Carlo simulations (Table 1)). Therefore, geminate recombination can be excluded from the reasons for carrier loss in a-PbO, leaving columnar recombination as the dominant process.

Let us now examine the exposure dependency of the collected charge and $W_{\pm}$. For this, the collected photogenerated charge was measured at a constant exposure rate and plotted in Figure 8a as a function of exposure in a log–log scale. The collected charge increased strictly linearly with the exposure, as demonstrated by the unity slope values in the inset to Figure 8a. In this case, both the number of collected ehps and the total energy absorbed were proportional to the exposure, and therefore, $W_{\pm}$ remained unchanged (see Equations (1), (A2) and (A4)). However, if the collected charge is measured at a variable exposure rate and a fixed pulse duration t_{pulse}, its

dependency on the exposure is different. This is shown in Figure 8b: the slope values deviate from unity, and thus $W_{\pm}$ changes, as was demonstrated in Figure 4. At the lower field of 5 V/μm, the collected charge increased as $Q \sim X^{\alpha}$ with an intermediate exponent $\alpha = 0.785$; and at the higher field of 20 V/μm, it changed almost linearly: $\alpha = 0.957$ (see slope values in the inset to Figure 8b). In addition, the slope value decreased with increasing X-ray energy (Figure 8c). Since the exponents take an intermediate value between that for the bulk recombination ($\alpha = 0.5$) and columnar recombination ($\alpha = 1$), this analysis suggests the interplay between bimolecular Langevin recombination in the bulk and the column. Indeed, the carriers first experience the initial columnar recombination, and afterward, the escaped carriers drift through the bulk of the photoconductor and recombine with the carriers from the different columns, giving rise to the bulk Langevin recombination.

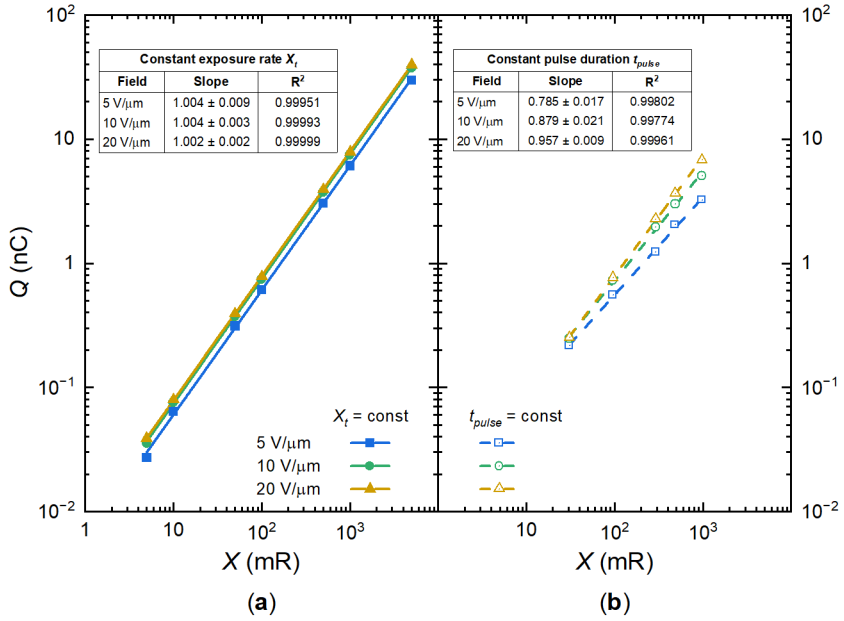

(c)

Slope at contant t_{pulse}	40 kVp	60 kVp	80 kVp	100 kVp
5 V/μm	0.830	0.785	0.760	0.749
10 V/μm	0.959	0.879	0.851	0.846
20 V/μm	0.982	0.957	0.942	0.940

Figure 8. Charge collected versus the exposure for (**a**) the constant exposure rate and (**b**) the constant pulse duration at 60 kVp irradiation. (**c**) Slope values for the case of the constant pulse duration at different kVp and field strengths.

Although the above considerations allow for a qualitative model of X-ray generation and recombination in a-PbO, the saturation of $W_{\pm}$ at energy-dependent values well above the intrinsic $W_{\pm}^{0}$ remains unclear. The lowest experimentally achievable $W_{\pm}$ ranges from 18 eV/ehp at 100 kVp

to 31 eV/ehp at 40 kVp (to be compared with energy-independent $W_{\pm}^{0}$ around 5–6 eV/ehp, as suggested by Klein and Que–Rowlands rules for lead oxide with $E_g = 1.9$ eV [1]).

The saturation of $W_{\pm}$ has been previously observed in the High-gain Avalanche Rushing Photoconductor (HARP) detector with a-Se photoconductor at high electric fields [36]. Indeed, $W_{\pm}$ in a-Se initially decreases with the field as $1/F$. However, in the fields stronger than 80 V/μm, $W_{\pm}$ saturated at a level of ~9 eV/ehp. This saturated value is larger than that theoretically predicted by Klein rule, 5–7 eV/ehp. Such behaviour is explained by the modified columnar recombination model which takes into account that the recombination rate is limited by the smaller of two parameters: time needed for carriers to meet in space and duration of the recombination event itself. In a high electric field, the time for an electron and hole to meet in space becomes smaller than the time needed for the recombination of the electron–hole pair that is on a scale of ~10^{-12} s. As the result, charge drift no longer influences the probability of recombination, which becomes independent of the electric field, and $W_{\pm}$ saturates.

Although saturation of $W_{\pm}$ in a-PbO occurs in an electric field weaker than that for a-Se, it confirms the findings in [36] that the Langevin recombination mechanism should not be expected at strong electric fields. As is shown in Table 1, the energy-dependent mean free pass r_{MFP} between the ionizing collisions in a-PbO is at a scale of several nanometers. This distance can be approximated as a maximum separation between the oppositely charged non-geminate carriers r_0 (although, realistically, r_{MFP} significantly overestimates a mean separation r_0, taking into account that at this distance not a single ehp is created, but rather multiple ehps that form a dense electron cloud—a spur (see Appendix B)). Considering the intrinsic $W_{\pm}^{0} \approx 5$ eV/ehp for a-PbO, the number of pairs generated in each spur could be estimated from the dissipated energy per collision (~35 eV, see Table 1) as ~7 ehps per spur, providing $r_0 \approx 10^{-7}$ cm. Now, assuming that the mobility of holes (faster carriers in PbO) $\mu \approx 1$ cm^2/(V·s) at $F = 10$ V/μm where $W_{\pm}(F)$ saturation begins (which seems a reasonable assumption for hole mobility in PbO at 10 V/μm [65]), the hole drift velocity $v_d = \mu F \approx 10^5$ cm/s. Therefore, the time $\tau = r_0/v_d$ that defines the probability for recombining carriers to meet in space is in the order of 10^{-12} s—shorter than the characteristic time of the recombination event for carriers of opposite sign placed at the same spatial point [36]. Similarly to a-Se, in strong electric fields the recombination in a-PbO becomes limited by the duration of the recombination event: the recombination rate no longer depends on the electric field. Therefore,

$W_{\pm}$ saturates, as was demonstrated in Figure 3. This also explains the saturation of $W_{\pm}$ at different values depending on the X-ray energy. As the mean X-ray energy in a beam increases from 28.8 to 50.7 keV, the mean free path of the primary photoelectron r_{MFP} increases by a factor of 1.7 (Table 1). This results in a reduced initial recombination rate and a saturated $W_{\pm}$ that is lower by the same factor (Figure 3).

6. Conclusions

The X-ray sensitivity in terms of the electron–hole pair creation energy $W_{\pm}$ of a single-pixel PI/a-PbO direct conversion X-ray detector prototype was characterized in a wide range of electric fields, X-ray photon energies (in diagnostic energy range), and exposures using polyenergetic irradiation. $W_{\pm}$ decreased with electric field strength, and above 10 V/μm saturated at 18–31 eV/ehp, depending on the energy of the X-rays—higher photon energy resulted in a lower $W_{\pm}$. In addition, $W_{\pm}$ increased with radiation exposure rate, especially in weaker electric fields. This demonstrates that the PI/a-PbO detector performs best in strong, practical electric fields (10–20 V/μm) in the diagnostic energy range and under low exposures, offering improved sensitivity as compared to a-Se.

The analysis of the field, X-ray energy, and exposure dependencies of the $W_{\pm}$ indicated an interplay between Langevin recombination within the ionization column (i.e., columnar recombination) and bulk Langevin recombination, which together are responsible for the carrier loss and suboptimal $W_{\pm}$ in a-PbO in electric fields weaker than 10 V/μm. In stronger fields, the columnar Langevin recombination cannot account for the observed field dependency of $W_{\pm}$, as the recombination process is no longer determined by the probability of X-ray-generated carriers meeting in space.

Appendix A. X-ray Sensitivity Calculations

In this work, the detector was irradiated with a polyenergetic X-ray beam. Therefore, to accurately calculate the absorbed energy, the shape of the X-ray spectrum must be considered. The X-ray spectrum for the tungsten target at a given tube voltage, tube current, Al filtration, and source-to-

detector distance (SDD) was simulated using the standard Tucker–Barnes–Chakraborty (TBC) model [66].

The validity of the model was verified by a half-value layer (HVL) of Al. Inherent filtration (glass, oil, and Al) can be adjusted in the model until a close match between the experimental and simulated HVL values is achieved, indicating that the modeled spectrum closely represents the one generated by the X-ray unit. To derive an experimental HVL of the beam, the exposure was measured for a naked tube and with added Al filtration of a different thickness up to 3 mm. The data were then interpolated to determine the Al thickness required to reduce the exposure to half of its original value.

The simulated spectrum represents the X-ray photon fluence incident on the detector (the number of photons for each energy E_i, per unit area per unit exposure) $N(E_i)$. The fraction of photons absorbed in the photoconductor is given by the energy-dependent Beer–Lambert law [63]:

$$N_{abs}(E_i) = N(E_i) \cdot \left(1 - \exp\left\{-\left(\frac{\mu(E_i)}{\rho}\right) \cdot \rho \cdot d\right\}\right), \quad \text{(A1)}$$

where $\left({}^{\mu(E_i)}/_{\rho}\right)$ is the mass attenuation coefficient; ρ—density; d—thickness of a-PbO layer. The absorbed energy is then calculated by summing the absorbed fraction $\left(= \frac{\left({}^{\mu_{en}(E_i)}/_{\rho}\right)}{\left({}^{\mu(E_i)}/_{\rho}\right)}\right)$ of the energy fluence $(= N(E_i) \cdot E_i)$ over the entire energy range. For the detector with an area A and an incident exposure X, the total absorbed energy is:

$$E_{abs} = A \cdot X \cdot \sum_i \left(\frac{\left({}^{\mu_{en}(E_i)}/_{\rho}\right)}{\left({}^{\mu(E_i)}/_{\rho}\right)} \cdot N_{abs}(E_i) \cdot E_i\right), \quad \text{(A2)}$$

where $\left({}^{\mu_{en}(E_i)}/_{\rho}\right)$ is the mass-energy absorption coefficient. The mass attenuation and mass-energy absorption coefficients for PbO were derived from the elemental coefficients for Pb and O (obtained from the NIST database [58]) as averages weighted by atomic mass.

The effective area of a detector is determined by the area of a smaller electrode, which in our case was a top gold contact. The exposure X' was measured with an ionization chamber located at a distance d_1 from the tube's anode, away from the detector at a distance d_2. The exposure in the detector's plane was then calculated by the inverse square law. Since the photoconductor was irradiated through the 0.7 mm thick glass substrate, its attenuation was also considered. The

transmittance of the substrate T_s was separately measured for each spectrum as the ratio of exposures with and without a "blank" substrate (i.e., the glass substrate without the photoconductor film deposited) in front of the X-ray tube window with all other parameters fixed. Finally, the incident exposure on the photoconductor is therefore given as:

$$X = X' \cdot \left(\frac{d_1}{d_1+d_2}\right)^2 \cdot T_s \ . \tag{A3}$$

The number of collected photogenerated ehps was obtained from the current transients. The dark current was subtracted from the current transient, and the resulting photocurrent was integrated over the pulse duration. The amount of charge was divided by an elementary charge *e* to obtain the number of carriers collected:

$$N_{ehp} = \int I_{photo}(t)\, dt / e \ . \tag{A4}$$

The simulated X-ray spectra for the X-ray tube with a tungsten target and 2 mm added Al filtration at different tube voltages are shown in Figure A1a. The low-energy end (up to ~15 keV) was attenuated by the inherent filtration (glass housing) and added Al filtration. The peaks at 58–59 keV and 67–69 keV are due to the emissions of the characteristic K_α and K_β X-ray photons of tungsten, respectively. The spectra were normalized to 1 R of incident exposure for better representation. The inset shows the mean energy, HVL, and exposure at a given tube voltage and typical parameters (2 mm added Al filtration, tube current 200 mA, pulse duration 0.1 s, SDD 80 cm) for unnormalized X-ray beams.

Figure A1b shows measured exposure as a function of the added Al filtration thickness to the naked tube for selected tube voltages. The calculated and measured HVL values for the naked tube are listed in the inset: the difference is <2% for all tube voltages. The error of 2% in HVL value translates into 1% uncertainty in the calculated value of absorbed energy E_{abs}, and therefore, of $W_{\pm}$, which is smaller than a symbol size in Figures 3–6.

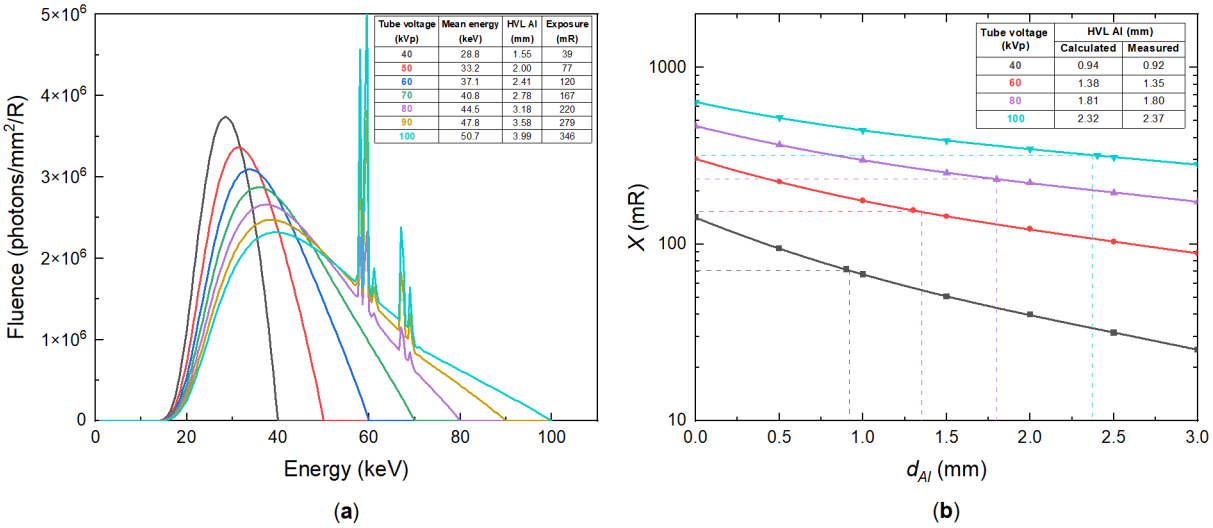

Figure A1. (**a**) The simulated X-ray spectra at different tube voltages, normalized to 1 R of exposure. The inset shows typical (see text) parameters of the beams. (**b**) Exposure measured as a function of added Al filtration thickness for different tube voltages. The dashed lines correspond to 50% of the original exposure and HVL of Al. The inset shows calculated and measured HVL values for a naked tube.

Appendix B. Model for the Charge Generation and Recombination Processes in a-PbO

A qualitative model of the charge generation and recombination processes in a-PbO is based on our experimental results, and previous experimental observations and theoretical simulations in a-Se.

Upon impinging on the photoconductor, the energy of the X-ray photon (minus the binding energy of the electron) is mostly transferred to the kinetic energy of a primary electron, since the photoelectric absorption is the main photon interaction mechanism in PbO for the diagnostic X-ray energy range [64]. The kinetic energy of the primary photoelectron is deposited into the material during the inelastic collisions with the outer-shell atomic electrons, which leads to the ionization of these atoms (creation of the ehps) or emission of a phonon (energy loss). A single ionization event can result in the creation of multiple ehps in the vicinity of the interaction site, composing a spur core (Figure A2a). This event could be interpreted as the excitation of plasma waves, which very quickly decay into multiple ehps [53]. After the ehps are created, they diffuse away from the excitation location in a thermalization process and gradually lose their initial kinetic

energy. At the end of the thermalization process, ehps are separated by a finite thermalization distance (which can be estimated by the Knights–Davis equation [67], but usually is interpreted as a free fitting parameter), constituting an electron cloud—namely, a spur (Figure A2b). As the primary electron makes its way through the photoconductor, it collides with the atoms and creates many localized spurs along its track. If the ionization density along the track is large enough, individual spurs overlap and form a column of X-ray-generated secondary ehps surrounding the electron's track [41,53] (Figure A2c).

If at the end of the thermalization process, the distance between any oppositely charged carriers is smaller than the Coulombic capture radius (such that their mutual attraction is stronger than the thermal diffusion and the drift in the applied electric field), then the carriers will recombine (Figure A2c). Due to a high density of the X-ray-generated carriers inside the column [32,34,41,53], the mean separation of the twin ehp is larger than the separation between any adjacent non-geminate electrons and holes, meaning that non-geminate ehps are more likely to recombine than the geminate pairs, leading to a columnar recombination mechanism. The carriers with separation larger than the Coulombic capture radius are likely to escape the recombination (Figure A2d) and contribute to the X-ray signal, although the probability of escape depends on the combined effects of the diffusion and extraction fields [34,44,67]. A fraction of the electrons and holes that escaped recombination will drift in the applied electric field towards the opposing electrodes where they are collected (Figure A2e). If columns are generated closely in space, the carriers from different columns and spurs can meet during their drift and recombine in the bulk (Figure A2f), contributing to the bulk Langevin recombination.

Photogenerated charge density is an important parameter in the columnar recombination model since it directly affects the recombination rate. It can be described in terms of the energy deposition rate. The rate of energy deposition by a primary electron (i.e., stopping power) decreases with its kinetics energy and so does with photon energy (see Table 1 and [68]). Thus, the density of ehps in the column decreases with increasing photon energy and ehps have a greater probability of escape [34,35,40,41,54]. Therefore, with increasing energy of the incident X-ray photon, the columnar recombination rate within the photoconductor decreases, increasing the fraction of charge collected.

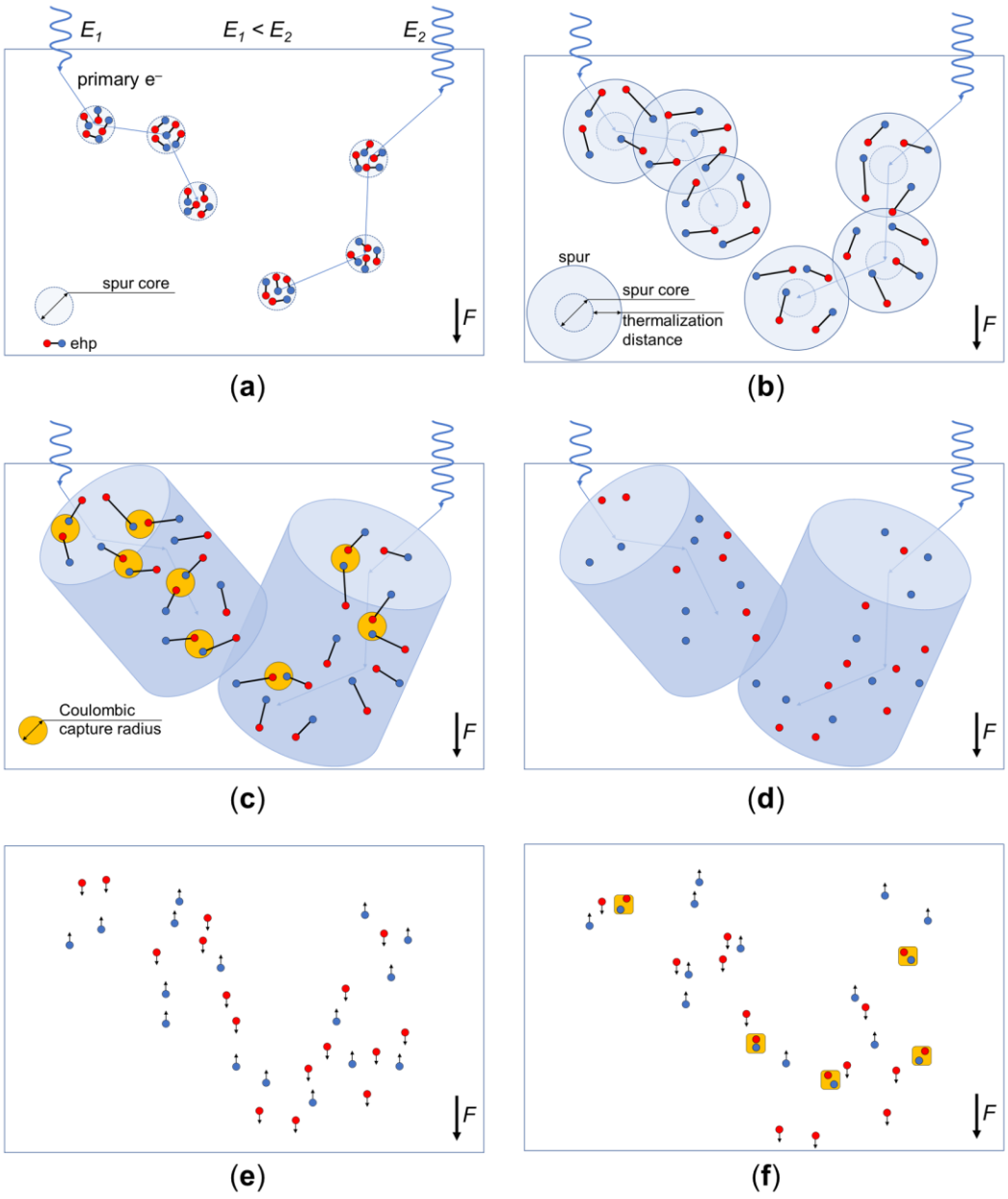

Figure A2. Schematic illustration of the charge generation and recombination processes. (**a**) A primary photoelectron ejected by an incident X-ray photon creates multiple ehps in each ionization event. (**b**) Secondary charge carriers thermalize in a drift-diffusion process and form a spur. (**c**) Overlapping spurs produce an ionization column along the track of the primary photoelectron. Oppositely charged carriers with a separation smaller than the Coulombic capture radius recombine. (**d**) The remaining carriers escape columnar recombination and (**e**) drift through the bulk of the photoconductor. (**f**) Drifting carriers from different columns and spurs recombine in the bulk.

References

1. Kasap, S.O.; Frey, J.B.; Belev, G.; Tousignant, O.; Mani, H.; Greenspan, J.; Laperriere, L.; Bubon, O.; Reznik, A.; DeCrescenzo, G.; et al. Amorphous and Polycrystalline Photoconductors for Direct Conversion Flat Panel X-ray Image Sensors. *Sensors* **2011**, *11*, 5112–5157, https://doi.org/10.3390/s110505112.

2. Kabir, M.Z.; Kasap, S.O. Photoconductors for X-Ray Image Detectors. In *Springer Handbook of Electronic and Photonic Materials*, 2nd ed.; Kasap, S., Capper, P., Eds.; Springer: Cham, Switzerland, 2017; pp. 1125–1147, https://doi.org/10.1007/978-3-319-48933-9_45.

3. Kasap, S.O.; Frey, J.B.; Belev, G.; Tousignant, O.; Mani, H.; Laperriere, L.; Reznik, A.; Rowlands, J.A. Amorphous selenium and its alloys from early xeroradiography to high resolution X-ray image detectors and ultrasensitive imaging tubes. *Phys. Stat. Sol.* **2009**, *246*, 1794–1805, https://doi.org/10.1002/pssb.200982007.

4. Belev, G.; Kasap, S.O. Amorphous selenium as an X-ray photoconductor. *J. Non. Cryst. Solids* **2004**, *345–346*, 484–488, https://doi.org/10.1016/j.jnoncrysol.2004.08.070.

5. Abbaszadeh, S.; Scott, C.C.; Bubon, O.; Reznik, A.; Karim, K.S. Enhanced Detection Efficiency of Direct Conversion X-ray Detector Using Polyimide as Hole-Blocking Layer. *Sci. Rep.* **2013**, *3*, 3360, https://doi.org/10.1038/srep03360.

6. Frey, J.B.; Sadasivam, K.; Belev, G.; Mani, H.; Laperriere, L.; Kasap, S.O. Dark current–voltage characteristics of vacuum deposited multilayer amorphous selenium-alloy detectors and the effect of x-ray irradiation. *J. Vac. Sci. Technol. A* **2019**, *37*, 061501, https://doi.org/10.1116/1.5121197.

7. Polischuk, B.T.; Savard, S.; Loustaneau, V.; Hansroul, M.; Cadieux, S.; Vaque, A. Se-based flat-panel detector for screening mammography. *Med. Imaging 2001 Phys. Med. Imaging* **2001**, *4320*, 582, https://doi.org/10.1117/12.430884.

8. Sun, H.; Zhao, B.; Zhu, X.; Zhu, S.; Yang, D.; Wangyang, P.; Gao, X. Laser-induced surface recrystallization of polycrystalline PbI_2 thick films for X-ray detector application. *Appl. Surf. Sci.* **2018**, *427*, 1146–1151, https://doi.org/10.1016/j.apsusc.2017.08.144.

9. Condeles, J.F.F.; Mulato, M. Polycrystalline lead iodide films produced by solution evaporation and tested in the mammography X-ray energy range. *J. Phys. Chem. Solids* **2016**, *89*, 39–44, https://doi.org/10.1016/j.jpcs.2015.10.012.

10. Street, R.A.; Ready, S.E.; Van Schuylenbergh, K.; Ho, J.; Boyce, J.B.; Nylen, P.; Shah, K.; Melekhov, L.; Hermon, H. Comparison of PbI_2 and HgI_2 for direct detection active matrix X-ray image sensors. *J. Appl. Phys.* **2002**, *91*, 3345–3355, https://doi.org/10.1063/1.1436298.

11. Lee, D.; Lee, K.; Seo, J. High signal-to-noise ratio HgI_2 X-ray detector assisted with ultraviolet radiation. *Nucl. Instrum. Methods Phys. Res. Sect. A Accel. Spectrometers Detect. Assoc. Equip.* **2019**, *941*, 162364, https://doi.org/10.1016/j.nima.2019.162364.

12. Antonuk, L.E.; El-Mohri, Y.; Zhao, Q.; Jiang, H. Exploration of strategies for implementation of screen-printed mercuric iodide converters in direct detection AMFPIs for digital breast tomosynthesis. *Med. Imaging 2017 Phys. Med. Imaging* **2017**, *10132*, 101320A, https://doi.org/10.1117/12.2254552.

13. Lee, S.; Kim, J.S.; Ko, K.R.; Lee, G.H.; Lee, D.J.; Kim, N.W.; Kim, J.E.; Kim, H.K.; Kim, N.W.; Im, S. Direct Thermal Growth of Large Scale Cl-doped CdTe Film for Low Voltage High Resolution X-ray Image Sensor. *Sci. Rep.* **2018**, *8*, 14810, https://doi.org/10.1038/s41598-018-33240-1.

14. Znamenshchykov, Y.V.; Kosyak, V.V.; Kononov, O.K.; Shpetnyi, I.O.; Grebinaha, V.I.; Fochuk, P.M.; Opanasyuk, A.S. Electrical, structural and optical properties of $Cd_{1-x}Zn_xTe$ thick polycrystalline films. *Vacuum* **2018**, *149*, 270–278, https://doi.org/10.1016/j.vacuum.2018.01.010.

15. Liu, Y.; Sun, H.; Yang, D.; Wangyang, P.; Gao, X.; Gou, Z.; Zhu, X. Electrical properties of x-ray detector based on bismuth tri-iodide single crystal with electrode configuration considering. *Mater. Res. Express* **2019**, *6*, 055902, https://doi.org/10.1088/2053-1591/aaff87.

16. Zhou, L.; Huang, Z.; Zhao, X.; He, Y.; Chen, L.; Xu, M.; Zhao, K.; Zhang, S.; Ouyang, X. A High-Resistivity ZnO Film-Based Photoconductive X-Ray Detector. *IEEE Photonics Technol. Lett.* **2019**, *31*, 365–368, https://doi.org/10.1109/LPT.2019.2894296.

17. Simon, M.; Ford, R.A.; Franklin, A.R.; Grabowski, S.P.; Menser, B.; Much, G.; Nascetti, A.; Overdick, M.; Powell, M.J.; Wiechert, D.U. PbO as direct conversion x-ray detector material. *Med. Imaging 2004 Phys. Med. Imaging* **2004**, *5368*, 188, https://doi.org/10.1117/12.533010.

18. Semeniuk, O.; Grynko, O.; Decrescenzo, G.; Juska, G.; Wang, K.; Reznik, A. Characterization of polycrystalline lead oxide for application in direct conversion X-ray detectors. *Sci. Rep.* **2017**, *7*, 8659, https://doi.org/10.1038/s41598-017-09168-3.

19. Rowlands, J.A. Material change for X-ray detectors. *Nature* **2017**, *550*, 47–48, https://doi.org/10.1038/550047a.

20. Semeniuk, O.; Grynko, O.; Juska, G.; Reznik, A. Amorphous lead oxide (a-PbO): Suppression of signal lag via engineering of the layer structure. *Sci. Rep.* **2017**, *7*, 13272, https://doi.org/10.1038/s41598-017-13697-2.

21. Grynko, O.; Thibault, T.; Pineau, E.; Reznik, A. Engineering of a Blocking Layer Structure for Low-Lag Operation of the a-PbO-Based X-Ray Detector. *IEEE Trans. Electron Devices* **2021**, *68*, 2335–2341, https://doi.org/10.1109/TED.2021.3067616.

22. Simon, M.; Ford, R.A.; Franklin, A.R.; Grabowski, S.P.; Menser, B.; Much, G.; Nascetti, A.; Overdick, M.; Powell, M.J.; Wiechert, D.U. Analysis of lead oxide (PbO) layers for direct conversion X-ray detection. *IEEE Trans. Nucl. Sci.* **2005**, *52*, 2035–2040, https://doi.org/10.1109/TNS.2005.856790.

23. Tousignant, O.; Demers, Y.; Laperriere, L.; Mani, H.; Gauthier, P.; Leboeuf, J. Spatial and temporal image characteristics of a real-time large area a-Se x-ray detector. *Proc. SPIE* **2005**, *5745*, 207, https://doi.org/10.1117/12.602183.

24. Tsukamoto, A.; Yamada, S.; Tomisaki, T.; Tanaka, M.; Sakaguchi, T.; Asahina, H.; Suzuki, K.; Ikeda, M. Development and evaluation of a large-area selenium-based flat-panel detector for real-time radiography and fluoroscopy. *Med. Imaging 1999 Phys. Med. Imaging* **1999**, *3659*, 14–23, https://doi.org/10.1117/12.349477.

25. Tsukamoto, A.; Yamada, S.; Tomisaki, T.; Tanaka, M.; Sakaguchi, T.; Asahina, H.; Nishiki, M. Development of a selenium-based flat-panel detector for real-time radiography and fluoroscopy. *Med. Imaging 1998 Phys. Med. Imaging* **1998**, *3336*, 388, https://doi.org/10.1117/12.317039.

26. Adachi, S.; Hori, N.; Sato, K.; Tokuda, S.; Sato, T.; Uehara, K.; Izumi, Y.; Nagata, H.; Yoshimura, Y.; Yamada, S. Experimental evaluation of a-Se and CdTe flat-panel x-ray detectors for digital radiography and fluoroscopy. *Proc. SPIE* **2000**, *3977*, 38–47, https://doi.org/10.1117/12.430924.

27. Hunt, D.C.; Tousignant, O.; Rowlands, J.A. Evaluation of the imaging properties of an amorphous selenium-based flat panel detector for digital fluoroscopy. *Med. Phys.* **2004**, *31*, 1166–1175, https://doi.org/10.1118/1.1707755.

28. Zhao, B.; Zhao, W. Temporal performance of amorphous selenium mammography detectors. *Med. Phys.* **2004**, *32*, 128–136, https://doi.org/10.1118/1.1827791.

29. Semeniuk, O.; Reznik, A.; Sukhovatkin, V. Amorphous lead oxide based energy detection devices and methods of manufacture thereof. *U.S. Patent* 10,163,970 B2; 2018.

30. Klein, C.A. Bandgap Dependence and Related Features of Radiation Ionization Energies in Semiconductors. *J. Appl. Phys.* **1968**, *39*, 2029–2038, https://doi.org/10.1063/1.1656484.

31. Blevis, I.M.; Hunt, D.C.; Rowlands, J.A. Measurement of x-ray photogeneration in amorphous selenium. *J. Appl. Phys.* **1999**, *85*, 7958–7963, https://doi.org/10.1063/1.370615.

32. Que, W.; Rowlands, J.A. X-ray photogeneration in amorphous selenium: Geminate versus columnar recombination. *Phys. Rev. B* **1995**, *51*, 10500–10507, https://doi.org/10.1103/PhysRevB.51.10500.

33. Kasap, S.O. X-Ray Photoconductivity of Stabilized Amorphous Selenium. In *The World Scientific Reference of Amorphous Materials*; Kolobov, A.V., Shimakawa, K., Eds.; World Scientific: Singapore, 2021; pp. 519–538, https://doi.org/10.1142/9789811215575_0016.

34. Kabir, M.Z.; Arnab, S.M.; Hijazi, N. Electron–hole pair creation energy in amorphous selenium: Geminate versus columnar recombination. *J. Mater. Sci. Mater. Electron.* **2019**, *30*, 21059–21063, https://doi.org/10.1007/s10854-019-02475-7.

35. Hijazi, N.; Panneerselvam, D.; Kabir, M.Z. Electron–hole pair creation energy in amorphous selenium for high energy photon excitation. *J. Mater. Sci. Mater. Electron.* **2018**, *29*, 486–490, https://doi.org/10.1007/s10854-017-7937-8.

36. Bubon, O.; Jandieri, K.; Baranovskii, S.D.; Kasap, S.O.; Reznik, A. Columnar recombination for X-ray generated electron-holes in amorphous selenium and its significance in a-Se x-ray detectors. *J. Appl. Phys.* **2016**, *119*, https://doi.org/10.1063/1.4944880.

37. Lachaine, M.; Fallone, B.G. Monte Carlo simulations of X-ray induced recombination in amorphous selenium. *J. Phys. D. Appl. Phys.* **2000**, *33*, 1417–1423, https://doi.org/10.1088/0022-3727/33/11/323.

38. Kasap, S.O.; Rowlands, J.A. X-ray photoconductors and stabilized a-Se for direct conversion digital flat-panel X-ray image-detectors. *J. Mater. Sci. Mater. Electron.* **2000**, *11*, 179–198, https://doi.org/10.1023/A:1008993813689.

39. Kasap, S.O.; Haugen, C.; Nesdoly, M.; Rowlands, J.A. Properties of a-Se for use in flat panel X-ray image detectors. *J. Non. Cryst. Solids* **2000**, *266-269 B*, 1163–1167, https://doi.org/10.1016/s0022-3093(99)00954-0.

40. Haugen, C.; Kasap, S.O.; Rowlands, J.A. Charge transport and electron-hole-pair creation energy in stabilized a-Se x-ray photoconductors. *J. Phys. D. Appl. Phys.* **1999**, *32*, 200–207, https://doi.org/10.1088/0022-3727/32/3/004.

41. Mah, D.; Rowlands, J.A.; Rawlinson, J.A. Sensitivity of amorphous selenium to x rays from 40 kVp to 18 MV: Measurements and implications for portal imaging. *Med. Phys.* **1998**, *25*, 444–456, https://doi.org/10.1118/1.598219.

42. Onsager, L. Initial recombination of ions. *Phys. Rev.* **1938**, *54*, 554–557, https://doi.org/10.1103/PhysRev.54.554.

43. Jaffé, G. Zur Theorie der Ionisation in Kolonnen. *Ann. Phys.* **1913**, *347*, 303–344, https://doi.org/10.1002/andp.19133471205.

44. Hirsch, J.; Jahankhani, H. The carrier yield in a-Se under electron bombardment. *J. Phys. Condens. Matter* **1989**, *1*, 8789–8798, https://doi.org/10.1088/0953-8984/1/45/004.

45. Kasap, S.O.; Fogal, B.; Kabir, M.Z.; Johanson, R.E.; O'Leary, S.K. Recombination of drifting holes with trapped electrons in stabilized a-Se photoconductors: Langevin recombination. *Appl. Phys. Lett.* **2004**, *84*, 1991–1993, https://doi.org/10.1063/1.1667001.

46. Haugen, C.; Kasap, S.O. Langevin recombination of drifting electrons and holes in stabilized a-Se (Cl-doped a-Se: 0.3% As). *Philos. Mag. B* **1995**, *71*, 91–96, https://doi.org/10.1080/01418639508240295.

47. Reznik, A.; Jandieri, K.; Gebhard, F.; Baranovskii, S.D. Non-Onsager mechanism of long-wave photogeneration in amorphous selenium at high electric fields. *Appl. Phys. Lett.* **2012**, *100*, 50–54, https://doi.org/10.1063/1.3697643.

48. Xu, X.; Qian, W.; Xiao, S.; Wang, J.; Zheng, S.; Yang, S. Halide perovskites: A dark horse for direct X-ray imaging. *EcoMat* **2020**, *2*, e12064, https://doi.org/10.1002/eom2.12064.

49. Johns, H.E.; Cunningham, J.R. *The Physics of Radiology*, 4th ed.; Charles C Thomas: Springfield, IL, USA, 1983; ISBN 0-398-04669-7.

50. Stone, M.F.; Zhao, W.; Jacak, B.V.; O'Connor, P.; Yu, B.; Rehak, P. The x-ray sensitivity of amorphous selenium for mammography. *Med. Phys.* **2002**, *29*, 319–324, https://doi.org/10.1118/1.1449874.

51. Kasap, S.O.; Aiyah, V.; Polischuk, B.; Baillie, A. X-ray sensitivity of a-Se for x-ray imaging with electrostatic readout. *J. Appl. Phys.* **1998**, *83*, 2879–2887, https://doi.org/10.1063/1.367074.

52. Fiedler, H.; Laugwitz, F. Quantum efficiency of electroradiographic selenium layers. *J. Fuer Signalaufzeichn.* **1981**, *9*, 229–235.

53. Fourkal, E.; Lachaine, M.; Fallone, B.G. Signal formation in amorphous-Se-based x-ray detectors. *Phys. Rev. B* **2001**, *63*, 195204, https://doi.org/10.1103/PhysRevB.63.195204.

54. Sahyun, M.R.V. Monte Carlo modeling of electrophotographic x-ray detectors. *J. Appl. Phys.* **1982**, *53*, 6253–6261, https://doi.org/10.1063/1.331543.

55. Fang, Y.; Badal, A.; Allec, N.; Karim, K.S.; Badano, A. Monte Carlo simulation of amorphous selenium imaging detectors. *Med. Imaging 2010: Phys. Med. Imaging* **2010**, *7622*, 762214, https://doi.org/10.1117/12.844983.

56. Semeniuk, O.; Csik, A.; Kökényesi, S.; Reznik, A. Ion-assisted deposition of amorphous PbO layers. *J. Mater. Sci.* **2017**, *52*, 7937–7946, https://doi.org/10.1007/s10853-017-0998-5.

57. Demers, H.; Poirier-Demers, N.; Couture, A.R.; Joly, D.; Guilmain, M.; de Jonge, N.; Drouin, D. Three-dimensional electron microscopy simulation with the CASINO Monte Carlo software. *Scanning* **2011**, *33*, 135–146, https://doi.org/10.1002/sca.20262.

58. Hubbell, J.H.; Seltzer, S.M. Tables of X-Ray Mass Attenuation Coefficients and Mass Energy-Absorption Coefficients from 1 keV to 20 MeV for Elements Z = 1 to 92 and 48 Additional Substances of Dosimetric Interest. 2004. Available online: http://physics.nist.gov/xaamdi (accessed on 1 October 2021).

59. Drouin, D.; Couture, A.R.; Joly, D.; Tastet, X.; Aimez, V.; Gauvin, R. CASINO V2.42—A Fast and Easy-to-use Modeling Tool for Scanning Electron Microscopy and Microanalysis Users. *Scanning* **2007**, *29*, 92–101, https://doi.org/10.1002/sca.20000.

60. Joy, D.C. *Monte Carlo Modeling for Electron Microscopy and Microanalysis*; Oxford University Press: New York, NY, USA, 1993; ISBN 978-0-1950-8874-8.

61. Vilar-Palop, J.; Vilar, J.; Hernández-Aguado, I.; González-Álvarez, I.; Lumbreras, B. Updated effective doses in radiology. *J. Radiol. Prot.* **2016**, *36*, 975–990, https://doi.org/10.1088/0952-4746/36/4/975.

62. Rowlands, J.A.; Yorkston, J. Flat Panel Detectors for Digital Radiography. In *Handbook of Medical Imaging, Volume 1. Physics and Psychophysics*; SPIE: Bellingham, WA, USA, 2000; pp. 223–328, ISBN 978-0-8194-7772-9.

63. Boone, J. X-ray Production, Interaction, and Detection in Diagnostic Imaging. In *Handbook of Medical Imaging, Volume 1. Physics and Psychophysics*; SPIE: Bellingham, WA, USA, 2000; pp. 1–78, ISBN 978-0-8194-7772-9.

64. Berger, M.J.; Hubbell, J.H.; Seltzer, S.M.; Chang, J.; Coursey, J.S.; Sukumar, R.; Zucker, D.S.; Olsen, K. XCOM: Photon Cross Sections Database. 2010. Available online: http://physics.nist.gov/xcom (accessed on 1 October 2021).

65. Grynko, O.; Thibault, T.; Pineau, E.; Juska, G.; Reznik, A. Bilayer lead oxide X-ray photoconductor for lag-free operation. *Sci. Rep.* **2020**, *10*, 20117, https://doi.org/10.1038/s41598-020-77050-w.

66. Tucker, D.M.; Barnes, G.T.; Chakraborty, D.P. Semiempirical model for generating tungsten target X-ray spectra. *Med. Phys.* **1991**, *18*, 211–218, https://doi.org/10.1118/1.596709.

67. Knights, J.C.; Davis, E.A. Photogeneration of charge carriers in amorphous selenium. *J. Phys. Chem. Solids* **1974**, *35*, 543–554, https://doi.org/10.1016/S0022-3697(74)80009-0.

68. Berger, M.J.; Coursey, J.S.; Zucker, M.A.; Chang, J. Stopping-Power & Range Tables for Electrons, Protons, and Helium Ions. 2017. Available online: http://physics.nist.gov/Star (accessed on 1 October 2021).

Author Contributions: Conceptualization, O.G.; methodology, O.G.; software, O.G. and T.T.; validation, O.G., T.T., and E.P.; formal analysis, O.G., T.T., and E.P.; investigation, O.G., T.T., and E.P.; writing—original draft preparation, O.G.; writing—review and editing, O.G. and A.R.; visualization, O.G.; supervision, A.R.; project administration, O.G. and A.R.; funding acquisition, A.R. All authors have read and agreed to the published version of the manuscript.

Funding: This research was funded by Teledyne DALSA, the Natural Sciences and Engineering Research Council of Canada (NSERC) and Mitacs. The APC was funded by NSERC.

Institutional Review Board Statement: Not applicable.

Informed Consent Statement: Not applicable.

Data Availability Statement: The data presented in this study are available on request from the corresponding author.

Acknowledgments: The authors are grateful to Andrey Lomako for valuable discussions on the prospects for the application of a-PbO technology in practical detectors and to Giovanni DeCrescenzo for technical support and useful deliberations.

Conflicts of Interest: The authors declare no conflict of interest.

Received: 14 October 2021 | **Revised**: 30 October 2021 | **Accepted**: 1 November 2021 | **Published**: 3 November 2021

Chapter 6

Conclusions and future work

1 Conclusions

a-PbO is an amorphous X-ray photoconductor with a high atomic number and hence high X-ray stopping power. The very fast X-ray response and absence of signal lag make this material a promising replacement for a-Se in direct conversion X-ray detectors for dynamic X-ray applications in the diagnostic energy range. While the elimination of signal lag represents a breakthrough in PbO technology, comprehensive material science research was necessary to improve the technology and enhance a-PbO properties as an X-ray–to–charge transducer to achieve a theoretically high conversion efficiency and low dark current level.

This work was an effort to improve PbO science and technology to solve many of the practical problems in X-ray photoconductor and detector fabrication that limited the X-ray performance of a-PbO–based detector; it also addressed several theoretical aspects that were previously not fully understood or simply not known. One of the largest challenges was an efficient suppression of the dark current to an acceptably low level without compromising the other characteristics of the a-PbO–based detector.

In the first proposed solution, a PbO-based multilayer detector has been developed and investigated. This detector utilizes a PbO homostructure consisting of two allotropic forms of Lead Oxide: a-PbO and poly-PbO. In this configuration, an a-PbO acts as an injection-preventing layer and a poly-PbO layer serves as the X-ray–to–charge transducer. When combined, these layers provide adequate hole mobilities, low dark current at practical electric fields, and low-lag real-time operation under the exposure in the diagnostic energy range. Such bilayer a-PbO/poly-PbO detector has low complexity of implementation since a sequential deposition of amorphous and polycrystalline layers could be performed in a single deposition cycle, without breaking the vacuum, making the direct conversion system simpler and more economical to manufacture.

Investigation of the charge transport properties of faster carriers in PbO, i.e., holes, revealed that hole transport in the bilayer structure is qualitatively similar to that in single poly-PbO layers. It has a dispersive behaviour that is governed by spatial disorder and hole mobility increases rapidly with the increasing electric field. However, both the dispersion parameter and hole mobility values obtained for a bilayer a-PbO/poly-PbO detector are higher than those for poly-PbO. This was achieved by reducing the structural inhomogeneity of the poly-PbO layer: deposition of a poly-PbO layer on the top of alike a-PbO sublayer makes the structure more homogeneous, hole transport less dispersive, and increases hole mobility. The fact that mobility increases with the electric field is very favourable since it allows to significantly improve the carrier schubweg and to avoid depth-dependent charge collection by application of a stronger electric field.

Evaluation of the temporal response of the bilayer detector under the pulsed X-ray radiation demonstrated an absence of signal build-up during the exposure and very little residual current, i.e., a signal lag. The problem of a large lag is considered to be a major obstacle for the application of many photoconductors in the real-time direct conversion X-ray digital detectors, including poly-PbO. The elimination of signal lag in bilayer PbO structure was achieved by dealing with the root cause of the lag problem in poly-PbO, which is the charge trapping at the interface between the electrode and the photoconductor that causes local enhancement of the electric field and charge injection triggered by X-rays. In a bilayer a-PbO/poly-PbO structure, a homojunction at the poly-PbO interface is formed, which prevents accumulation of charge carriers, reduces charge injection, and therefore, diminishes signal lag and lowers a dark current.

Despite these benefits, the dark current of the bilayer structure is still higher than the recommended level of ~10 pA/mm^2. Additionally, other concerns associated with the practical application of a poly-PbO photoconductor, such as poor stability (structural and electrical) at the ambient conditions, high porosity, and low density, were not addressed here.

The second solution implements a different approach, where a semi-insulating polymer layer of Polyimide is employed in the PI/a-PbO blocking structure. The PI layer prevents the injection of one type of carrier from the electrode while allowing the collection of the photogenerated carriers of the opposite sign from the bulk of the a-PbO photoconductor. This detector can be stably operated under much stronger electric fields (up to 40 V/μm) with a sufficiently low dark current (< 10 pA/mm^2), which leads to improved charge collection efficiency and higher SNR.

Additionally, PI acts as a soft buffer layer reducing shear strain at the interface between the photoconductor and the substrate and improving adhesion.

Investigation of the X-ray response of the PI/a-PbO detector under the continuous and pulsed irradiation demonstrated the unhindered flow of photogenerated carriers from the photoconductor through the PI layer to the electrode. This indicates that charge carriers do not accumulate at the interface and do not cause a screening of the electric field and degradation of temporal performance, despite a foreign layer of PI being introduced in the PI/a-PbO heterostructure. The temporal response of the PI/a-PbO blocking layer structure improves with the application of a stronger electric field, and at the readout rate of 30 frames per second shows a signal lag value < 1%, which satisfies requirements for the real-time diagnostic imaging and 3D tomosynthesis applications. The X-ray sensitivity remains stable with no ghosting effect observed at relatively low exposure rates (< 1 R/s), indicating an absence of deep charge trapping in the a-PbO photoconductor.

Although the introduction of the PI layer increases the technological complexity of the PI/a-PbO detector preparation process in comparison to that of bilayer a-PbO/poly-PbO detector, since it requires an additional technological step, this is not a significant complication. Indeed, the polyimide can be applied to large-area substrates by a conventional spin-coating technique, it is compatible with CMOS surface topography and PbO deposition technology. Moreover, its charge blocking properties can be tuned by varying the thickness of the layer during the coating.

Development of the blocking layer structure allowed to significantly suppress the dark current and to overcome the practical challenges of the X-ray response measurement under a low radiation exposure and a high applied bias. This permitted to carry out a thorough and accurate characterization of the X-ray sensitivity of a-PbO photoconductor in terms of the electron-hole pair creation energy $W_{\pm}$ and to investigate the fundamental mechanisms governing it.

$W_{\pm}$ was measured over a wide range of the electric fields, X-ray photon energies (in diagnostic energy range) and radiation exposures. $W_{\pm}$ decreases (X-ray sensitivity improves) with the increasing electric field and X-ray energy and saturates after 10 V/μm. The saturated $W_{\pm}$ values are 18–31 eV/ehp for the irradiation with a mean energy of 51–29 keV, respectively. Also, $W_{\pm}$ increases with increasing radiation exposure rate, especially at lower electric fields. These results

demonstrate that the PI/a-PbO detector performs best at strong practical electric fields (10–20 V/μm) in diagnostic energy range and under low exposures.

The a-PbO–based detector offers twice higher X-ray sensitivity in comparison to the detector based on an a-Se photoconductor under similar practical electric fields and X-ray energies. However, effective $W_{\pm}$ is still higher than the theoretical value, implying that a fraction of X-ray–generated carriers undergo recombination before they are collected. The analysis of $W_{\pm}$ dependency on the field, energy and exposure indicates an interplay between Langevin recombination within the ionization column (i.e., columnar recombination) and bulk Langevin recombination mechanisms, which together are responsible for the carrier loss and relatively high $W_{\pm}$ in a-PbO at electric fields lower than 10 V/μm. At stronger fields, the columnar Langevin recombination cannot be accounted for the observed field dependency of $W_{\pm}$ as the recombination process is no longer determined by the probability of X-ray–generated carriers to meet in space.

2 Significance of the results

The development of the PbO-based detector technology is an important scientific and engineering accomplishment in the continuing development of digital X-ray imaging systems. Teledyne DALSA, a Canadian and a global leader in digital imaging products and solutions for medical and industrial imaging markets, recognizes the high potential of the application of a-PbO as an X-ray–to–charge transducer in the next generation of DALSA's direct conversion flat panel X-ray imaging detectors. The research agreement between Lakehead University and Teledyne DALSA was signed and outlines joint research opportunities, as well as knowledge and technology transfer for commercialization of the a-PbO–based detectors.

Teledyne DALSA will benefit from new scientific and engineering knowledge when optimized PbO manufacturing techniques are transferred to them. This will enable the manufacturing of PbO-based direct conversion detectors with greater sensitivity at lower X-ray exposures. High-sensitivity PbO-based detectors have the core benefit of reducing the incident X-ray dose to acquire a diagnostic image, and thereby improve the overall safety of general radiography and interventional procedures, such as those required during cardiac interventions. These are often dose-limited procedures that have the follow-on consequence of limiting cardiac therapy and

subsequently the well-being of patients suffering from a heart-related illness. The development of advanced technology for PbO as a photoconductive material will facilitate the widespread clinical application of fluoroscopy-based cardiac interventions.

3 Future work

The scaling of the a-PbO technology at its current state is limited by the capabilities of the ion-assisted thermal evaporation vacuum system used for the deposition of a-PbO layers. The growth of thick layers is extremely challenging due to the substrate overheating during the long evaporation cycle, and large-area substrate cannot be used due to the limited dimensions of the vacuum chamber. To overcome these challenges, a new vacuum system must be built that would resolve these problems, even though it requires substantial financial investments. This process is currently underway.

Once this technical step is completed, a limited-size detector prototype should be developed and evaluated to demonstrate the practical feasibility of an a-PbO photoconductor for diagnostic imaging detectors. To achieve this, a PI blocking layer and a 100-μm thick a-PbO photoconductive layer should be evaporated on a small-size (approx. 5 cm × 5 cm) TFT or CMOS imaging array. For quantitative evaluation of imaging performance, detector performance parameters such as modulation transfer function (MTF), noise power spectrum (NPS) and detective quantum efficiency (DQE) as a function of spatial frequency and different radiation doses should be investigated [1]. These three parameters are fundamental metrics of system performance, rather than its individual components (i.e., photoconductor, imaging electronics, etc.) and describe the performance of the entire detector system. MTF characterizes the spatial resolution of the detector, NPS describes the magnitude and spatial frequency of image noise, and DQE accounts for multiple factors (such as attenuation of X-rays, charge generation and collection, etc.) and provides a comprehensive description of how efficiently a detector produces a radiographic image from an incident X-ray beam modulated by the imaged object.

In parallel with fabricating the PbO detector prototype and characterizing its imaging performance, the development of a PbO-based blocking structure should be continued. Cerium oxide (CeO_2) [2] is one of the promising materials with a compatible deposition method. Additionally, recent

progress in the ion-assisted deposition of germanium oxide (GeO_2) [3] thin films opens an opportunity to develop a deposition process where both a photoconductive structure and a blocking layer are deposited in one cycle. GeO_2 or CeO_2 film, several tens of nm in thickness, may efficiently prevent the injection of positive charge from the anode by forming a high potential barrier to holes, while photogenerated electrons can drift freely through the same interface.

After the proof-of-concept of the a-PbO–based detector is demonstrated, a full-size detector with an 800-μm thick a-PbO–based blocking structure on an approximately 30 cm × 30 cm imager should be fabricated. MTF, NPS and DQE should be measured as described above. For qualitative image evaluation, images of the various anatomical phantoms should be acquired at clinically relevant conditions.

This work is expected to be performed in collaboration with our industrial partner, Teledyne DALSA. This ensures that the developed PbO-based detector technology will be compatible with DALSA's X-ray systems currently in use, thereby maximizing the economic value and market potential of research on PbO science and technology.

4 References

[1] Kasap, S.O.; Frey, J.B.; Belev, G.; Tousignant, O.; Mani, H.; Greenspan, J.; Laperriere, L.; Bubon, O.; Reznik, A.; DeCrescenzo, G.; Karim, S.K.; Rowlands, J.A. Amorphous and Polycrystalline Photoconductors for Direct Conversion Flat Panel X-Ray Image Sensors. *Sensors* 11, 5112–5157 (2011), doi: 10.3390/s110505112.

[2] Wang, K.; Abbaszadeh, S.; Karim, K.S.; Rowlands, J.A.; Reznik, A. Reactive Ion-Assisted Deposition of Cerium Oxide Hole-Blocking Contact for Leakage-Current Suppression in an Amorphous Selenium Multilayer Structure. *IEEE Sens. J. 15*, 3871–3876 (2015), doi: 10.1109/JSEN.2015.2397953.

[3] Miller, J.W.; Chesaux, M.; Deligiannis, D.; Mascher, P.; Bradley, J.D.B. Low-loss GeO_2 thin films deposited by ion-assisted alternating current reactive sputtering for waveguide applications. *Thin Solid Films 709*, 138165 (2020), doi: 10.1016/j.tsf.2020.138165.